Quantum Dot Ensembles as an Optical Quantum Memory

With an Investigation in High Order Wavemixing in Two-Level Quantum Systems

Michael Woodhouse

Department of Physics and Astronomy

University of Sheffield

This dissertation is submitted for the degree of

Doctor of Philosophy

September 2015

Acknowledgements

I would like to to thank David Whittaker for supervising me during my PhD, checking the sanity of many of my results and to Tim Spiller and David for painstakingly reading through copies of this thesis, providing invaluable comments. Thank you to Phil and my Marjorie Woodhouse (my Grandma) for checking though this thesis for errors and to everyone else, especially those at Cornerstone, for support and understanding while I've been writing up.

Abstract

In this Ph.D. Thesis we investigate the viability of using quantum dot ensembles as a quantum memory architecture through the use numerical simulations to study population transfer within quantum dots. This is followed by an investigation into the effects of high order wavemixing on the population transfer within two level systems, which was born from effects noted while simulating quantum dots.

We study the initialisation of an ensemble of inhomogeneously broadened quantum dots, introducing a novel initialisation method utilising pump field with a slow frequency sweep. We focus on the properties of such an initialisation procedure and conclude that the maximum initialisation fidelities are determined entirely by the Zeeman splittings and decay rates of the quantum dots.

We study several possibilities for performing π rotations on the population of an ensemble of quantum dots, and show the RCAP protocol is the most applicable. We study this protocol in the context of quantum dots and give the optimal parameters to use to generate high fidelity π pulses.

We then bring together our work on quantum dots population transfer with the work of others covering the write and read procedures on quantum dots to provide a feasibility analysis of the complete quantum memory protocol.

The work on wavemixing presented in this thesis uses a novel approach to analyse wavemixing effects which is used to predict the population transferred in two level simulations of wavemixing processes. We provide simulation confirmation of our approach to analyse wavemixing effects and then go on to calculate the disruptive effects of wavemixing caused by high intensity lasers on some simple systems. Finally we show that large orders of wavemixing can, at least in principle, be used for coherent population transfer.

Table of contents

Table 1 Abbreviations

Abbreviation	
QD	Quantum Dot
QM	Quantum Memory
EIT	Electromagnetically Induced Transparency
ARP	Adiabatic Rapid Passage
STIRAP	STImulated Raman Adiabatic Passage
RCAP	Raman Chirped Adiabatic Passage
SCRAP	Stark Chirped Rapid Adiabatic Passage
NWM	(Number: 4, 6, 8 ...etc) Wave Mixing

Chapter 1

Introduction: Quantum Dots/Quantum Information

1.1 Quantum Information Processing

Quantum information processing has been shown to be capable of greatly increasing the efficiency of certain computational problems such as factoring large integers [70], searching databases [37] and simulating quantum systems [22]. Quantum communication enables the creation of distributed quantum networks allowing, among other things, faithful transmission of quantum states over long distances via teleportation and the ability to have completely secure communication between remote locations using Quantum key distribution.

At the core of a Quantum Computer is the qubit, a quantum state that can be represented by any quantum system with two (or more) well defined eigenstates, pictorially represented by the three dimensional Bloch sphere, Fig 1.1. Physically there are many different qubits that have been used; For example, the spin of a single electron in silicon with a phosphorus donor [59], the hyperfine levels and phonon modes in trapped ions[73], the charge state of superconducting devices [12], and many more. Throughout this thesis we will be concentrating on two physical qubits implementations: the photonic qubit, where the information is encoded in the state of a single photon, which could be its polarisation, channel, arrival time or photon number and the encoding of a qubit in an ensemble of electron spins, which we shall discuss in detail later. To perform quantum information processing successfully, qubits must satisfy the famous DiVincenzo criteria [25][24] and need to be capable of being initialised, rotated, interacted with other qubits, stored, transported and measured. The combination of

photons and electron spin ensembles provides the possibilities for easy transportation and quantum gates with photons and stable storage in the spin ensembles.
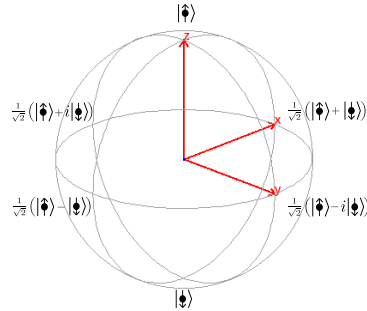

Fig. 1.1 The qubit, represented by the Bloch sphere above has not only the classical states "on", $|\spadesuit\rangle$ or $|Z\rangle$, and "off", $|\clubsuit\rangle$ or $|-Z\rangle$, but also superpositions of these two with a phase ϕ given by $\frac{1}{\sqrt{2}}\left(|\spadesuit\rangle + e^{i\phi}|\clubsuit\rangle\right)$, which gives the states represented by $|X\rangle$ and $|Y\rangle$ for ϕ equal to 0 and $\frac{\pi}{2}$ respectively. In general a quantum state is given by $\alpha|\spadesuit\rangle + \beta|\clubsuit\rangle$, where $|\alpha|^2 + |\beta|^2 = 1$ corresponds to pure states which are on the surface of the Bloch sphere and $|\alpha|^2 + |\beta|^2 < 1$ corresponds to mixed states which are inside the Bloch sphere.

Manipulations of the qubits within a quantum computer are all performed by unitary gates that are either single qubit rotations around the surface of the qubits Bloch sphere, for example the Hadamard gate; or multi qubit gates in which the rotation of one qubit is conditional on the state of another qubit, for example the controlled not (CNOT) gate. When performing a gate such as the CNOT gate it is important that the state of the second qubit is rotated without classically measuring the control qubit and therefore collapsing its state and destroying the quantum correlations in the system. Single qubit rotations and the CNOT gate together are an example of a universal set of quantum gates [2] and can therefore be used to construct any other quantum gate.

1.1.1 Quantum Memories

A quantum memory is a physical system that can store the state of a qubit and return it for use later; it must be capable of preserving the full information within the qubit, including any entanglement with other qubits. An operational quantum memory cannot use the classical approach of measure and write down as this destroys the quantum nature of the information encoded within the qubit and any entanglement with other qubits.

Quantum memories are an integral part of realising many current ideas within quantum communication and quantum information processing and are particularly important for scaling up from single gates to fully functional quantum computers and within linear optical quantum computers. [48]

Direct entanglement of two photons requires them to interact. One option for interacting light could be through a material with highly non-linear properties, such that the existence of one photon changes how the second photon travels through the medium creating a controlled gate. The response of materials to single photons is however too weak to implement this approach. A different approach uses the photon statistics at beam splitters to entangle two photons, known as linear optical quantum computing. The linear optical entangling gates can generate entanglement between two photons, however the gates have only a probabilistic chance for success and require further measurements [42] on one or more ancilla modes to determine whether the gate was successful. Since the success of the gate is conditional on the measurements of the ancillae the scheme becomes exponentially slower to run for higher gate numbers when all gates need to be successful simultaneously, this is of course not scalable. Currently all proposed implementations of linear optical quantum computers require some form of quantum memory [43]. Quantum memories allow various stages of the computation to be stored temporarily until further gates have been performed successfully, making the use of the large network of gates required for quantum computing a possibility.

Photons are the obvious choice of carrier for quantum communication due to their speed and weakly interacting nature, the qubit information can be encoded in many ways including the polarisation, path and timing of the photon. However, before quantum repeaters were considered, long distance quantum communication for Quantum Key Distribution and for quantum networks was not considered to be feasible with the current optical technologies. This was because of the exponential absorption of photons in the fibre optic channels used making it exponentially expensive to faithfully communicate a quantum state. Quantum repeaters make communication over long distances feasible with lossy channels by exchanging and purifying entanglement with neighbouring quantum repeaters, which can be placed sufficiently close such as to have a reasonable probability of transferring the state [6]. The quantum repeaters in turn swap the entanglement with their neighbours until pairs of maximally entangled states are generated at the desired locations, which can be arbitrarily far apart. This protocol changes the communication fidelity from one which is exponentially decreasing with length to one which is only polynomially decreasing with length. One of the central components of all quantum repeater protocols is a quantum memory, for example the

DLCZ protocol [26], which uses entangled atomic ensembles. Generally the three level Raman memory is discussed for this application, but it should be possible to use any type of optical quantum memory with photon retrieval to the same end.

All processes within the quantum computer will operate at a fidelity which is below unity and therefore each process introduces errors into the calculation. These errors would quickly build up and degrade the calculation. However due to quantum error correction these errors can be removed.

There are three possible errors that can occur in a photonic quantum memory. The first is photon loss when the photon is not returned. The second error is when noise that creates an extra photon alongside the signal photon. If the computational scheme can detect multi-photon errors and discard them then these can be considered to be a simple loss, else the error would lead to a computational error. The third possibility is when the original photon is lost while a noise photon is also generated. Without quantum error correction these will result in computational errors.

Some fault tolerant quantum computing schemes have been shown to be tolerant to up to 50% loss rate[78], however these do not generally include corrections for computational errors. A more recent paper [3] describes a scheme which can still tolerate a high rate of loss, up to 25% while simultaneously including a tolerance to computational errors of 0.6%. A quantum memory would have to function within these bounds to be useful within a quantum computer.

1.1.2 Quantum Memory Process

The quantum memory process for can be separated into four distinct processes:

1. Initialisation:

   Preparing the memory state to be ready to store a qubit.

2. Write in:

   Transferring the qubit state from the external photonic qubit to a qubit encoded within the ensemble memory.

3. Storage:

   Performing any necessary actions to keep the qubit from being lost/decohering during storage.

4. Read out:

Transferring the state of the qubit from the memory back out to an external photonic qubit.

1.1.3 Quantum Memory Implementations

While an optical qubit could be encoded in many ways, an optical quantum memory can be reduced to being a pair of single photon storage devices. For the memories we will consider here, only path amplitude and not polarisation can be stored in a single device, so for a polarisation encoded qubit the qubit is first transformed into a path encoded qubit as shown in figure 1.2. The black box single photon storage devices can be anything that stores a single photon and deterministically releases it at a later time, preferably on demand.
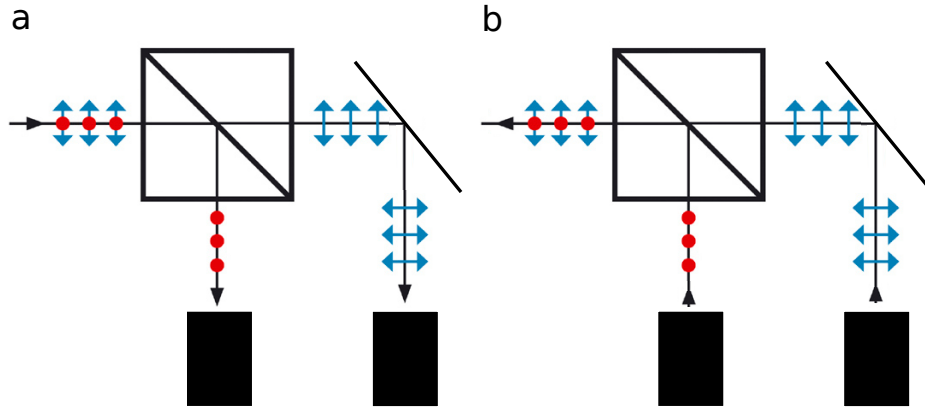
Fig. 1.2 a.) An incoming polarisation encoded qubit is transformed into a channel encoded qubit through a polarising beam splitter. A channel encoded qubit can then be stored within the two single photon storage devices. The qubit is then jointly stored between the two single photon storage devices, each single photon storage device stores one of the original polarisation amplitudes independently b.) Reconstruction of the original qubit is achieved by releasing the photon stored between the two devices simultaneously back through the same optical circuit.

In this thesis we will be considering quantum memories based on ensembles of Quantum Dots (QDs). Two potential options are Raman transfer and Electromagnetically Induced Transparency (EIT). In three level Λ systems (see figure 2.2). For EIT Δ (shown in figure 2.2) is set to 0, whilst for Raman transfer $\Delta \gg \Omega_1, \Omega_2, \delta$. Both systems have been widely studied in recent years [15, 30, 31] and both offer promise for viable quantum memories. On one level EIT and Raman memories are similar techniques as they both use ensembles of three level lambda systems, using the collective coupling enhancement of $\sqrt{N}$ between the light and the atoms where N is the number

of interacting atoms/dots [47]. Both use a signal and control pulse that propagate together to generate a collective atomic coherence, which we from now on shall refer to as a "spin wave", in the ground states; as such these memory implementations are sometimes analysed using similar methods [32]. However, compared to EIT, the read and write operations of Raman transfer discussed later use different physical methods. EIT generates a high dispersion from the interference between two absorption pathways, absorption directly into the excited state and absorption into the ground state mediated via the control pulse. This has the effect of allowing the signal pulse to propagate through the medium at a reduced speed where it would normally have been instantly absorbed. To store the signal the power of the control pulse is adiabatically reduced, slowing the pulse further until the signal is absorbed as a spin wave in the ground states of the ensemble. Raman memories however detune the control and signal sufficiently from resonance such that absorption into the excited state can be safely ignored, leaving only the coherent absorption of the signal into the second ground state via the control pulse. Both methods store the state in a collective spin wave excitation across the ensemble. The two approaches are each suitable for different applications. EIT is more suitable for use when photon absorption time is longer than the atomic lifetime (Γ^{-1}) whereas the broadband pseudo state that is created in a fast Raman transition is capable of storing much shorter, broadband photons [53].

The Raman memory protocol requires an ensemble with two stable ground states and a third exited state, which is optically coupled to both ground states via different polarisations, thus enabling them to be coupled separately. Since the Raman protocol uses an off resonance transition it is fairly robust to inhomogeneities in the ensemble, unlike EIT which requires each atom to be on resonance with both the control pulse and the input photon as large inhomogeneities can destroy the transparency [54]. This condition is particularly important later when we consider the inhomogeneities between QDs, and leads us to only consider the Raman protocol where relevant.

Currently one of the more popular Raman memory experiments uses the Λ system defined by the hyperfine levels of caesium gas as ground states to store the spin wave and an excited P orbital for the transition [63]. The transition couplings are selected via field polarisation and can therefore be addressed individually. The output fields go through both polarisation and spectral filters allowing the weak signal field to be distinguished from the much stronger control pulse. Current experiments are not yet optically thick and therefore the transmitted signal is larger than the absorbed signal. This experiment intrinsically contains Doppler shifted inhomogeneous broadening.

A third QM implementation that is often discussed is the photon echo approach. The technique can be performed on an ensemble of either two or three level systems. Several different pulse schemes are commonly used but they all work by allowing the dipoles to dephase during storage and be rephased later at a chosen retrieval time which induces the emission of an output pulse by the ensemble. The problem with this approach is that there is a fundamental signal to noise ratio that is below unity [65] and applies to the commonly used schemes. As such this approach will not been considered further here.

1.2   Quantum Dots

A Quantum Dot (QD) is something that can confine an electron or a hole in all three dimensions. Instead of having a continuum of possible energy states like particles in a bulk, sheet or wire, particles in a QD can only exist at specific discrete energy levels; transitions between these levels produces discrete spectral lines. As a result of this discreteness QDs are frequently referred to as artificial atoms. Quantum dots require extremely small dimensions, usually on the order of nm, to confine the particles in well defined quantum states.

Semiconductor QDs are of particular interest as potential quantum memories because of their integrability into nano structure solid state photonic circuits. Other potential quantum memories, such as NV centres in diamond and gas based memories [15], require additional architecture to interface them with semiconductor devices. QDs have the advantage of being fabricated using similar techniques and materials and are of appropriate dimensions such that they should be integrable into semiconductor hardware currently being developed [7].

In fabrication, as the length scales of components decrease, traditional nano-fabrication techniques such as lithography become increasingly costly and impractical. This has led to the use of techniques such as self-assembly which allow large numbers of QDs to be produced relatively simply and cheaply. Stranski–Krastanov epitaxial growth uses lattice-mismatched growth to nucleate small droplets of, for example, InGaAs within a GaAs substrate [62] and can create structures of 10's of nanometres across. The position of self assembled QDs is in general not controlled, although the dots can be placed on selected sites through prior lithographic patterning of the surface if necessary [66]. However the size, shape and composition of the QDs produced using self assembly is currently only partially controlled and therefore varies slightly between any two dots, hence any properties that depend on the size and shape and composition

of the QDs will also vary. The differences between the individual QD in a particular ensemble produces an energy variation between their energy levels [64], resulting in inhomogeneous broadening of the emission spectra. From now on we will refer to these Stranski–Krastanov self assembled QDs as simply "Quantum Dots" (QDs) unless explicitly stated otherwise.

The QDs may either be neutral or charged depending on the presence of any dopants in the substrate or any fields applied to the system. Here we are interested in the case of ensembles of charged QDs as these provide a large number of systems with a pair of stable ground states given by a single electron spin ($|\Downarrow\rangle$, $|\Uparrow\rangle$). The lifetime of the ground state electrons is very long and has been demonstrated to be of the order of milliseconds [44], orders of magnitude larger than any gates performed on the active photons in the computer. For individual dots population transfer times can be as small as 38ps [60]. While manipulation of an ensemble with inhomogeneous broadening would generally require longer gate times, these are still well within the dot coherence time, as we shall show later. These ground states are optically coupled to two unstable trion states with a lifetime of around 1ns [11], made up of two electrons and a heavy hole. The hole spin determines the trion state ($|\Downarrow\Uparrow\Downarrow\rangle$, $|\Downarrow\Uparrow\Uparrow\rangle$). There are various selection rules possible depending on the geometry of the fields, described in section 1.2.1. These couplings allow for manipulation of quantum information held in the state of the ground state electron, while using the electrons inherent stability for storage.

With the QDs and transitions being considered here, the inhomogeneous broadening presents itself primarily in differences between the energy gap E_x required to generate an exciton which is the energy gap between the lower levels and the upper levels in figure 1.4. This inhomogeneous broadening means that we can only consider manipulations that are insensitive to the exact value of E_x, this is contrary to much of the QD research based upon single QDs which relies upon resonant fields, for example [60].

1.2.1   The Model

The research presented in this thesis is independent of the underlying heterostructure and the types of state used in the implementation, as any ensemble of systems with a set of basis states that are governed by the Voigt geometry Hamiltonian in equation (1.4) will be consistent with the transfer mechansms that we present later. In this section however we will consider the specific case of the interaction of the electron and heavy hole negative trion spin states in QDs and their optical transitions. This will be the example we refer back to throughout the thesis.

We assume negligible light hole-heavy hole mixing, the tight confinement in a QD leads to an energy splitting of 10's of meV between the light and heavy holes [19] allowing us to safely ignore the effects of the light hole states. We use the following basis states $|\psi\rangle = \{|\spadesuit\rangle,\ |\spadesuit\rangle, |\spadesuit\spadesuit\spadesuit\rangle,\ |\spadesuit\spadesuit\spadesuit\rangle\}$, where $\spadesuit$ represents an "up" spin hole and $\spadesuit$ represents a down spin electron. We are interested in the coupling between the ground state electron and the excited heavy-hole trion state of charged QDs under the effect of an external magnetic field and arbitrary laser coupling. We assume that the electron-trion transition can be modelled as a dipole, the wavelength of light used is approximately 1μm while the average dot size is under 100nm so this should be a reasonable approximation. This results in dynamics that are governed by the Hamiltonian (1.1) below, as given by ([19, 77]).

$$H = \begin{pmatrix} \omega_B g_z^e \cos(\theta) & \omega_B g_x^e \sin(\theta) & e^{-it\omega_-}\Omega^{-*} & 0 \\ \omega_B g_x^e \sin(\theta) & -\omega_B g_z^e \cos(\theta) & 0 & e^{-it\omega_+}\Omega^{+*} \\ e^{it\omega_-}\Omega^- & 0 & E_T + \omega_B g_z^h \cos(\theta) & \omega_B g_x^h \sin(\theta) \\ 0 & e^{it\omega_+}\Omega^+ & \omega_B g_x^h \sin(\theta) & E_T - \omega_B g_z^h \cos(\theta) \end{pmatrix} \quad (1.1)$$

Where Ω^+ and Ω^- are left and right circularly polarised light. E_T is the excitation energy of the trion state, $\omega_B = \frac{1}{2}\mu_B|B|$, θ is the angle of the magnetic field to the growth direction shown in figure 1.3 and g's are the electron/hole g factors. ω_+ and ω_- are the frequencies of the left/right circularly polarised light respectively. For $\theta = 0$ there are two optical transitions between the trion and electron states and two dark transitions. Diagonalisation of the bare states for $\theta \neq 0$ results in four optical transitions between the trion and electron states due to the non zero off-diagonal components. There are two magnetic field configurations which are commonly used, the Faraday geometry where $\theta = 0$ and the Voigt geometry $\theta = \pi/2$, where H_F and H_V are the Hamiltonians in the Faraday Geometry and Voigt geometry respectively.

The Hamiltonian H_F below is for the Faraday geometry with $\theta = 0$ where we can see that each lower state is coupled to a single upper state and there are no terms coupling the pairs together.

$$H_F = \begin{pmatrix} \omega_B g_z^e & 0 & e^{-it\omega_-}\Omega^{-*} & 0 \\ 0 & -\omega_B g_z^e & 0 & e^{-it\omega_+}\Omega^{+*} \\ e^{it\omega_-}\Omega^- & 0 & E_T + \omega_B g_z^h & 0 \\ 0 & e^{it\omega_+}\Omega^+ & 0 & E_T - \omega_B g_z^h \end{pmatrix} \quad (1.2)$$
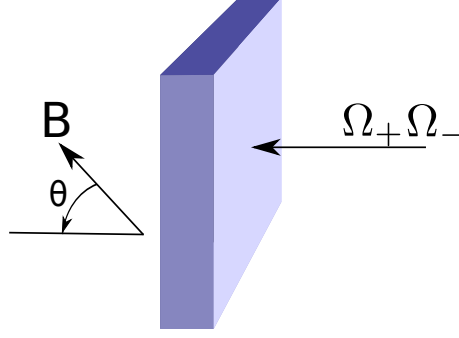
Fig. 1.3 The magnetic field and sample orientation for the Hamiltonian in equation (1.1), where QDs are grown on the lighter coloured plane. Circularly polarised radiation is directed into the growth plane.

This Hamiltonian can be compared to the Voigt geometry Hamiltonian with $\theta = \pi/2$ below.

$$H_V = \begin{pmatrix} 0 & \omega_B g_x^e & e^{-it\omega_-}\Omega^{-*} & 0 \\ \omega_B g_x^e & 0 & 0 & e^{-it\omega_+}\Omega^{+*} \\ e^{it\omega_-}\Omega^- & 0 & E_T & \omega_B g_x^h \\ 0 & e^{it\omega_+}\Omega^+ & \omega_B g_x^h & E_T \end{pmatrix} \qquad (1.3)$$

To see the dynamics in the basis of the bare states we first transform into a set of basis states that diagonalises H_V for Ω's$= 0$ which results in the interaction picture that will be used throughout this thesis, given by the states: $|\psi'\rangle = \{\frac{1}{\sqrt{2}}(|\Uparrow\downarrow\rangle + |\Downarrow\uparrow\rangle),$ $\frac{1}{\sqrt{2}}(|\Uparrow\downarrow\rangle - |\Downarrow\uparrow\rangle), \frac{1}{\sqrt{2}}(|\Uparrow\Downarrow\uparrow\rangle + |\Uparrow\Downarrow\downarrow\rangle), \frac{1}{\sqrt{2}}(|\Uparrow\Downarrow\uparrow\rangle - |\Uparrow\Downarrow\downarrow\rangle)\}$. This results in the Hamiltonian H'_V:

$$H'_V = \begin{pmatrix} \omega_B g_x^e & 0 & \Omega_h^* e^{-i\omega t} & \Omega_v^* e^{-i\omega t} \\ 0 & -\omega_B g_x^e & \Omega_v^* e^{-i\omega t} & \Omega_h^* e^{-i\omega t} \\ \Omega_h e^{i\omega t} & \Omega_v e^{i\omega t} & E_T + \omega_B g_x^h & 0 \\ \Omega_v e^{i\omega t} & \Omega_h e^{i\omega t} & 0 & E_T - \omega_B g_x^h \end{pmatrix} \qquad (1.4)$$

Where Ω_h and Ω_v correspond to horizontally and vertically polarised light respectively. $\Omega_h e^{i\omega t} = \frac{1}{2}\left(\Omega_+ e^{i\omega t} + \Omega_- e^{i\omega t}\right)$ and $\Omega_v e^{i\omega t} = \frac{1}{2}\left(\Omega_+ e^{i\omega t} - \Omega_- e^{i\omega t}\right)$ for $\omega_+ = \omega_- = \omega$. In general there will be external control of the frequencies of the incoming polarised radiation so the frequencies can be varied independently, such that $\Omega_v e^{i\omega t} \rightarrow \Omega_v e^{i\omega_v t}$ and $\Omega_h e^{i\omega t} \rightarrow \Omega_h e^{i\omega_h t}$.

In this thesis we consider quantum dots measured in the Voigt geometry, where the magnetic field is perpendicular to propagation direction of light. This arrangement includes indirect couplings between the two ground states via the excited states,
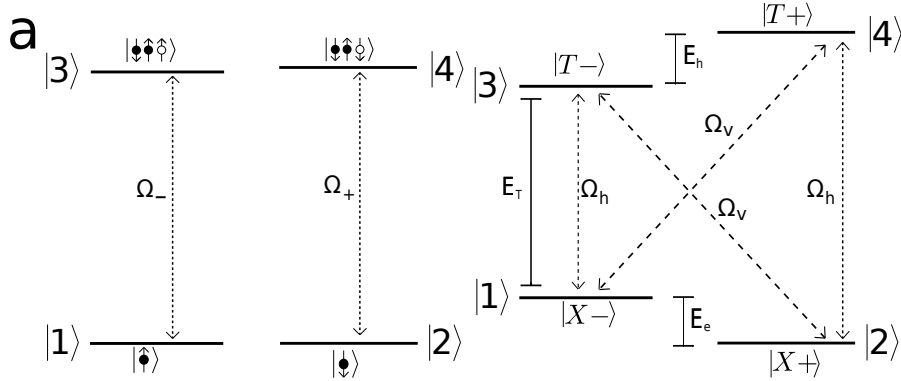
Fig. 1.4 The Faraday and Voigt geometries. For both cases there are two ground states of spin up and spin down electrons: $|\spadesuit\rangle$ and $|\clubsuit\rangle$ ($|1\rangle$ and $|2\rangle$) and two excited trion states: $|\spadesuit\clubsuit\rangle$ and $|\spadesuit\clubsuit\rangle$ ($|3\rangle$ and $|4\rangle$). a.) The Faraday geometry has two couplings from $|1\rangle \rightarrow |3\rangle$ and $|2\rangle \rightarrow |4\rangle$ by circular polarised radiation Ω_- and Ω_+ respectively, cross couplings are forbidden. b.) The Voigt geometry states are optically coupled together with horizontally and vertically polarised radiation Ω_h and Ω_v respectively, as shown by the dotted lines. The energy gaps between the levels are E_h and E_e determined by the g factors and the external magnetic field and E_T given by the trion excitation energy.

resulting in the possibility of coherent population transfer between the states whist not resulting in strong decoherence that would generally be associated with a direct coupling. The dynamics for the Voigt geometry are given by the Hamiltonian in equation (1.4) which is widely used in the literature [29, 60, 82]. The selection rules in this geometry have been demonstrated to allow for complete and fast manipulation of single QDs [60].

1.2.2   Quantum Dot Parameters

While the actual values for the QD parameters vary between different experiments we will consider the following dot parameters as the "typical QD ensemble" quoted throughout this thesis. These values have been chosen, where relevant, to be closer to the favourable side of reported results with the assumption that the growth processes would be modified towards building the optimal memory conditions.

The trion excitation energy E_T can vary from 1 to 1.5 eV, where relevant we have used $E_T = 1.2$ eV here. Inhomogeneous broadening in E_T can be between 5 and 50 meV [50, 58], we will assume 10mev broadening here. While the ground state and trion splittings vary between experiments and depend on the magnetic field used [56, 60, 68, 83], they are generally on an order of 0.1mev when in large ($> 6T$) magnetic

fields, we will use $E_e \approx E_h \approx 0.1$ meV unless otherwise stated. Trion spontaneous decay time is around 1ns [50, 72], corresponding to $\Gamma_{31} = \Gamma_{32} = \Gamma_{42} = \Gamma_{41} = \Gamma = 0.004$ meV (which will be defined later in section 2.5.4). In a typical dot the decay rate Γ's may not be identical and will be influenced by the shape of the dot, we will however assume the decay rates to be identical. A standard deviation of about 20% [11] for the dipole strength has been measured between dots, which is not critical to any of the protocols considered here.

Spin lifetimes, the time taken before a spin flip on average occurs, are dependent on the magnetic field and have been measured in the 10's of milliseconds [44]. Decoherence times, defined by the loss of phase information of the qubit, have been measured to be of a few μs [61]. These times mean that initialisation must be performed within a time which is less than a few ms, ideally much less and the complete write to read storage time must be performed faster than μs.

Throughout the simulation code behind this thesis a consistent set of "code units" of 1 code unit of energy = 1meV and $\hbar = 1$ has been used. These units have also been used in all relevant plots unless otherwise specified.

1.2.3   QD Growth Limitations

The model given by section 1.2.1 is only valid for the light propagating normal to the growth plane because of the asymmetries of quantum dots in the growth axis, both from their width in the growth plane and their strain. For a QM using this geometry there would need to be many layers grown to assemble a large enough ensemble. The number of layers required is beyond current achievements. However, this is an active area of research, with current groups capable of creating 10's of layers of QDs [39, 76]. Because of these limitations we will now discuss the consequences of trying to store an in-plane propagating photon in QD ensembles, which would only require a few dot layers for the free space case, or a single dot layer for a planar waveguide case.

While there are many examples of optical experiments with light normal to the growth plane [79], there are significantly fewer with optical fields propagating along the growth plane, and these have not yet used strong fields to access the Voigt geometry, some examples: [49, 55]. Bastard 1988 [5] derives coupling strengths in quantum wells between radiation propagating in-plane and shows that only one polarisation, that with an in-plane electric field, couples to the heavy holes. Transitions for radiation polarised with its electric field normal to the growth direction are forbidden. We assume that this is generally true as the dots are thin in the z direction such that the results in reference [5] should be valid. For thicker dots, however there may be more bulk-like

properties which would potentially allow access to the full Voigt geometry given in figure 1.4b. In this thesis we therefore consider two cases, one with the full Voigt geometry and one with only access to a single polarisation.
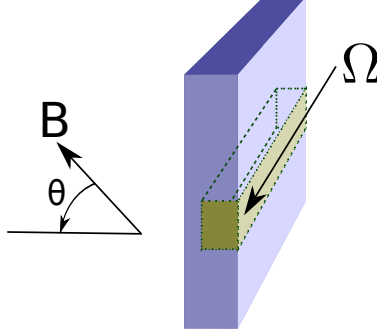

Fig. 1.5 The magnetic field and sample orientation for in-plane optical setup. Magnetic field B is placed at an angle ϕ to the growth direction. Only one polarisation couples to the heavy-hole QD transitions. The central band indicates the approximate volume of the sample assumed to be affected by incoming radiation which in general will not be confined within a waveguide.

As we assume do not have access to the out-of-plane polarisation, this leaves only the in-plane polarisation available for transitions. The coupling of this polarisation to the trion states depends on the orientation of the magnetic field, given by ϕ in figure 1.5. If the magnetic field is completely in-plane $\phi = \frac{\pi}{2}$ or completely out-of-plane $\phi = 0$ then the coupling of the in-plane propagating, in-plane polarised radiation will be to the equivalent of either the horizontally or vertically polarised transition in figure 1.4b respectively. Not both at the same time, however, such that each ground state couples to a different excited state. If however we consider the magnetic field orientations between $\phi = 0$ and $\phi = \frac{\pi}{2}$ then it will be possible to couple to all four Voigt couplings at the same time with a single polarisation, the Hamiltonian for this case is given in equation (1.5). This is the equivalent to applying a diagonally polarised radiation in the Voigt geometry.

$$
H_\phi = \begin{pmatrix}
\omega_B g_x^e & 0 & \cos(\phi)\Omega^* e^{-i\omega t} & \sin(\phi)\Omega^* e^{-i\omega t} \\
0 & -\omega_B g_x^e & \sin(\phi)\Omega^* e^{-i\omega t} & \cos(\phi)\Omega^* e^{-i\omega t} \\
\cos(\phi)\Omega e^{i\omega t} & \sin(\phi)\Omega e^{i\omega t} & E_T + \omega_B g_x^h & 0 \\
\sin(\phi)\Omega e^{i\omega t} & \cos(\phi)\Omega e^{i\omega t} & 0 & E_T - \omega_B g_x^h
\end{pmatrix} \tag{1.5}
$$

Because we are only interested in the case when we have coupling that links both ground states together via the excited levels we must set ϕ to a value in the interval $(0, \frac{\pi}{2})$, of which we choose $\frac{\pi}{4}$ to maintain equal strength to both h and v couplings.

$$H_{\frac{\pi}{4}} = \begin{pmatrix} \omega_B g_x^e & 0 & \frac{1}{\sqrt{2}}\Omega^* e^{-i\omega t} & \frac{1}{\sqrt{2}}\Omega^* e^{-i\omega t} \\ 0 & -\omega_B g_x^e & \frac{1}{\sqrt{2}}\Omega^* e^{-i\omega t} & \frac{1}{\sqrt{2}}\Omega^* e^{-i\omega t} \\ \frac{1}{\sqrt{2}}\Omega e^{i\omega t} & \frac{1}{\sqrt{2}}\Omega e^{i\omega t} & E_T + \omega_B g_x^h & 0 \\ \frac{1}{\sqrt{2}}\Omega e^{i\omega t} & \frac{1}{\sqrt{2}}\Omega e^{i\omega t} & 0 & E_T - \omega_B g_x^h \end{pmatrix} \tag{1.6}$$

This results in a Hamiltonian with the same couplings as shown in figure 1.4b but without the selection rules since there is only one incoming radiation mode. Differentiation between different signals must now be done spectrally rather than through polarisation, limiting the options for population transfer schemes. We will refer to this as the in-plane geometry and will investigate the consequences in section 3.

Chapter 2

Introduction: Optics Theory

Throughout this thesis we look at the interaction between isolated quantum systems and an electromagnetic (EM) field through the electric dipole interaction. A fully quantum approach should take into account all modes of the system:

$$H = H_{\text{matter}} + H_{\text{interaction}} + H_{\text{field}} \tag{2.1}$$

However, a general EM field in free space is constructed from an infinite number of modes, which is not possible to simulate in full. One approach is to only consider a limited number of modes, or in the case of the Jaynes-Cummings model, a single field mode. This is useful for cavity dynamics, but not for the free space models we consider here. Instead, we take a semi-classical approach to the interaction of light and matter since in the following work we only directly model many-photon interactions with QDs. That is to say that we treat the matter dynamics quantum mechanically and the EM dynamics classically:

$$H = H_{\text{matter}} + H_{\text{interaction}} \tag{2.2}$$

where

$$H_{\text{matter}} = \sum_i \sigma_i \mathcal{E}_i \tag{2.3}$$

and

$$H_{\text{interaction}} = \sum_{i \neq j} \sigma_{ij}^x \Omega_{ij}. \tag{2.4}$$

$\mathcal{E}_i$ is the energy of each level respectively. σ_{ij} is defined as the operator $|i\rangle\langle j|$ and σ_i's are the shift operators defined as $\sigma_i = \sigma_{ii}$. $\Omega_{ij} = \Omega_{ji}^* = \mu_{ij}\text{EF}$, where μ_{ij} is the electric dipole moment coupling the levels i and j and EF is the external electric field.

The Hamiltonian H for any system determines its dynamics. Specifically the state of a system $|\psi(t)\rangle$ is given by the time dependent Schroedinger equation, which throughout this thesis will be used with $\hbar = 1$:

$$\frac{d}{dt}|\psi(t)\rangle = -iH|\psi(t)\rangle \tag{2.5}$$

The time independent Schroedinger equation can be used to determine stationary states when the Hamiltonian of a system is time independent, or only changes with time adiabatically, where E is an eigenvalue of H:

$$E|\psi(t)\rangle = H|\psi(t)\rangle \tag{2.6}$$

2.1   Transformations

Physics contains many symmetries that allow us to look at a system from a different point of view without altering the dynamics of the system. For an example in classical mechanics, throwing a tennis ball on a speeding train, the ball will follow the same path despite having vastly different speeds to observers on the train and on the ground respectively. We can use the same principle in quantum systems to rewrite the dynamics in different frames. Firstly we can choose any energy zero that we wish by adding a factor of $\mathcal{E}_0$ onto each diagonal term:

$$H_{\text{matter}} = \sum_i \sigma_i(\mathcal{E}_i + \mathcal{E}_0) \tag{2.7}$$

Which does not change the evolution of the system. We can also consider a general transformation to a new set of basis states: $|\psi^U\rangle = U|\psi\rangle$, where U is any unitary transformation. Given a Hamiltonian H that generates the dynamics of $|\psi\rangle$ we can determine the Hamiltonian H^U that generates the dynamics of $|\psi^U\rangle$ [75]:

$$H^U = U^\dagger H U - iU^\dagger \dot{U} \tag{2.8}$$

A specific transform that we will use several times in this thesis is the rotating frame, where $U = e^{i\omega t S_z}$.

2.2   Continuous Wave Example

We now look, for example at the case of a two level system interacting with a monochromatic electric field. $\Omega = \Omega_0 \cos(\omega t + \phi)$ with $\mathcal{E}_1 = 0$ and $\mathcal{E}_2 = (\omega + \Delta)$, or since we are free to set the zero of energy however we wish this is identical to using $\mathcal{E}_1 = -(\omega + \Delta)/2$ and $\mathcal{E}_2 = (\omega + \Delta)/2$. ϕ determines the phase of the coupled field. For simplicity we will consider the case for $\phi = 0$.

$$H = \tfrac{1}{2}(\sigma_1 - \sigma_2)(\omega + \Delta) + \tfrac{1}{2}(\sigma_{12} + \sigma_{21})\Omega_0 \cos(\omega t) \tag{2.9}$$

The bare system (when $\Omega_0 = 0$) will undergo Larmor precession if the state is not completely in either of the eigenstates $|\psi_1\rangle$ or $|\psi_2\rangle$ at $t = 0$. This means the state of the system will rotate at an angular frequency given by $\omega_L = \mathcal{E}_2 - \mathcal{E}_1$, such that:

$$|\psi(t)\rangle = \begin{pmatrix} e^{-\frac{i}{2}(\mathcal{E}_2 - \mathcal{E}_1)t} \\ e^{\frac{i}{2}(\mathcal{E}_2 - \mathcal{E}_1)t} \end{pmatrix} |\psi(0)\rangle \tag{2.10}$$
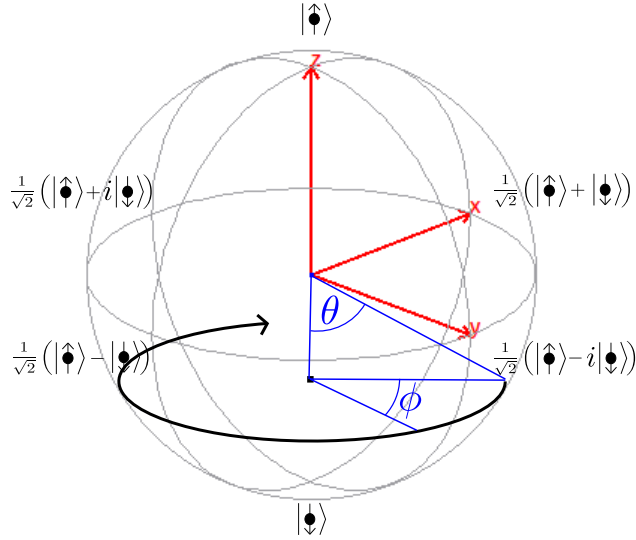
Fig. 2.1 Larmor precession on the Bloch sphere, the precession moves around the angle ϕ whilst keeping a constant angle θ .

We can rewrite $\Omega = \tfrac{1}{2}\Omega_0 \left(e^{i\omega t} + e^{-i\omega t}\right)$ which leaves two terms rotating in opposite directions. One of these terms will be rotating in the same direction as the bare system, and one will be counter rotating. The term rotating with the bare system is significantly closer to resonance and will dominate the dynamics of the system. The counter rotating term has considerably less effect on the system if $\Omega_0 \ll \omega$ and is zero

at the lowest order in perturbation theory [75]. The counter rotating term can also be considered as a second independent coupling which is highly detuned from resonance. This is discussed in section 2.5.1, or for the case $\Omega_0 \gg \omega$ this is discussed in detail in chapter 4. The elimination of the counter rotating term is known as the rotating wave approximation and will be used repeatedly within this thesis.

After using the rotating wave approximation to write $\Omega = \Omega_0 e^{i\omega t}$, we can then use the transformation from equation (2.8) with $U = e^{i\omega t \frac{1}{2}(\sigma_1 - \sigma_2)}$ to transform us into the rotating frame that eliminates the time dependence in equation (2.9), resulting in the following Hamiltonian:

$$H^r = \tfrac{1}{2}(\sigma_1 - \sigma_2)\Delta + \tfrac{1}{2}(\sigma_{12} + \sigma_{21})\Omega_0 \qquad (2.11)$$

It is always possible to find a time independent frame if the graph of the couplings between states does not contain any loops [28], meaning there are two or more paths to transfer population between two states. This will be elaborated on further in section 4.

2.3 Approximations

Although we are only looking at the state of two level systems to define a qubit, real systems contain many more levels that may or may not be important to the overall dynamics of the two levels of interest.

Particularly we may wish to reduce a large Hamiltonian to a two level effective-Hamiltonian by removing these extra energy levels, while still capturing the main dynamics of the levels in the system that make up our qubit. Firstly we can consider simply ignoring the coupling between an energy level and the levels of interest. Since there are near infinite energy levels in any real systems that could potentially be accounted for, ignoring energy levels is by far the most common method of simplification, usually with minimal discussion. The results are only valid if the eliminated state remains relatively unpopulated throughout the process. This leaves us with much smaller Hamiltonian, with dynamics that are easier to describe.

If we wish to reduce the Hamiltonian further we can eliminate energy levels that are important to the dynamics of the system but are not going to contain large amounts of population using Adiabatic Elimination. Adiabatic elimination leaves a smaller Hamiltonian which can more clearly isolate the dynamics of the levels of interest. It is a commonly used method, but is particularly non-rigorous and must be performed carefully, as we will now demonstrate.
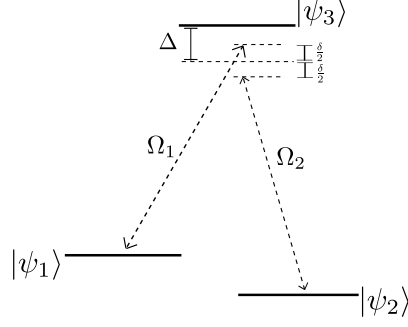
Fig. 2.2 The energy level diagram for the three level Λ system with the Hamiltonian given by equation (2.12), this setup will be used repeatedly in this thesis and is used to transfer population between the two lower states while keeping the upper, intermediate state relatively unoccupied. Δ is the detuning between the lower levels and the upper level, this is generally large to ensure that very little population is transferred into the upper state. δ is the two photon resonance detuning between the two lower levels, this is generally small to ensure rapid population transfer between the two lower states. The Ω's are determined by the external field and give the strength of the couplings between the three energy levels.

We first take the Hamiltonian associated with the three level Λ system shown in figure 2.2, already placed into the time independent rotating frame. We also include an arbitrary reference energy E_0 which should not affect the dynamics of the system:

$$H^r = \frac{1}{2} \begin{pmatrix} -\delta + E_0 & 0 & \Omega_1 \\ 0 & \delta + E_0 & \Omega_2 \\ \Omega_1^* & \Omega_2^* & 2\Delta + E_0 \end{pmatrix} \tag{2.12}$$

Here we are interested in the dynamics of levels one and two, and want to ignore level three. δ and Ω's are assumed to be small compared to Δ, which provides limits to the frequencies and strengths of the external fields. Whilst the Ω's could contain a complex phase we have not included this because it doesn't add any qualitative changes to the results. To demonstrate the adiabatic elimination process we use the Schröedinger equation (2.5) with the state $|\psi(t)\rangle = [|\psi_1(t)\rangle, |\psi_2(t)\rangle, |\psi_3(t)\rangle]$ and the Hamiltonian (2.12), while assuming that $\frac{d}{dt}|\psi_3(t)\rangle = 0$. This assumption, along with $|\psi_3(0)\rangle = 0$ leads to zero population being transferred into the upper state.

$$\begin{aligned} \frac{d}{dt}i|\psi_1(t)\rangle &= \tfrac{1}{2}(-\delta + E_0)|\psi_1(t)\rangle + \tfrac{1}{2}\Omega_1|\psi_3(t)\rangle \\ \frac{d}{dt}i|\psi_2(t)\rangle &= \tfrac{1}{2}(\delta + E_0)|\psi_2(t)\rangle + \tfrac{1}{2}\Omega_2|\psi_3(t)\rangle \\ \frac{d}{dt}i|\psi_3(t)\rangle &= \tfrac{1}{2}(\Omega_1|\psi_1(t)\rangle + \Omega_2|\psi_2(t)\rangle) + (\Delta + \tfrac{1}{2}E_0)|\psi_3(t)\rangle \end{aligned} \tag{2.13}$$

setting $\frac{d}{dt}|\psi_3(t)\rangle = 0$ leaves us with $|\psi_3(t)\rangle = -\frac{1}{2\Delta+E_0}(|\Omega_1\psi_1(t)\rangle + \Omega_2|\psi_2(t)\rangle)$. Substituting for $|\psi_3(t)\rangle$ into the first two equations and rearranging into the form $\frac{d}{dt}[|\psi_1(t)\rangle, |\psi_2(t)\rangle] = -iH_{\text{eff}}^r[|\psi_1(t)\rangle, |\psi_2(t)\rangle]$ gives:

$$H_{\text{eff}}^r = \frac{1}{2}\begin{pmatrix} -\delta - \frac{|\Omega_1|^2}{E_0+2\Delta} & \frac{\Omega_1\Omega_2}{2\Delta} \\ \frac{\Omega_1\Omega_2{}^*}{2\Delta} & \delta - \frac{|\Omega_2|^2}{E_0+2\Delta} \end{pmatrix} \tag{2.14}$$

This leaves the unphysical situation where the final dynamics are dependent on the frame in which the system is viewed. Other approaches [38] allow the dynamics to be analysed without eliminating the upper level, but the results from these have not been extended to more complicated Hamiltonians. The result above for $E_0 = 0$ is commonly used and successfully reproduces the actual dynamics of the Λ system, this is sometimes called the natural frame [13]. Specifically the natural frame is the frame where the energy zero is exactly half way between the two levels of interest. A more rigorous approach which solves the problem exactly is shown in [13] and confirms that the accepted result from the three level adiabatic elimination method is accurate, given the previous parameter assumptions. The result gives:

$$H_{\text{eff}}^r = \frac{1}{2}\begin{pmatrix} -\delta - \frac{|\Omega_1|^2}{2\Delta} & \frac{\Omega_1\Omega_2}{2\Delta} \\ \frac{\Omega_1\Omega_2{}^*}{2\Delta} & \delta - \frac{|\Omega_2|^2}{2\Delta} \end{pmatrix} \tag{2.15}$$

Throughout this thesis we will be considering the four level trion system shown in figure 1.4. In many papers the fourth level is simply ignored during the theoretical analysis (for example: [82]), leaving the three level Λ system from figure 2.2. The fourth level is ignored because level three is either placed on or near resonance with the lower levels of the system, or the transition $1-3-2$ is placed on or near two photon resonance, whereas the fourth level is placed off resonance on both measures. The elimination of the fourth level is then justified in the same way we justified the rotating wave approximation earlier, by assuming the counter rotating term is insignificant. One is left with a Λ system from which adiabatic elimination can be used again to obtain the two level dynamics.

However in this thesis we are interested in the effect of the fourth trion level on the system and therefore we want to consider the adiabatic elimination for the fourth level too. There is not currently a higher level extension to the method described in [13], but we can use the non-rigorous adiabatic elimination approach if we appropriately identify the natural frame we have checked this through a numerical comparison for every case used here. To complicate the setup we can see there is also no frame available that gives a completely time independent Hamiltonian. We choose the frame that would be

a natural frame and rotating frame for the Λ system $1 \to 3 \to 2$ since this transition provides the dominant dynamics, setting the zero energy to exactly half way between the two ground state levels. This frame includes a time dependence for the $1 \to 4 \to 2$ coupling, since we will be keeping this coupling off resonant for the simulations too. The choice of zero energy relative to the upper energy levels would be identical if $1 \to 4 \to 2$ transition was placed on resonance instead, and so leads to an identical effective Hamiltonian, and as such the exact choice appears irrelevant. This choice of frame leads to the following Hamiltonian:
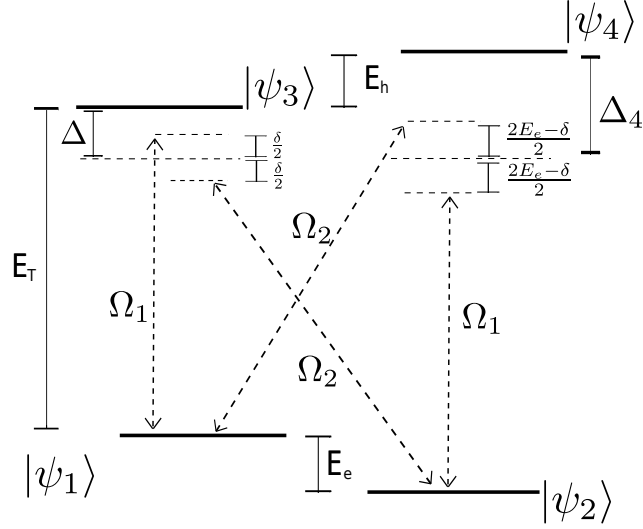

Fig. 2.3 The energy level diagram for the Hamiltonian given in equation (2.16). There are two couplings applied Ω_1 and Ω_2 which have the selections rules shown. Δ and Δ_4 are the large detunings between the lower levels and the level $|\psi_3\rangle$ and $|\psi_4\rangle$ respectively. δ is the two-photon resonance detuning and is generally small. E_e and E_h are the lower and upper state energy splittings.

$$H = \begin{pmatrix} \frac{\delta}{2} & 0 & \frac{\Omega_1}{2} & \frac{\Omega_2}{2}e^{-i\mathrm{E}_{\mathrm{e}}t} \\ 0 & -\frac{\delta}{2} & \frac{\Omega_2}{2} & \frac{\Omega_1}{2}e^{i\mathrm{E}_{\mathrm{e}}t} \\ \frac{\Omega_1}{2} & \frac{\Omega_2}{2} & \Delta & 0 \\ \frac{\Omega_2}{2}e^{i\mathrm{E}_{\mathrm{e}}t} & \frac{\Omega_1}{2}e^{-i\mathrm{E}_{\mathrm{e}}t} & 0 & \Delta_4 \end{pmatrix} \qquad (2.16)$$

Note that if equation (2.16) was rewritten in the natural frame of the $1 \to 4 \to 2$ transition instead the energy of the lower levels would be swapped, but the average energy would not be altered in comparison to the upper levels, further validating this choice of frame for adiabatic elimination. δ, Δ and Δ_4 are determined from the laboratory frame coupling terms $\Omega_1 e^{i\omega_1 t}$ and $\Omega_2 e^{i\omega_2 t}$, the trion creation energy E_T and the electron/hole Zeeman splittings E_e/E_h. This gives $\delta = E_e + \omega_1 - \omega_2$,

$\Delta = E_x - \frac{\omega_1 + \omega_2 + E_h}{2}$ and $\Delta_4 = E_T - \frac{\omega_1 + \omega_2 - E_h}{2}$. The four level Hamiltonian reduces to the following two level effective Hamiltonian when the two upper levels are eliminated through adiabatic elimination:

$$H_{\text{eff}} = \frac{1}{4} \begin{pmatrix} -2\delta + \frac{\Omega_1{}^2}{\Delta} + \frac{\Omega_2{}^2}{\Delta_4} & \left(\frac{1}{\Delta} + \frac{e^{-2i\mathrm{E_e}t}}{\Delta_4}\right)\Omega_1\Omega_2 \\ \left(\frac{1}{\Delta} + \frac{e^{2i\mathrm{E_e}t}}{\Delta_4}\right)\Omega_1\Omega_2 & 2\delta + \frac{\Omega_1{}^2}{\Delta_4} + \frac{\Omega_2{}^2}{\Delta} \end{pmatrix} \tag{2.17}$$

Here we can more clearly see the analogy between making the rotating wave approximation in section 2.2 and ignoring the fourth level from the system. In both cases we have two coupling terms, one which is on or close to resonance and one that can be considered to be rotating quickly if $\frac{\Omega_1\Omega_2}{4\Delta}, \delta \ll \mathrm{E_e}$. The coupling via the fourth level is rotating at a rate of $2E_e$.

2.4 Ensemble considerations

In this thesis we will consider each dot to be an independent system which is not affected by the state of the other dots in the ensemble, this allows us to simulate the dynamics of the dots individually, simplifying the problem considerably. Using this assumption is to say that we ignore dipole-dipole coupling, which appears to be generally valid even for moderately dense dot growth [10] and ignore the effects of scattered light on the other dots in the ensemble.

While many of the memory processes can be modelled by considering the dots individually, accurate modelling of the read and write processes cannot. Mapping a photon onto an ensemble spin wave requires considering the properties of the full ensemble, specifically these considerations result in the collective enhancement of $\sqrt{N}$ in the coupling between the dots and the photon mode over what would be naively assumed from the single dot case [23, 31]. A Gorshkov et al [31] and subsequent papers have thoroughly investigated the fidelity of these transitions including the case of free space and with the inclusion of inhomogeneous broadening (introduced in section 1.2). Their analysis is limited to Λ systems and does not include noise. We discuss the effects of these points later.

2.5 Common transfer protocols

This thesis investigates methods of population transfer within isolated quantum systems. In this section we cover some important transfer protocols and methods, while we have

simulated the results in all of the figures shown in this section for consistency with later sections, the results are commonly understood and available in the literature:

Rabi: Basic rotations around the two level Bloch sphere.

Stimulated Raman: Extending Rabi to multilevel systems.

Adiabatic Rapid Passage (ARP): Adiabatic population transfer with level crossings.

Pumping: Incoherent transfer using spontaneous emission.

2.5.1 Rabi

Rabi oscillations or Rabi flopping is the most basic population transfer beyond Larmor precession discussed in section 2.2, and viewed from an appropriate frame these are one and the same thing. More generally the population will rotate around the axis of the eigenbasis of the system, given by the eigenvectors, at a rate given by the energy splitting of the eigenvalues. During Rabi oscillations the direction of the eigenvectors are altered by the application of a strong resonant coupling by an angle θ given in figure 2.1. Because the state is no longer in the eigenbasis it then rotates, displaying the familiar Rabi oscillations.

The Hamiltonian for a two level example in the rotating frame is given by:

$$H^r = \tfrac{1}{2} \begin{pmatrix} -\Delta & \Omega \\ \Omega & \Delta \end{pmatrix}. \tag{2.18}$$

For a completely resonant system $\Delta = 0$ the eigenvalues are $\pm\frac{1}{2}\Omega$ and the eigenvectors, which give the quantisation direction, are $|\psi'_{1,2}\rangle = \frac{1}{\sqrt{2}}(|\psi_1\rangle \pm |\psi_2\rangle)$. If the system is in state $|\psi_1\rangle$, then it is now in a superposition of the eigenbasis with the coupling applied and will rotate with a frequency given by the eigenvalue splitting Ω. Once the coupling is removed the eigenbasis will return to $|\psi\rangle$ and the state will have rotated around by an amount given by the strength of the applied field multiplied by the time in which it was applied. This can be calculated from the area under the figure 2.4a, or the area between the eigenvalues in figure 2.4b. This gives a rotation angle of 5π for case of figure 2.4c, two and a half complete rotations.

If $\Delta \neq 0$ then the dressed state eigenvectors will not be orthogonal to the bare state eigenvectors and transfer will not be along a great circle on the Bloch sphere, so
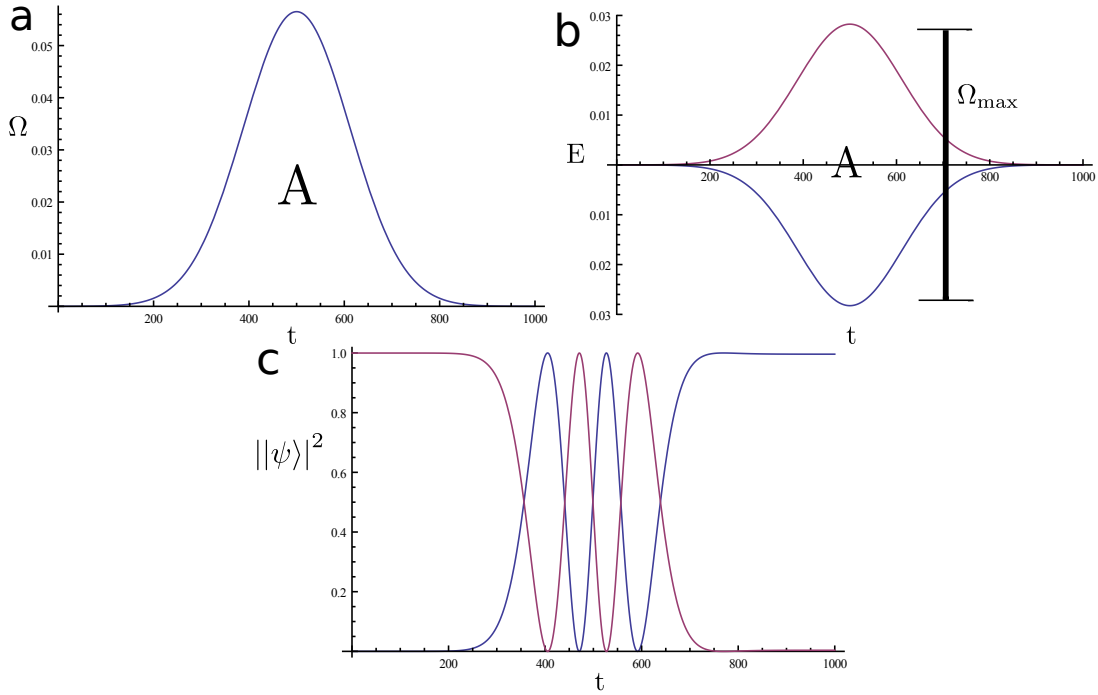
Fig. 2.4 The dynamics during Rabi oscillations. for $\Delta = 0$ a.) The intensity of the coupling Ω due to the external field over time, with a Gaussian profile. b.) The instantaneous eigenvalues of the Hamiltonian over time when viewed in the rotating frame. c.) The population of the bare states over time, several Rabi oscillations can be seen

complete transfer cannot occur. In general the peak height of the oscillations is given by

$$\frac{\Omega}{\sqrt{\Omega^2 + \Delta^2}} \tag{2.19}$$

and the rotation frequency is given by the energy splitting $\sqrt{\Omega^2 + \Delta^2}$.

If the same coupling is applied over a longer time scale, particularly so that the angle θ through which the state moves changes much more slowly than the energy splitting of the states:

$$\frac{d\theta}{dt} \ll \sqrt{\Omega^2 + \Delta^2}, \tag{2.20}$$

then the population will follow the eigenstates as they rotate. Viewed from the bare state basis the population temporarily mixes together in a superposition state, known as state mixing or adiabatic following.
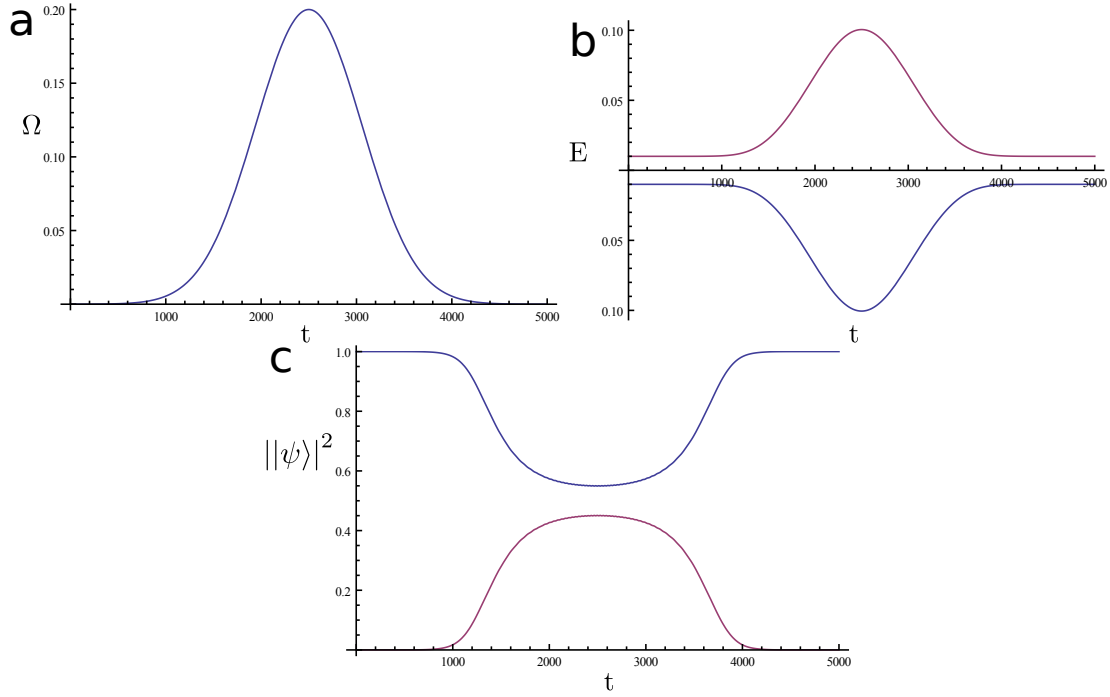
Fig. 2.5 a.) The Gaussian pulse that is applied adiabatically to two level system
b.) The eigenvalues of the Hamiltonian (2.18) with a small detuning $\Delta(= 0.02)$, the
eigenvalues of the systems still change significantly with the applied field. c.) The
state of the system follows the eigenstates of the system and temporarily creates a
large population in the previously unpopulated state. As the coupling is adiabatically
removed the state follows the eigenstate back to its original population.

The population moved during state mixing is calculated from the angle θ in figure
2.1 through which the eigenvalues move. The temporary population transfer is given
by:

$$\rho_{11} = \tfrac{1}{2} - \tfrac{1}{2}\cos(\theta) = \frac{1}{2} - \frac{\Delta}{2\sqrt{\Delta^2 + \Omega^2}} \tag{2.21}$$

Where ρ is the density matrix and $\rho_{ij} = |i\rangle\langle j|$. The state mixing population can
alternatively be calculated by recognising that the eigenvalues rotate by exactly half
the angle of the maximum Rabi oscillation height from equation (2.19), which gives a
population transfer of:

$$\rho_{11} = \sin\left(\frac{1}{4}\arccos\left(1 - \frac{2\Omega^2}{\Delta^2 + \Omega^2}\right)\right)^2 \tag{2.22}$$

Equations 2.21 and 2.22 are equivalent, demonstrating the connection between
state mixing and Rabi oscillations.

While state mixing will be a visible effect in many of the simulations shown throughout this thesis, it generally does not affect the results significantly because the process is reversed completely as the coupling is removed. Exceptions to this occur if the population is transferred into an unstable state or the population is intentionally manipulated with adiabatic following through Adiabatic Rapid Passage 2.5.3.

2.5.2 Stimulated Raman

The stimulated Raman transition is the natural extension to Rabi flopping for transfer between two levels which are not directly coupled together. The process is used to transfer population population between two unconnected states, for example the two lower levels in the Λ system in figure 2.2, through an intermediary level whilst not significantly populating the intermediate level. The Hamiltonian is given by equation (2.23), however this protocol can be viewed best from the perspective of the two level effective Hamiltonian given in equation (2.15) in which the upper of the three Λ system levels was removed using adiabatic elimination. If δ is set to zero and $\Omega_1 = \Omega_2$ then the system will be on two photon resonance. The two level subsystem can now be manipulated to create Rabi transfer as described in the previous section, an example numerical simulation for the three level Λ system is shown in figure 2.6 with $\Delta = 1$, $\delta = 0$ and $\Omega_{1\text{max}} = \Omega_{2\text{max}} = 0.101$. As in the previous section the number of oscillations depends on the intensity of the coupling and the time for which the coupling is applied, the rotation angle through which the population is rotated is given by the area A in figure 2.6b. The numerical simulation result shown in figure 2.6c is for the three level problem, however it is indistinguishable to the eye from the result of a simulation on the two level system after adiabatic elimination.

$$H^r = \frac{1}{2} \begin{pmatrix} -\delta & 0 & \Omega_1 \\ 0 & \delta & \Omega_2 \\ \Omega_1^* & \Omega_2^* & 2\Delta \end{pmatrix} \tag{2.23}$$

The maximum height of the oscillations is also dependent on the two-photon detuning δ. However, if intensities of the couplings are not equal, $|\Omega_1| \neq |\Omega_2|$, then there will also be a time dependent Stark shift that will cause a time dependent detuning in the two level system. Assuming δ is not equally time dependent to cancel out the Stark effect there cannot then be complete population transfer. This requires a careful tuning of δ which is dependent on the Ω's if complete transfer is required.
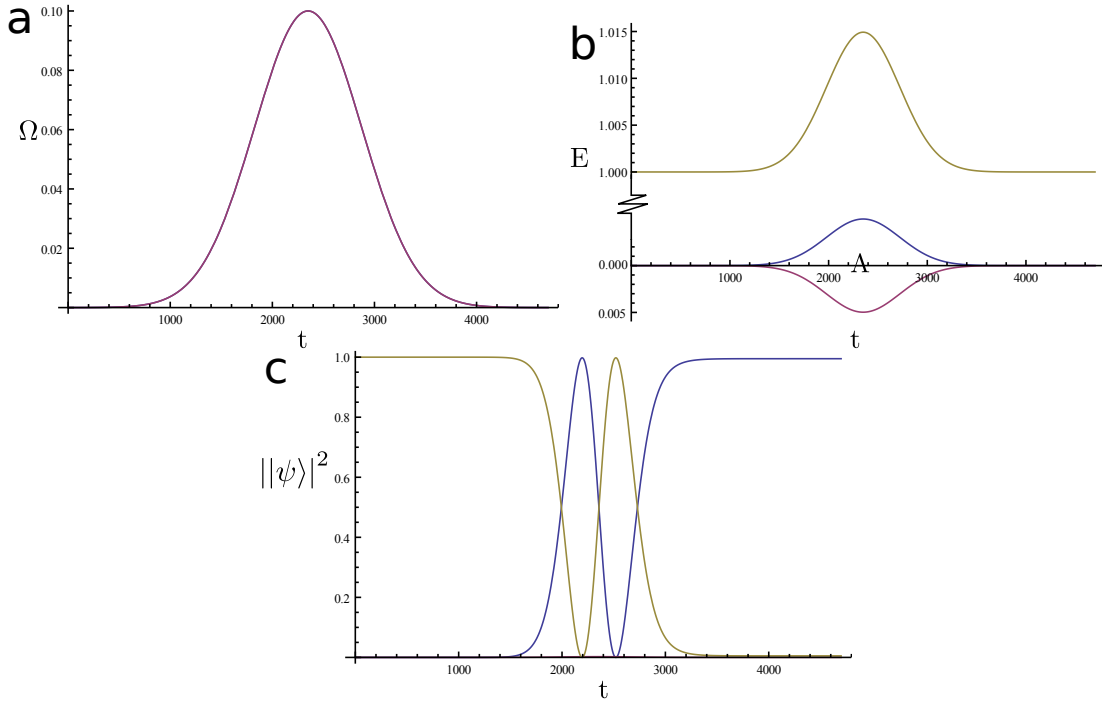
Fig. 2.6 The dynamics during a Stimulated Raman transition a.) The strength of the couplings during the transition, there are two couplings with identical strengths in this example, using different strength couplings will cause a detuning. b.) The eigenvalues of the Hamiltonian in the rotating frame. The area A determines the angle through which the system rotates, determining the number of oscillations c.) The population of the bare states throughout the transition, showing one and a half full oscillations

2.5.3 Adiabatic Rapid Passage

Adiabatic Rapid Passage (ARP), also know as a Landau-Zener transition is an extension of state mixing mentioned in section 2.5.1. It occurs whenever two eigenstates slowly intersect, such that the population follows the states, but which are also coupled strongly together, such that the eigenvalues also repel each other, creating an avoided crossing. This is shown in figure 2.7b. If this crossing happens slowly enough the population in the two states will follow the rotation in the eigenbasis completely [41]. This occurs when $\frac{d\theta}{dt} \ll |\Omega|$ where $\frac{d\theta}{dt}$ is the rate of change of the angle of the eigenvectors of the system and Ω is the coupling strength between the levels. If the initial state is $|1\rangle$ or $|2\rangle$ then θ corresponds to the θ in figure 2.1, however if the initial state is another state the relevant angle θ is the angle through which the state moves from its initial position, in whichever direction it moves (whilst in the rotating frame).

The ARP transition is very important for manipulating systems where the exact parameters are unknown, because the small changes in the parameters will not signifi-

cantly affect the fidelity of the transition assuming it is performed slowly enough. This is contrary to population transfer through a Rabi rotation, where the angle through which the states rotate is very sensitive to the coupling strengths and detunings in the system. The disadvantage of ARP is that it is only capable of performing complete population inversions (π rotations) to a high fidelity.

An ARP transition can occur between two levels in any size system, reference [80] creates an ARP transition between two levels in quantum dots for example. The Hamiltonian for a two level transition is given by:

$$H^r = \begin{pmatrix} -\delta(t) & \Omega \\ \Omega & \delta(t) \end{pmatrix}, \tag{2.24}$$

where Ω is non-zero near t_0 and $\delta(t) = \Delta_t \times (t - t_0)$ where we can see that t_0 is the time at which the avoided crossing occurs and Δ_t is the rate at which the eigenvalues cross. The eigenvalues over time for this system are $\sqrt{\Omega^2 + \delta(t)^2}$ and are shown in figure 2.7b

The transition transfers population between the two states and will occur completely if $\frac{d\delta(t)}{dt} \ll |\Omega^2|$, whist if the transition is performed faster the fidelity of transfer, originally derived by Landau and Zener[45, 84]. is given by:

$$|\alpha|^2 = 1 - \sigma = e^{-\frac{|\Omega|^2 \pi}{\Delta t^2}}, \tag{2.25}$$

where we consider the case when the state is initially in $|\psi_1\rangle$ and finishes the transition in state $\alpha|\psi_1\rangle + \beta|\psi_2\rangle$, σ is the fidelity of the transfer. This is the usually the stated formula, however it is only valid for the specific case for starting in an eigenstate, $\alpha_0 = 0, 1$. If the initial population is in a superposition of states $\alpha_0 \neq 0, 1$, as will generally be the case, the unitary transform is given by: [1, 69, 71]

$$U_{ARP} = \begin{pmatrix} \cos\frac{\chi}{2} & e^{i\phi}\sin\frac{\chi}{2} \\ -e^{-i\phi}\sin\frac{\chi}{2} & \cos\frac{\chi}{2} \end{pmatrix}, \tag{2.26}$$

where $\sin\frac{\chi}{2}^2 = 1 - \sigma$ and the angle ϕ determines the angle on the Bloch sphere through which the population is transferred. While this does not affect the outcome of the transition if the transfer is complete, ϕ will determine the phase of the final population during incomplete transfer, which will be discussed when we encounter a consequence of this phase in section 4.5.1.

The example ARP transfer is shown in figure 2.7. A smoothly varying coupling Ω, in this case a Gaussian, is applied to a two level system with energy levels that cross when viewed from the rotating frame. the bare state energies (dotted) are shown to

cross and the eigenvalues of the system are shown to undergo an avoided crossing. In the laboratory frame this crossing can be induced by a chirped coupling term which changes frequency to pass through resonance with the two level system, or alternatively a modification of the two level systems energy levels to pass through resonance with a constant frequency coupling. The dressed states picture will be identical for both of these cases and both will be used in this thesis.
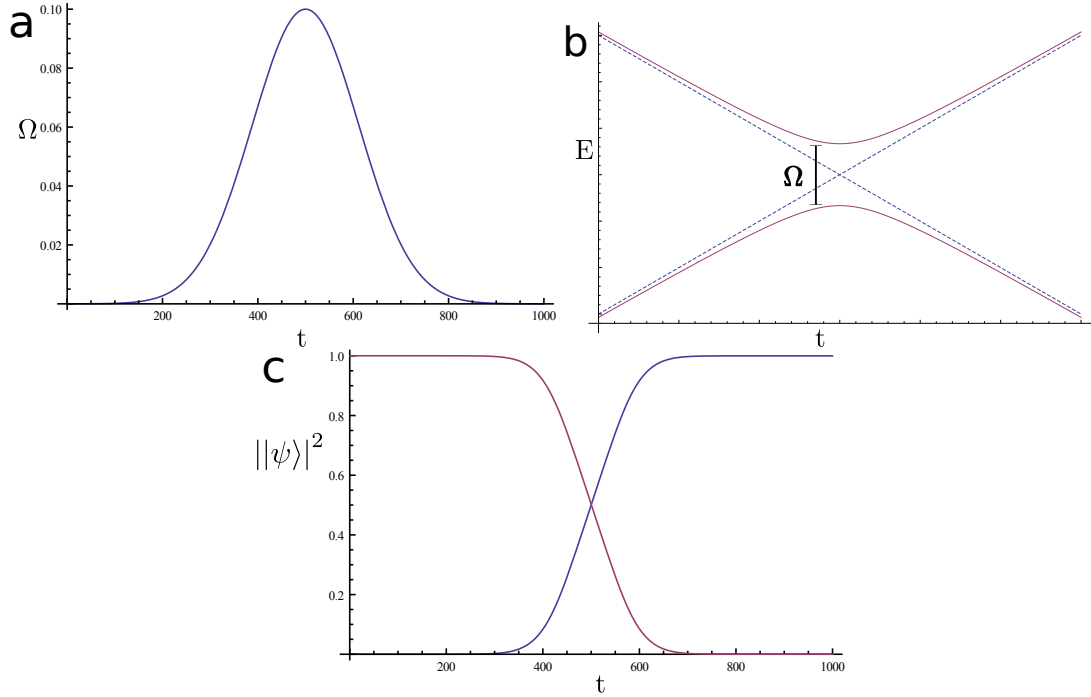

Fig. 2.7 a The strength of the coupling Ω used in c. which is given by a Gaussian profile, b The eigenvalues of a two level system going through a Landau-Zener crossing. Dotted lines correspond to the bare state energies, or for $\Omega = 0$ solid lines demonstrating an avoided crossing. c The population during the transition with $\Omega_m ax = 0.1$ and $\frac{dE}{dt} = 1/1000$.

In general ARP can occur in any size Hamiltonian, through any pair of states whose eigenvalues undergo an avoided crossing. Some different protocols using ARP are introduced in chapter 3. Particularly STImulated Raman Adiabatic Passage: STIRAP, Raman Chirped Adiabatic Passage: RCAP and Stark Chirped Raman Adiabatic Passage: SCRAP.

2.5.4 Incoherent Pumping

The previous models shown in this chapter are based upon equation 2.5 and only considered the interaction of the quantum system with one or two coupling terms Ω.

This is sufficient if interactions with the surrounding environment are negligible, but not realistic for many situations. We will be considering quantum dots in free space throughout much of this thesis. In free space we need to not only consider the single laser mode Ω but also the interactions with all other possible optical modes.

The optical modes form a continuum of states in free space which are treated as a reservoir of harmonic oscillators [16], computing the state of the whole environment is not a practical solution. The interactions with the environment can be in the form of spontaneous emission into the reservoir causing a decrease of energy in the system or absorption of a photon from the bath leading to an increase of the energy of the system. In later sections we assume that the number of photons in the environment is small enough to be able to discount the possibility of absorption. This is also known as the zero temperature approximation. We also take the Markov approximation, which assumes that the interaction of the system with the environment does not depend on the previous state of the system. This means that any information transferred into the environment is therefore lost. This is a non-unitary process which we model with a master equation approach, in which the environment is traced out to leave the original system dynamics and some non unitary terms which account for the interaction with the environment. This results in the following master equation, known as the Lindblad equation. [16, 52]

$$\frac{d}{dt}\rho = -i[H,\rho] - \frac{1}{2}\sum_{(i,j)} \Gamma_{ij}\left(\sigma_{ij}^{+}\sigma_{ij}^{-}\rho + \rho\sigma_{ij}^{+}\sigma_{ij}^{-} - 2\sigma_{ij}^{-}\rho\sigma_{ij}^{+}\right), \qquad (2.27)$$

Where the Γ's account for the rate of spontaneous emission into the environment.

Spontaneous emission is an incoherent process. Incoherent processes are non-unitary and will destroy or degrade any information stored in the quantum state. Whilst this is often something to be avoided within quantum computing, pumping can be used to take advantage of the incoherent process to wipe information of the system's previous states and place the system in a new, known state. Incoherent processes are therefore to be avoided during any computational step but can be used effectively to initialise a state.

For a three level Λ system spontaneous emission occurs from the excited state (3) to the two lower energy states (1,2), which means $\Gamma_{32}, \Gamma_{31} = \Gamma$ and $\Gamma_{ij} = 0$ for all $\{i,j\} \neq \{3,2\}$ or $\{3,1\}$. This system can be used to generate incoherent pumping by applying a strong resonant coupling between the lower level that is to be evacuated and the upper level. This transfers population continuously between those two levels. The upper level $|3\rangle$ is an excited state that can decay through spontaneous emission into the

environment with roughly equal probability down to the two lower states. The lower state $|2\rangle$ that is not coupled to the pumping field accumulates population which cannot be transferred back to either of the other levels as there is no coupling to transfer the population out, until eventually (almost) all of the population is transferred into state $|2\rangle$. The Hamiltonian for resonant pumping in a Λ system is as follows:

$$H = \frac{1}{2} \begin{pmatrix} 0 & 0 & \Omega \\ 0 & E_2 & 0 \\ \Omega & 0 & 2\Delta \end{pmatrix} \tag{2.28}$$

Where Δ gives the detuning of the coupling from resonance and Ω the strength of the coupling, this is equivalent to the Hamiltonian in (2.12) with E_0, δ, $\Omega_2 = 0$. E_2 is the (arbitrary) energy of the second level. The approximate population transfer rate due to pumping can be found through putting the Hamiltonian (2.28) into equation (2.27) with the relevant Γ's mentioned above. Applying adiabatic elimination of the upper state ($|3\rangle$) gives the following equation:

$$\frac{d}{dt}\rho_{11} = -\frac{\Gamma\Omega^2\rho_{11}}{4\left(\Gamma^2 + \Delta^2\right) + \Omega^2} \tag{2.29}$$

Which results in the following time evolution:

$$\rho_{11} = e^{-\frac{t\Gamma\Omega^2}{4\Gamma^2 + 4\Delta^2 + \Omega^2}} \tag{2.30}$$

This is assuming that the upper state never has a significant amount of population. For the case when a large population is transferred into the upper state the transfer must be considered in terms spontaneous decay from this upper state population. The transfer rate from ρ_{33} is then given by $\frac{d}{dt}\rho_{33} = \rho_{33}\sum^i \Gamma_i$ where the Γ_i's are all the decay paths out of state 3.

2.5.5 Transfer Protocol Summary

We introduced Rabi oscillation and its multilevel extension the Stimulated Raman transfer that can rotate the state of a system by an arbitrary angle on the Bloch sphere defined by the strength and time of the pulse applied. The protocols are therefore not robust on systems with inhomogeneities since these will alter the rotation angle and therefore the final state reached. The coupling must be turned on and off quickly to ensure that the system does not simply undergo state mixing which induces no overall population transfer.
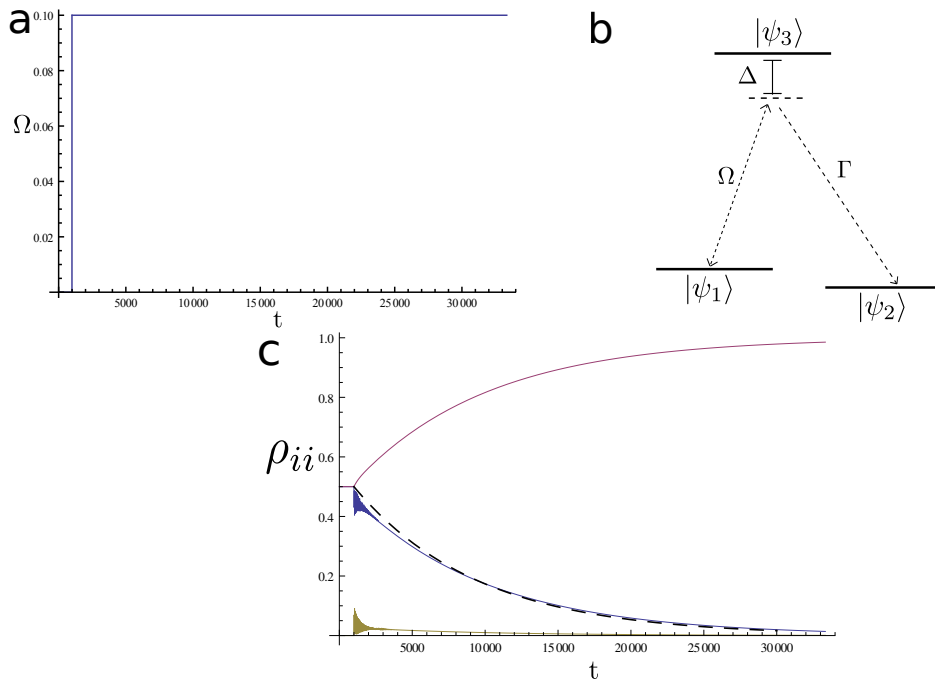
Fig. 2.8 a.) The coupling between $|\psi_1\rangle$ and $|\psi_3\rangle$ is turned on at a particular time and left running until the desired fidelity of pumping is reached. This can be of any pulse shape as long as the pump is strong enough to move a significant amount of population between the states. Here we use a constant pump strength b.) The energy level diagram for resonant pumping, for efficient pumping $\Omega >> \Delta$. Γ shows decay down to $|\psi_2\rangle$ via spontaneous emission. Emission also transfers population from $|\psi_3\rangle \rightarrow |\psi_1\rangle$ but this population will then be transferred back via the coupling Ω. c.) The simulated population throughout the pumping process, showing diagonal terms of the density matrix ρ_{ii}. The oscillations are Rabi oscillations due to the speed in which the pump is turned on, an adiabatically applied pump would avoid these. The dotted line is the fit given by equation (2.30).

Adiabatic Rapid Passage is a robust protocol but can only reliably perform π rotations, which is sufficient for spin echo. This makes it a very useful protocol for ensembles with inhomogeneous broadening but is not applicable to applications that require arbitrary rotations. The protocol requires the state to follow the eigenbasis and so must be performed adiabatically.

Incoherent pumping uses spontaneous emission into the background environment to pump the system into a particular state and will destroy any information in the state in the process. The transfer follows an exponential decay towards the final state. Spontaneous emission is useful for initialising systems but causes unwanted decoherence when it affects the system during any coherent process, such as the memory protocol considered here and generally needs to be minimised.

Chapter 3

Quantum Memories

In this section We will look at the feasibility of using GaAs self assembled QDs as an optical quantum memory. We investigate the four stages: Initialisation, Write, Storage and Read.

Plots in this chapter display the "code units" of 1 code unit of energy = 1meV and $\hbar = 1$ unless otherwise specified.

3.1 Initialising QD ensemble

Initialisation requires moving the state of every dot in the entire ensemble to a known state, in our case one of the ground states. This needs to be independent of what state the dot was in previously, for this process we will be using pumping introduced in section 2.5.4. Pumping in a Λ system has no theoretical limit to the fidelity the pumping can reach because there is no mechanism to transfer population out of the final energy level. However, pumping in the Voigt geometry (figure 3.1) effectively has two pumps: one pumping from $|1\rangle \to |2\rangle$ and one from $|2\rangle \to |1\rangle$, since applying a single laser field of any polarisation will couple to both ground states simultaneously and act to pump population in both directions. We will first consider pumping with horizontally polarised light, since this gives the largest gap between the two resonances, and therefore, we would assume, the best initialisation fidelity. We will also consider the in-plane geometry case discussed in section 1.2.3, which from a modelling perspective is the equivalent of using an out-of-plane diagonally polarised laser that couples equally to both the horizontally and vertically polarised dipole transitions. This case therefore provides four resonant conditions.
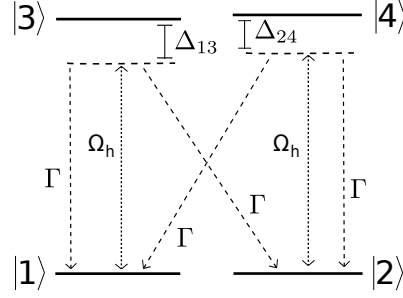
Fig. 3.1 Pumping in the Voigt geometry with horizontally polarised light Ω_h results in direct couplings only between levels $1 \to 3$ and $2 \to 4$. However, due to spontaneous decay from the upper states, population can be transferred down through any of the Γ decay routes shown.

The evolution of an individual dot is given by the Lindblad master equation (2.27) with $\Gamma_{31} = \Gamma_{32} = \Gamma_{42} = \Gamma_{41} = \Gamma$ else $\Gamma_{i,j} = 0$ and H given by:

$$
H = \begin{pmatrix}
-\frac{\Delta_{13}}{2} & 0 & \frac{\Omega}{2} & 0 \\
0 & -\frac{\Delta_{24}}{2} & 0 & \frac{\Omega}{2} \\
\frac{\Omega}{2} & 0 & \Delta_{13} & 0 \\
0 & \frac{\Omega}{2} & 0 & \Delta_{24}
\end{pmatrix}
\tag{3.1}
$$

The system will come to equilibrium when the pump rate from both pumps is equal. Equation (2.30) gives the approximate pump rate for pumped Λ system with a single pump when $\Delta > \Omega$, however we can obtain the equilibrium point directly from considering the steady state solution of the four-level equations from which we can derive the populations to which the states will asymptotically approach. This achieved by setting $\frac{d}{dt}\rho = 0$ in equation (2.27), providing the following solutions:

$$
\begin{aligned}
\rho_{11\infty} &= \frac{4\left(\Gamma^2 + \Delta_{13}{}^2\right) + \Omega^2}{4\left(2\Gamma^2 + \Delta_{13}{}^2 + \Delta_{24}{}^2 + \Omega^2\right)} \\[2mm]
\rho_{22\infty} &= \frac{4\left(\Gamma^2 + \Delta_{24}{}^2\right) + \Omega^2}{4\left(2\Gamma^2 + \Delta_{13}{}^2 + \Delta_{24}{}^2 + \Omega^2\right)} \\[2mm]
\rho_{33\infty} &= \frac{\Omega^2}{4\left(2\Gamma^2 + \Delta_{13}{}^2 + \Delta_{24}{}^2 + \Omega^2\right)} \\[2mm]
\rho_{44\infty} &= \frac{\Omega^2}{4\left(2\Gamma^2 + \Delta_{13}{}^2 + \Delta_{24}{}^2 + \Omega^2\right)}
\end{aligned}
\tag{3.2}
$$

The initialisation fidelities dependence on the parameters Ω, Γ are shown in figures 3.2 and 3.3 and are potentially counter-intuitive. The stronger the laser coupling and the stronger the coupling to spontaneous emission the weaker the fidelity of transfer will be, although the faster the system will tend to the equilibrium.
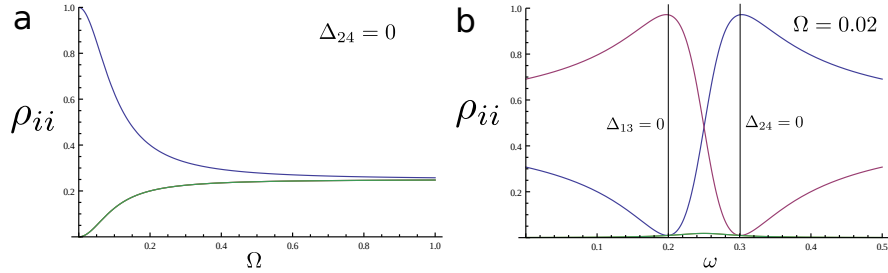

Fig. 3.2 Steady state solutions for the population of all four states $\rho_{11}, \rho_{22}, \rho_{33}, \rho_{44}$ under monochromatic pumping as given by equation (3.2). a.) shows the steady state solution dependence on laser strength Ω while on resonance $\Gamma = 0.001$. For a low enough Ω the system will pump into level ρ_{22} to a high fidelity. b.) shows the strong frequency dependence on the pumping fidelity with $\Gamma = 0.001$ and $\Omega = 0.02$. For a complete view of the parameter space see figure 3.3.

This dependence on Ω is due to the increased strength of the detuned pump even while the other pump is close to resonance and highlights the importance of optimising the properties of an initialisation pulse for any individual system for both the time to reach the fidelity and the final fidelity desired. This trade off is not present while pumping in a Λ system.

Resonant pumping has already been performed in individual QDs [81], however the technique does not allow for the initialisation of an ensemble. An ensemble of inhomogeneously broadened dots cannot be initialised with a monochromatic laser since, due to the inhomogeneous broadening, there is no single resonance frequency that can be used. We must consider a different approach which we introduce next.

3.1.1 Sweeping Pump

The problem with attempting to initialise a large ensemble of inhomogeneously broadened QDs is that no two dots share the same resonant condition, the inhomogeneously broadened energies ΔE_T are generally spread by at least fifty times the gap between the two resonances (section 1.2.2). If a single frequency is chosen it is only possible to initialise a small number of the QDs. Instead we propose a slowly sweeping pump frequency ω that sweeps through the full dot range. The higher energy transition of each dot will always pump into the same state for each dot, therefore as the pump
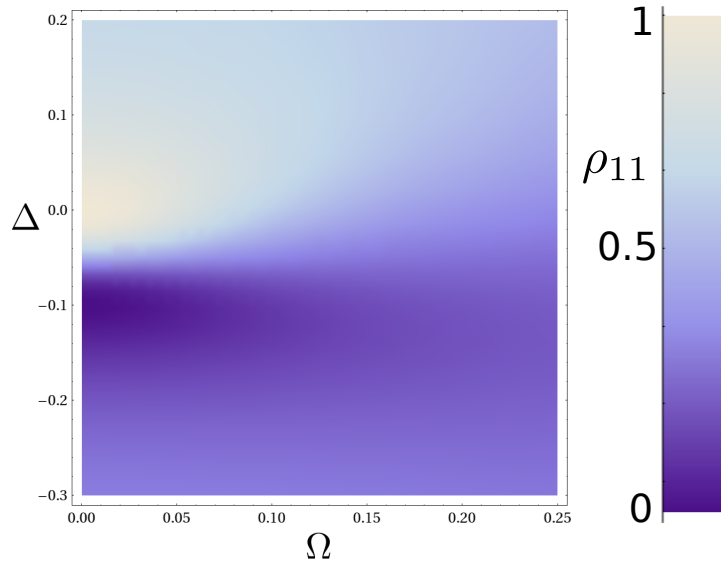
Fig. 3.3 Density plot of steady state solution for the dot state under a monochromatic pump. The two resonance cases where populations are pumped completely into either $|1\rangle$ or $|2\rangle$ are shown as dark and light respectively. An increase in Ω increases reverse pumping, reducing the final fidelity of the pumping even when on resonance with one of the dot states. Figure 3.2 provides cross sections for the $\Omega = 0$ and Δ on resonance cases.

frequency sweeps through the two resonances of each dot it will first reverse pump, and then pump into the desired state, initialising each dot in turn as they fall onto resonance with the pump. There will be an amount of reverse pumping as the frequency continues past the resonances of the dot as we can infer from figures 3.2b and 3.3.

3.1.2 Pump Model

From equation (2.29) which gives the pumping in a single Λ system we can derive the transfer rate between two ground state levels. We treat the transfer as two independent transfer rates:

$$\frac{d}{dt}|\psi_1(t)\rangle = \Gamma\Omega^2\left(\frac{1-|\psi_1(t)\rangle}{4\left(\Gamma^2+\Delta^2\right)+\Omega^2} - \frac{|\psi_1(t)\rangle}{4\left(\Gamma^2+(E_e+E_h+\Delta)^2\right)+\Omega^2}\right), \qquad (3.3)$$

where $\Delta = 0$ is the condition for $\Delta_{13} = 0$ and $\Delta_{24} = E_e + E_h$, $\psi_1(t) = 1 - \psi_2(t)$ as we assume no significant population is in the excited states. This is a questionable assumption for resonance conditions while $\Omega > \Gamma$, but has been found to hold well for all relevant cases presented here and also we shall see later that the best initialisation

parameters are also for $\Omega < \Gamma$. Figure 3.4 shows both full 4-level numerical simulations (points) and the solution to the two level equation (3.3) (line) and demonstrates that this approximation holds well for the cases we consider here.
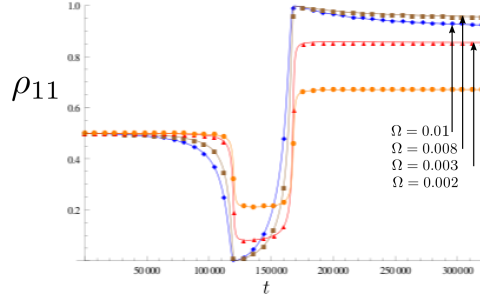

Fig. 3.4 Pumping with a single polarisation and a linear chirp. $\Gamma = 0.004$, $E_e + E_h = 0.2$ and $\frac{d}{dt}\Delta = 6 \times 10^{-5}$. The population of the dot transfers first into level 2 and then back into level 1 as the pulse becomes on resonance with the 1-3 and 2-4 transitions. Four examples for different pump field strengths Ω are shown. Points correspond to complete 4-level simulations, lines correspond to the two level approximation in equation 3.3.

The in-plane geometry initialisation discussed in section 1.2.3 has dynamics governed by the Hamiltonian given by equation (1.6). This Hamiltonian has the same four couplings as the Voigt geometry, but with only one incoming laser coupling Ω that couples to all four transitions. We assume again spontaneous emission dominates the effects allowing us to use the same assumption that we made for equation (3.3). This is a safe assumption since in the long time limit oscillations due to the couplings will be damped leaving only state mixing. State mixing is insignificant if $\Omega \ll E_e$, which is true for our cases here. This leads to four resonances and the following population evolution after extending the model in equation (3.3):

$$\frac{d}{dt}|\psi_1(t)\rangle = \Gamma\Omega^2 \left(\frac{1 - |\psi_1(t)\rangle}{4\left(\Gamma^2 + \Delta^2\right) + \Omega^2} - \frac{|\psi_1(t)\rangle}{4\left(\Gamma^2 + (E_e + E_h + \Delta)^2\right) + \Omega^2} + \frac{1 - |\psi_1(t)\rangle}{4\left(\Gamma^2 + (E_e + \Delta)^2\right) + \Omega^2} - \frac{|\psi_1(t)\rangle}{4\left(\Gamma^2 + (E_h + \Delta)^2\right) + \Omega^2} \right) \tag{3.4}$$

For both equation (3.3) and equation (3.4) we will consider a linearly swept pump, sweeping through the full energy range of the inhomogeneously broadened ensemble. This corresponds to a linear sweep of the detuning Δ, such that Δ passes from negative to positive for each dot or visa versa during the pump. The population transfer for an example sweep is shown in figure 3.4.

We find that there are two distinctly different behaviours that occur for the in-plane geometry, dependent on whether $E_h < E_e$ or $E_h > E_e$. This is because of order of the resonance conditions that can be seen in equation (3.4) changes. In the former the population is pumped $\{|\psi_0\rangle \to |2\rangle \to |1\rangle \to |2\rangle \to |1\rangle\}$, whereas in the latter case the population is pumped $\{|\psi_0\rangle \to |2\rangle \to |2\rangle \to |1\rangle \to |1\rangle\}$. For the latter case the second two pumps both pump into the same level, leading to a higher fidelity initialisation. Reversing the pump direction reverses the order of the pumps and therefore which spin state is initialised, but does not change the behaviour which is still determined by E_e and E_h. The difference can be seen in figure 3.5.
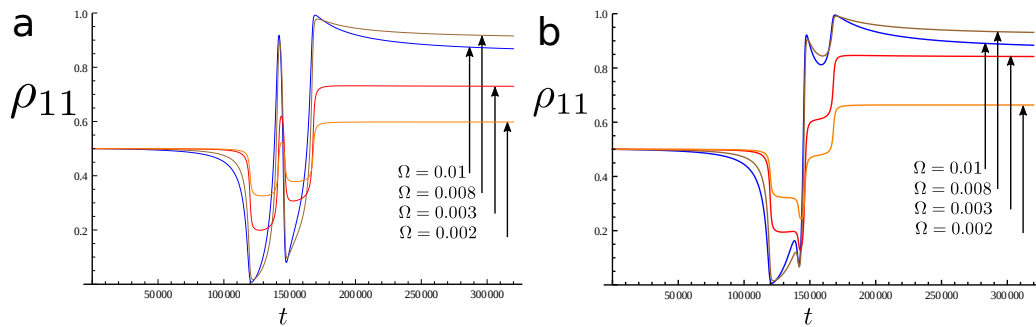

Fig. 3.5 In-plane pump sweep, where $\Omega_h = \Omega_v$. Simulations with the same parameters as for figure 3.4 with the polarisation of the electric field rotated by $\frac{\pi}{2}$, such that $\Omega_h, \Omega_v \to \frac{1}{\sqrt{2}}\Omega$. For a.) $E_h = 0.09$, $E_e = 0.11$ and for b.) $E_h = 0.11$, $E_e = 0.09$.

We can see from closely comparing the final state values in figures 3.4 and 3.5b that although the in-plane initialisation has a similar fidelity for $E_h > E_e$ for this short sweep example, there is also a faster transfer out of the initialised state. When extended to the large energy sweeps required for initialisation of an ensemble this will mean both in-plane cases will perform poorly compared to the out-of-plane, single pump polarisation case in figure 3.4. This shown more clearly later in figure 3.9.

For a inhomogeneously broadened ensemble the sweep would have to last considerably longer than in figures 3.4 and 3.5. Sweeping through a larger energy allows for more transfer out of the desired state if Ω is too large. For a typical ensemble (section 1.2.2) the inhomogeneous broadening Δ_E is at least $50 \times (E_e + E_h)$. An example initialisation of a typical QD ensemble using a horizontally polarised pulse is shown in figure 3.6. Firstly we can see that the mechanism does work for a proof of concept at least, with a 96% fidelity in this case. The pumping fidelity in the ensemble does depend on the excitation energy E_T for each dot, the dots initialised first will be reverse pumped for longer. However we can see from figure 3.6b that the variation
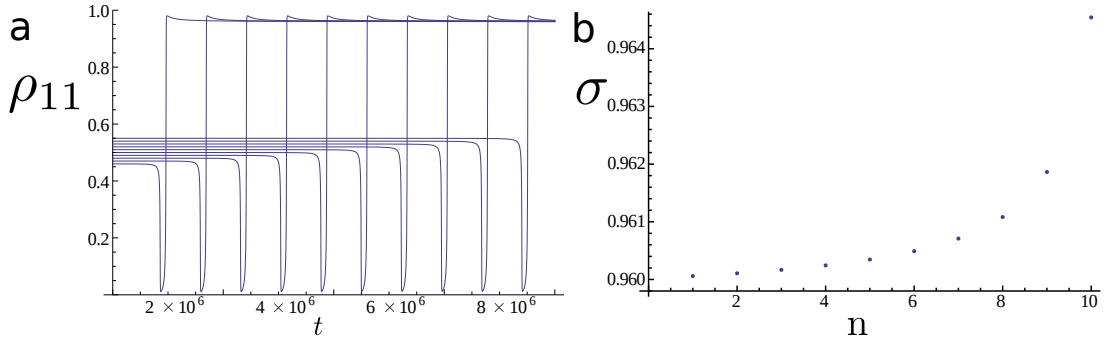
Fig. 3.6 a.) An example initialisation of an ensemble of dots with 10meV inhomogeneous broadening, starting values chosen for clarity. $\Omega = 0.003$ and frequency sweep rate 1.9×10^{-6}. Each dot is initialised in turn as the frequency of the sweep passes through resonance. b.) The final fidelity σ of each dot in the ensemble, a lower the excitation energy E_T results in a dot being initialised earlier, giving a longer time for reverse pump effects to occur, reducing the final fidelity.

of the pumping fidelities between those dots with a low and high E_T is only a small percentage difference overall.
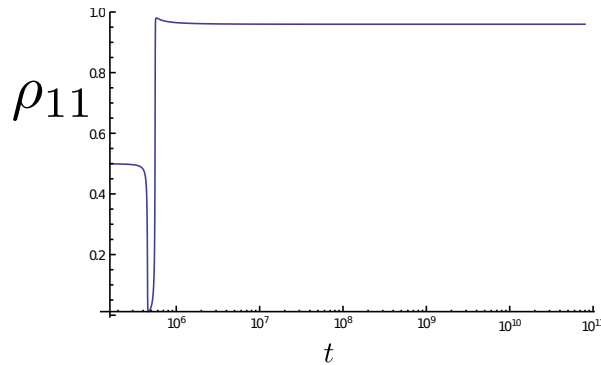
Fig. 3.7 A single dot state against logarithmic time with the same parameters as in figure 3.6 while being initialised with an especially long linear sweep of constant sweep rate 1.9×10^{-6}.

Figure 3.7 shows a single dot initialised by a particularly long sweep pulse with a logarithmic time axis. We can see that there is no visible transfer for $\Delta_E \gg (E_e + E_h)$. While the average fidelity of initialisation will be marginally better for ensembles with a smaller inhomogeneous broadening, we can see that this effect is not important in the large broadening limit, $\Delta_E \gg (E_e + E_h)$. Since our typical ensemble is within the large broadening limit, we will now go on to investigate the properties of the fidelity in this limit. All following results are taken to be that of a 15meV sweep with the dot central energy at 0.2meV unless otherwise specified. The time T taken to perform the sweep is given in each case which determines the sweep rate.

3.1.3   Optimising Initialisation

In the previous section we have shown that it is possible to initialise an ensemble of QDs using a pump with a frequency sweep that passes through resonance with all of the dots relevant states as shown for an example in figure 3.6. We now go on to calculate the optimal sweeping conditions from numerical simulations of the equations introduced in section 3.1.2.

Fit curves (red) for figure 3.8 are given by $T = \alpha \frac{1}{\Omega} + \beta \frac{1}{\Omega^2}$ where $\{\alpha, \beta\} = \{8100, 78\}$, $\{5300, 65\}$ and $\{3900, 44\}$ for a.) b.) and c.) respectively. In the large T limit the fits all tend to $T = \beta \frac{1}{\Omega^2}$. Both in-plane initialisation cases are optimal for lower Ω because of the larger reverse pumping shown in figure 3.5. The maximum fidelity for each T is given in figure 3.9 for all three cases. We can see that increasing the time T does not significantly benefit the fidelity of the initialisation beyond around $T = 5 \times 10^6$ in code units or $20\mu s$.

The above simulations are for our "typical dot ensemble" $E_e + E_h = 0.2$meV and $\Gamma = 0.004 = 1\text{ns}^{-1}$. The limits are now completely determined by these parameters, figure 3.10 shows how the fidelities are altered by modifications to these parameters. An increase in the splitting $E_e + E_h$ corresponds to an increase in the initialisation fidelity for all times T. Increasing Γ (corresponding to a lower trion lifetime) leads to a faster initialisation process, requiring less time to perform the initialisation but has a maximum fidelity which is worse than a dot with a smaller Γ, leading to a trade off between speed and fidelity.

Since the initialisation time of our typical ensemble is considerably less than the spin lifetime (10's of milliseconds) it would be optimal to choose dots with a longer lifetime or smaller Γ to increase the initialisation fidelity.

The fidelities shown in figures 3.9 and 3.10 are, for the case of large broadening and optimal Ω, given completely by Γ and $E_e + E_h$. Specifically we find that the fidelity is given completely by the ratio $\frac{\Gamma}{E_e + E_h}$. The fidelities are shown in figure 3.11.

3.1.4   Initialisation Conclusions

We have introduced a new pumping scheme suitable for initialising QDs. We have shown that there are limitations to the achievable pumping rate and fidelity for the initialisation of QDs because of the double Λ energy level structure. We introduced an initialisation scheme for use within inhomogeneously broadened ensembles with a sweeping pump pulse that initialises dots in turn as it passes through resonance.
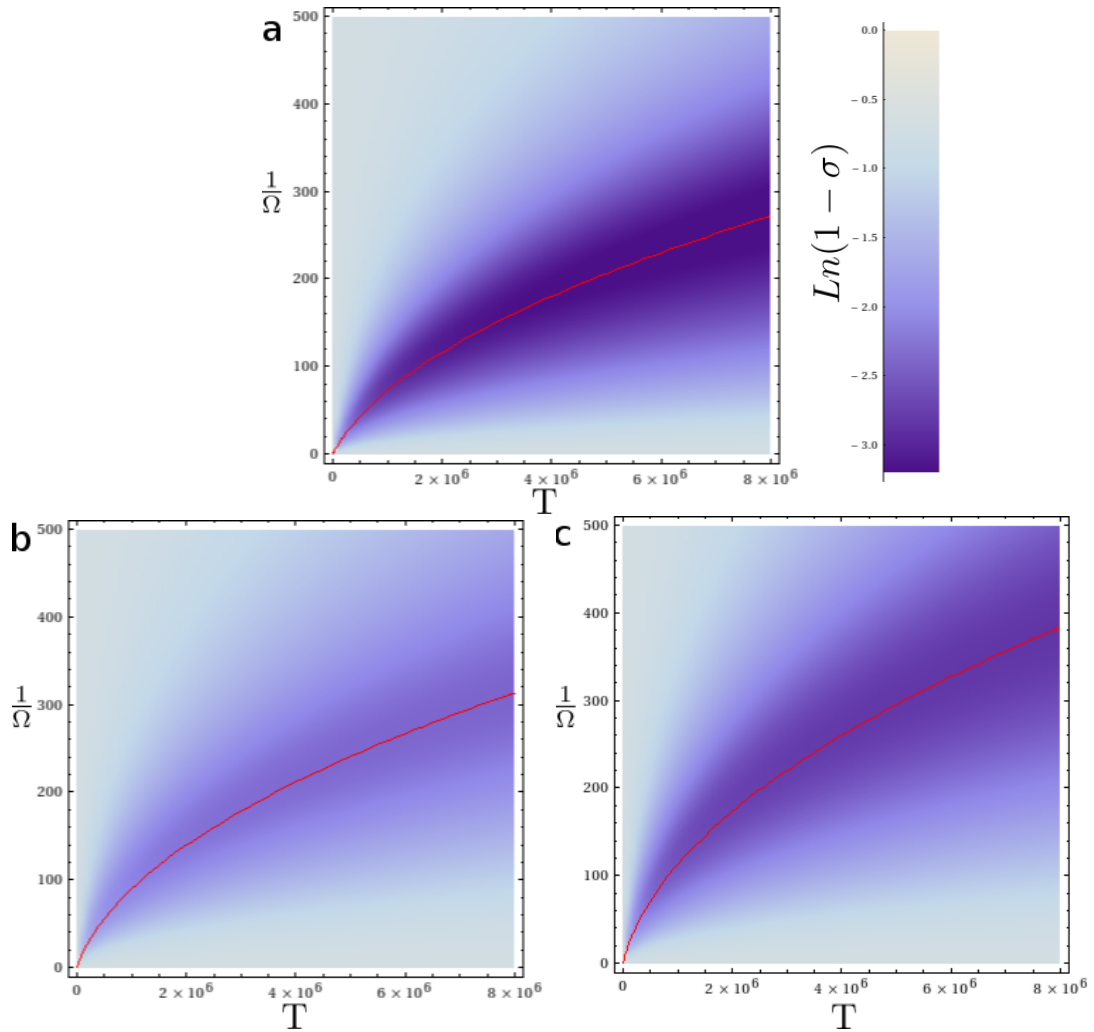
Fig. 3.8 The fidelity of pumping a single quantum dot in an ensemble with 15mev inhomogeneous broadening for a.) Vertically polarised pump b.) In-plane pump $E_e > E_h$ c.) In-plane pump $E_h > E_e$. Ω is the coupling strength and T is the total time to perform the sweep. Shading corresponds to the fidelity through $Ln(1-\sigma)$ the fit for maximum fidelity is given by the red line for each case.
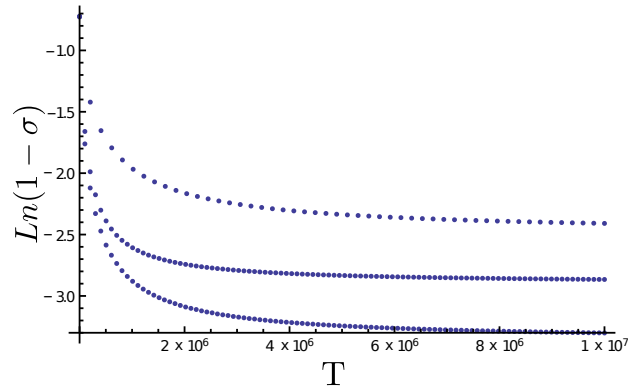
Fig. 3.9 Maximum initialisation fidelities for different sweep rates for the three cases given in figure 3.8 by red lines: Single polarisation (bottom), mixed polarisation $E_h > E_e$ (middle) and mixed polarisation $E_h < E_e$ (top). Time T is the time taken for the total time to complete the 15meV sweep, which determines the rate of sweep.
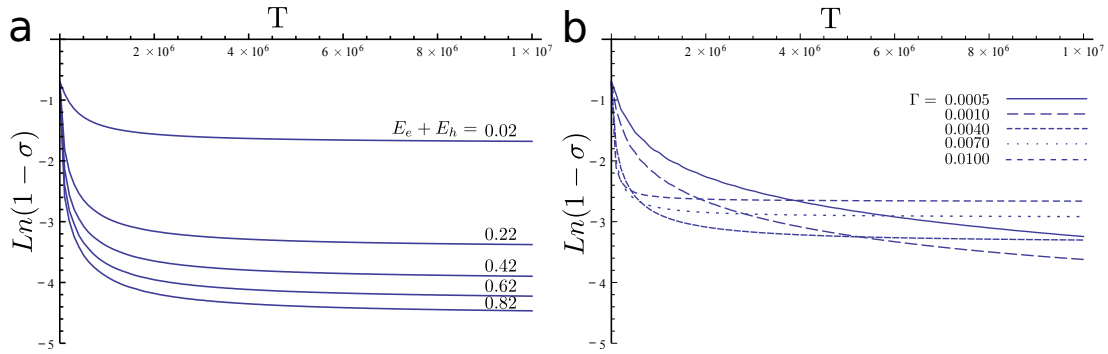
Fig. 3.10 Initialisation fidelity for a.) $\Gamma = 0.004$, varying splitting $E_e + E_h$ and b.) $E_e + E_h = 0.2$, varying decay rate Γ.
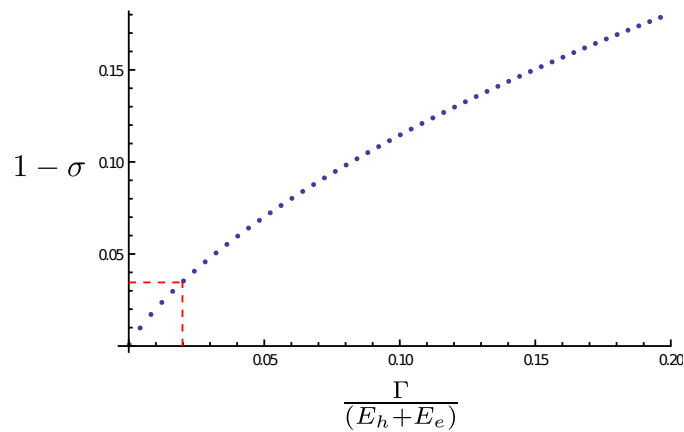
Fig. 3.11 Maximum initialisation fidelity obtainable for dots with parameters Γ and $(E_e + E_h)$. Red line indicates typical dot parameters.

We have shown that a typical QD ensemble can be initialised to a fidelity of 0.95 in a time of around 20μs, or to a maximum of 0.97 in 200μs. The maximum fidelity is only based upon Γ and the Zeeman splittings $(E_e + E_h)$. The time required to perform an optimal sweep is proportional to the inhomogeneous broadening of the ensemble and the decay rate Γ. The width of the inhomogeneous broadening of the ensemble does not affect the maximum fidelity when $\Delta_E \gg (E_e + E_h)$. A slower decay rate Γ and larger Zeeman splittings $(E_e + E_h)$ both generally lead to a better final fidelity. Within the typical parameter regime the maximum fidelity is determined entirely by $\frac{\Gamma}{E_e + E_h}$.

We have shown that if a diagonally polarised or diagonal in-plane pump is used then initialisation is still possible, but the fidelity is reduced to 0.91. For this case the fidelity is considerably better if $E_h > E_e$ (up to 0.94), but still below the fidelity possible for the horizontally polarised case (up to 0.96) which is the case we primarily investigated.

3.2   Storage

The quantum state will be stored collectively across all the dots in the system as an atomic coherence, which we refer to as a spin wave. That is to say that the phases of the electron spin in each dot in the ensemble are aligned such that they will each contribute constructively to the output mode of the photon when a control pulse is present. Knowing the state of an individual dot does not give knowledge of the existence of a spin wave. It is therefore essential that the coherence time of not only the individual dots but the full ensemble is greater than the storage time. When using ensembles of dots there will be both inhomogeneities in the local fields and in the individual dot properties to contribute to the T_2^* decoherence time. While the T_2 spin coherence time is of the order of μs [61] in single QDs and T_2^* is the measured decohenece time of the ensemble. Ensemble decoherence times of approximately T_2 are possible after a spin echo to rephase the spin to account for local, slowly varying inhomogeneities in the Overhauser field from the background nuclear spins. In an ensemble each dot's spin also needs to be in phase during readout. The T_2^* coherence time is of the order of ns with no spin rephasing techniques used [27], therefore an important part in any QD based memory will be a method to either rephase or synchronise the dot spins.

Here we will be investigating the options for spin echo to rephase the spins. However it is worth noting that there have also been promising demonstrations[35, 36] that constructively use the background nuclear spins to synchronise an ensemble of dots

to fixed precession frequencies. There are currently limits on the magnetic field that can be used B< 1T which would reduce the Zeeman splitting of the electron spin, something that generally wants to be set as large as possible.

3.2.1 π Pulses

The inhomogeneities in magnetic field generated by the background nuclear spins (the Overhauser field) leads to variations in the spin precession time in individual dots. The relative phase between the state of any two dots being given by $\phi = \Delta_\omega t$ where Δ_ω is the difference in the precession rate of the two dots. The extra phase ϕ causes the ensemble to become dephased over time. However if the population is inverted by performing a π pulse on the stored excitation the accumulated phase difference will also be inverted, and so the total accumulated phase between any two dots will become $\phi = \Delta_\omega t_2 - \Delta_\omega t_1$ where t_1 is the time before the π pulse and t_2 is the time after the π pulse, such that the spin precession times will remain the same ϕ tends to zero when $t_1 = t_2$. A second π pulse is required to return the ensemble back to its original state. Spin echo is therefore only successful if the precession rate Δ_ω has not varied significantly during the process.

We need to consider the possible methods for inverting the population. Due to the inhomogeneous broadening of the ensemble we can neglect any protocols whose rotation angle depends on the pulse area of the lasers and rather focus on protocols which employ a variation of the ARP method introduced in section 2.5.3. Spin echo can be realised with a mixture of either π or $\frac{\pi}{2}$ pulses, here we will consider the case for spin echo with only π pulses, as these can be realised to a high fidelity with an ARP transition 2.5.3. We do not believe there are any processes that would reliably perform a reliable $\frac{\pi}{2}$ rotation or any other fractional rotation on an ensemble of inhomogeneously broadened dots.

Two protocols will be discussed, both of which are usually applied to three level Λ systems, which we extend to the Voigt geometry. The protocols combine the Raman protocol and ARP by generating a two photon coupling between the ground states which is far detuned from the upper state and then sweeping this coupling through resonance with the ground states. The two we will investigate are STImulated Raman Adiabatic Passage (STIRAP) and Chirped Raman Adiabatic Passage (RCAP).

3.2.2   **STIRAP**

STIRAP is a process used in Λ systems where two monochromatic lasers are applied sequentially in a way that performs a π pulse on the ground states. This is best understood when we observe the eigenvalues of the state as the lasers are applied.
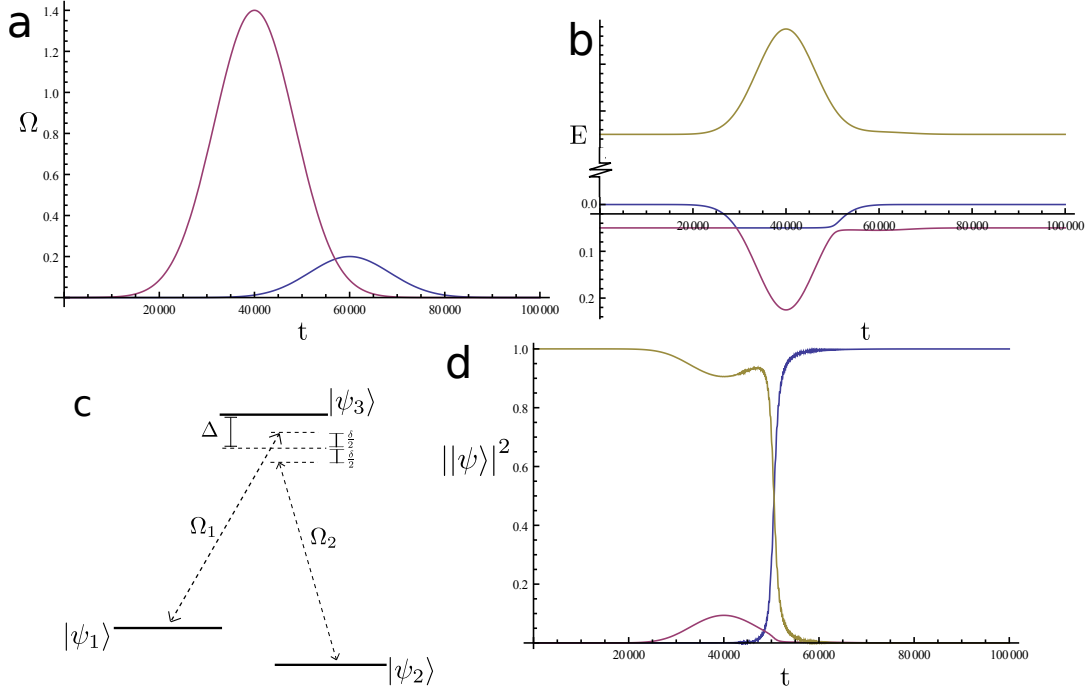
Fig. 3.12 c.) The energy level diagram of the Λ system. a.) Coupling intensity profiles of Ω_1 and Ω_2 throughout the STIRAP process. Either or both pulses can be strong and will contribute to the Rapid Adiabatic Passage process and can be applied in either order. b.) The eigenvalues in the rotating frame throughout the process. The two lower levels cross twice, but the first does not transfer a significant amount of population due the small value of Ω_2. $\delta = 0.05$, $\Delta = 2$. d.) The population transfer during the process. State mixing can be seen in the occupation of the upper level initially due to the strong coupling Ω_1. Population transfer between states 1 and 2 can be seen whilst Ω_1 is decreasing, causing an avoided crossing between the two lower levels.

Stimulated Raman Adiabatic Passage (STIRAP) [8, 14, 20, 21] in its simplest form works on a three level Λ system with one unstable state and two stable ground states. The protocol uses two monochromatic pulses to perform a π rotation on the state of the two lower levels without a significant amount of population occupying the unstable state that is coupled to the lower states and could spontaneously decay, destroying the

state. The levels are coupled via the same two photon interaction used in section 2.5.2, with the same Hamiltonian:

$$H_3 = \begin{pmatrix} -E_0/2 & 0 & \Omega_1/2 \\ 0 & E_0/2 & \Omega_2/2 \\ \Omega_1/2 & \Omega_2/2 & \Delta \end{pmatrix} \tag{3.5}$$

The STIRAP protocol creates an ARP level crossing via the Stark shift of a strong laser. One strong laser pulse and one weak pulse are applied to the system, partially overlapping (figure 3.12a). The strong pulse creates a Stark shift causing the ground state eigenvalues to cross twice. During the first crossing the weaker pulse is not applied and therefore there is no two-photon coupling and the crossing does not transfer population. But for the second crossing, because of the partial overlapping of the two pulses the crossing has the two-photon Raman coupling. This creates an avoided crossing between the lower levels (figure 3.12b) which transfers population using adiabatic rapid passage, introduced in section 2.5.3. If performed in the limit equation (2.25) tends to 1, the crossing results in one complete π rotation on the state of the lower levels.

The Hamiltonian (3.5) can be reduced to the following effective Hamiltonian through adiabatic elimination:

$$H_{\text{eff}} = \frac{1}{4} \begin{pmatrix} -2\delta + \frac{\Omega_1{}^2}{\Delta} & \frac{1}{\Delta}\Omega_1\Omega_2 \\ \frac{1}{\Delta}\Omega_1\Omega_2 & 2\delta + \frac{\Omega_2{}^2}{\Delta 4} \end{pmatrix} \tag{3.6}$$

This gives the strength of the coupling between the lower levels $\Omega_{\text{eff}} = \frac{\Omega_1\Omega_2}{2\Delta}$ and the detuning of the coupling from the lower levels $\Delta_{\text{eff}} = \delta + \frac{\Omega_1{}^2 - \Omega_2{}^2}{4\Delta}$ where $\delta = E_0 - (\omega_1 - \omega_2)$ is the bare two-photon detuning. The detuning Δ_{eff} is dependent on the strength of the two couplings, specifically we can see that if $\delta > 0$, Ω_1 is small then an increase in Ω_2 will cause the value of the detuning to change sign. When performed in the adiabatic limit this change of sign will cause an ARP population transfer. There are also some extensions to higher level systems [8] [57].

3.2.3 STIRAP in the Voigt geometry

We have shown how STIRAP works in the three level Λ system in 3.2.2, we want to see how the protocol implementation changes for the Voigt geometry in QDs, first introduced in figure 1.4. We shall see that the STIRAP protocol no longer works on our four level system. The Voigt geometry effectively contains two Λ couplings

$1 \to 3 \to 2$ and $1 \to 4 \to 2$ which are resonant under different conditions and have opposite selection rules. The effects of the second pair of couplings has two relevant effects that we need to take into account. Firstly there is a new resonance condition that should be avoided as it may cause unwanted population transfer both coherently and incoherently. Secondly there will be modifications to the Stark shifts induced by the couplings since now both lasers will couple to all four levels.

$$H_4 = \begin{pmatrix} -E_0/2 & 0 & \Omega_1/2e^{(-i\omega_1 t)} & \Omega_2/2e^{(-i\omega_2 t)} \\ 0 & E_0/2 & \Omega_2/2e^{(-i\omega_2 t)} & \Omega_1/2e^{(-i\omega_1 t)} \\ \Omega_1/2e^{(i\omega_1 t)} & \Omega_2/2e^{(i\omega_2 t)} & E_x + E_h/2 & 0 \\ \Omega_2/2e^{(i\omega_2 t)} & \Omega_1/2e^{(i\omega_1 t)} & 0 & E_x - E_h/2 \end{pmatrix} \tag{3.7}$$

The four level Hamiltonian equation that describes a charged QD in the Voigt geometry (equation (3.7)) can again be reduced to a two level effective Hamiltonian using adiabatic elimination when we are only interested in the dynamics of the two ground states:

$$H_{\text{eff}} = \begin{pmatrix} -\Delta_{\text{eff}}/2 & \Omega_{\text{eff}}/2(1 + e^{-i(\omega_1 - \omega_2)t}) \\ \Omega_{\text{eff}}/2(1 + e^{i(\omega_1 - \omega_2)t}) & \Delta_{\text{eff}}/2 \end{pmatrix} \tag{3.8}$$

Ignoring the quickly rotating coupling term we find that the Hamiltonian can be written as:

$$H_{\text{eff}} = \frac{1}{4} \begin{pmatrix} -2\delta + \frac{\Omega_1{}^2}{\Delta} + \frac{\Omega_2{}^2}{\Delta_4} & \frac{1}{\Delta}\Omega_1\Omega_2 \\ \frac{1}{\Delta}\Omega_1\Omega_2 & 2\delta + \frac{\Omega_2{}^2}{\Delta} + \frac{\Omega_1{}^2}{\Delta_4} \end{pmatrix} \tag{3.9}$$

This can be compared to the effective Hamiltonian for the Λ system from equation (3.6). We know that the protocol in the three level case creates an avoided crossing by using the Stark shift cause by the strong couplings to modify the energy levels of the lower states, altering the sign of $\Delta_{\text{eff}} = \delta + \Omega_1^2 \frac{1}{4\Delta} - \Omega_2^2 \frac{1}{4\Delta}$. But if we investigate the Voigt geometry's two level effective Hamiltonian we can see there are now two new terms which mostly cancel out the relative shift which was present for the Λ system. $\Delta_{\text{eff}} = \delta + \Omega_1^2 \left(\frac{1}{4\Delta} - \frac{1}{4\Delta_4}\right) + \Omega_2^2 \left(\frac{1}{4\Delta_4} - \frac{1}{4\Delta}\right)$. Since Δ and Δ_4 are also approximately equal (assuming $E_e, E_h \ll \Delta$) then these extra effects will almost completely eliminate the change in the relative Stark shift between the ground states. This means a large increase in either of the Ω's will not have a significant effect on the relative energy shift between the two levels and will not be able to cause the required sign change in Δ_{eff}. This has been confirmed through simulations shown in figure 3.13.
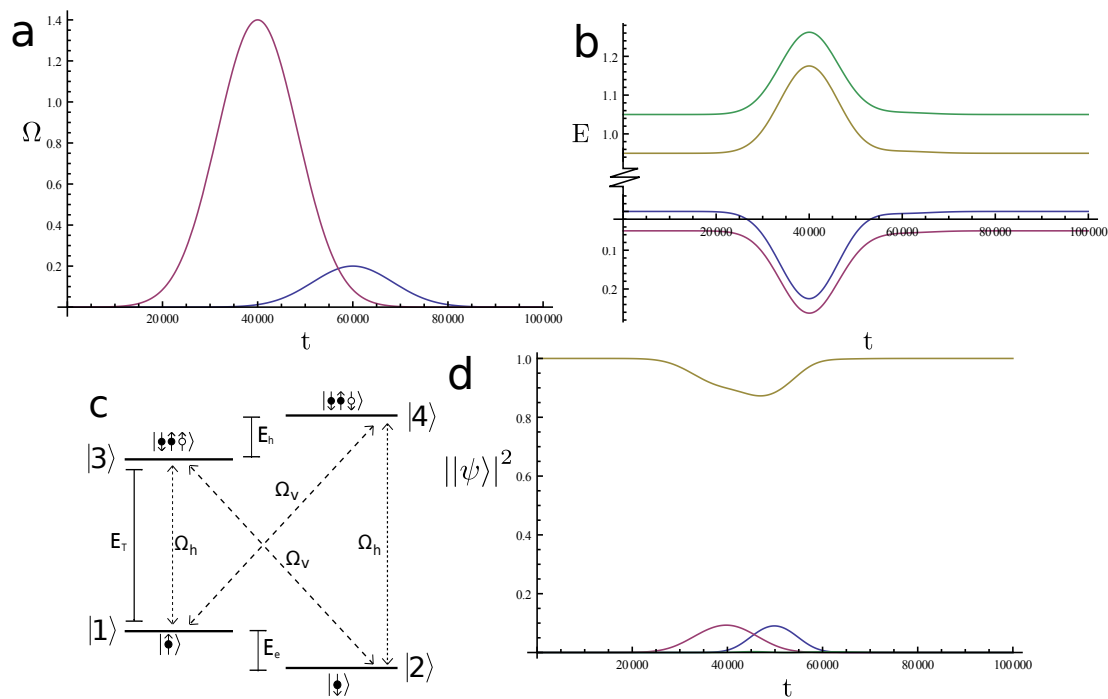
Fig. 3.13 The STIRAP protocol in the Voigt geometry (c). The coupling strength profiles, identical and with the same parameters shown in figure 3.12. b.) The eigenvalues for the attempted transition, both lower levels are now shifted almost equally as both lower levels are now coupled to the upper levels via the strong laser. This prevents the level crossings that are required for the STIRAP process. d.) This results in the population only temporarily being transferred into the other states through state mixing but without no overall transfer we saw in the Λ system.

If Δ was chosen to be of a similar order to the upper and lower levels' energy splitting E_h and E_e then it may be possible to still induce a significant avoided crossing from only modifying the magnitude of the laser couplings. In this limit we are modifying the frequencies to amplify the difference between the detunings Δ and Δ_4 to the point we can neglect the effects of the fourth level and revive the Λ system dynamics. This method would require careful tuning of the lasers close to resonance with the dots and so we would no longer be able to address a large ensemble of inhomogeneously broadened QD's simultaneously.

STIRAP is therefore not a suitable protocol for performing π pulses in an ensemble of QDs, for either in-plane geometry or the out-of-plane Voigt geometry, we will now go on to introduce an alternative method.

3.2.4   RCAP

Raman Chirped Adiabatic Passage (RCAP) was presented as an alternative to STIRAP [17] [18]. RCAP uses the same Λ type systems from figure 2.2 and also uses an avoided crossing to transfer the population robustly. The main difference from STIRAP is that RCAP generates the avoided crossing by chirping one of the lasers rather than through a Stark shift induced by the lasers.

The lasers are setup in a Raman configuration where the lower levels are both detuned from the upper energy level and close to two photon resonance between each other as for stimulated Raman transfer in section 2.5.2 and STIRAP in section 3.2.2. For RCAP the crucial avoided crossing is induced between the lower two levels by a chirped laser that sweeps through two photon resonance. Either laser can be swept in either direction for successful population transfer. The pulses do not in general need to be the same intensity, but have been set to in figure 3.14 to avoid Stark shifts from altering the resonance condition.

If we inspect the effective Hamiltonian (2.15) then we can see that there is an adiabatic increase and decrease in the off diagonal elements (the coupling intensity) and a sweeping coupling frequency which induces an avoided crossing between the two states which causes the population transfer. This shows that RCAP can be considered to be identical to an ARP transition when looked at from the perspective of two level effective Hamiltonian. The transition probabilities can therefore also be derived from the effective Hamiltonian (2.15), assuming the original conditions for adiabatic elimination hold. Equation (2.25) can be used to calculate the transition probability
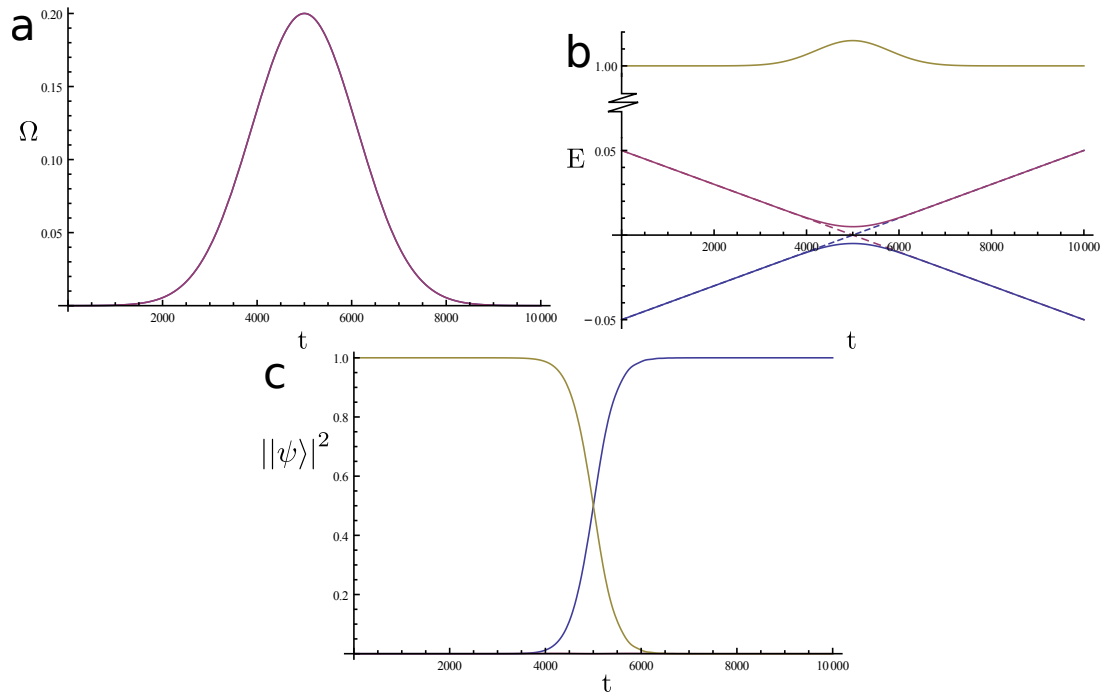
Fig. 3.14 The dynamics of a RCAP transition, performed in a three level Λ system from figure 2.2 without the inclusion of spontaneous decay a.) The intensity of the couplings during the transition, in this case both are of identical strength, but in general they can be of different strengths b.) The eigenvalues of the Hamiltonian in the rotating frame. $\Delta = 1$, $\frac{dE}{dt} = 0.001$ The two lower energy levels undergo an avoided crossing as in figure 2.7b, the upper level is Stark shifted slightly, but otherwise remains detuned throughout the process c.) The population transferred throughout the transition. There is a near complete transfer from level $|\psi_1\rangle$ to $|\psi_2\rangle$ and a small amount of population transferred to the upper level through state mixing during the middle of the transition, although hard to see here.

substituting $\Delta \rightarrow \Delta_{\text{eff}}$ and $\Omega \rightarrow \Omega_{\text{eff}}$. we can see that the fidelity of the transfer should be given by:

$$\sigma = 1 - e^{-\left(\frac{\Omega^2}{2\Delta}\right)^2 \frac{1}{\frac{dE}{dt}} \frac{\pi}{2}} \tag{3.10}$$

We first cover the three level Λ system case to later compare to the Voigt geometry case. Spontaneous emission is the cause of the loss of fidelity in figure 3.15b and occurs due to state mixing raising a proportion of the population into the upper state. State mixing, introduced in section 2.5.1 is when, due to the Ω coupling, the eigenvectors of the system become a mixture of the original bare states. Since the protocol is performed adiabatically, the state remains in an eigenstate throughout the whole process, and because this eigenstate contains a proportion of the bare state $|3\rangle$ it is capable of spontaneously emitting a photon, decohering the state. State mixing will always occur but will be small if Ω is small. The state mixing populations in a two level system are given by equation (2.21).
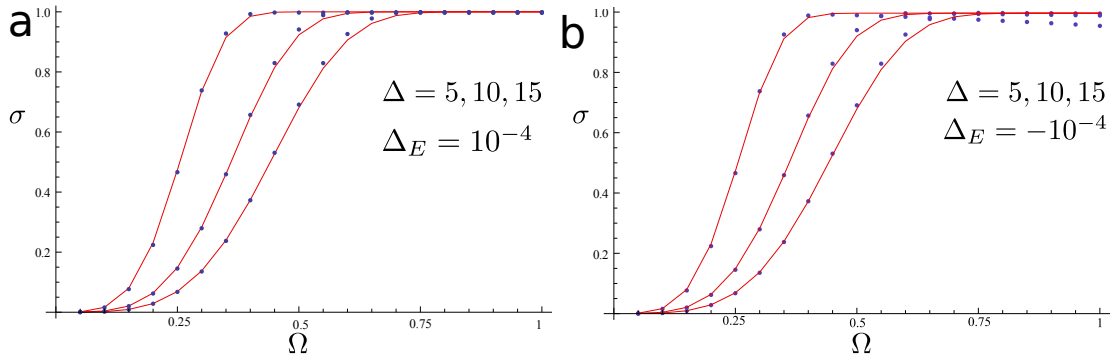
Fig. 3.15 A set of example fits for RCAP in a three level Λ system with spontaneous decay with $\Delta_E = \pm 10^{-4}, \Delta = 5, 10, 15$. Fits from equation (3.10) are given as the red line, results from numerical simulations with the inclusion of spontaneous emission are given as blue points, $\Gamma = 0.04$. A smaller Δ case corresponds to a smaller Ω required for transfer. A comparison between the two graphs shows that there is an asymmetry in Δ_E, the sweep rate of the chirp, for higher values of Ω.

$$\rho_{33} = \frac{1}{2} - \frac{\Delta}{2\sqrt{\Delta^2 + \Omega^2}} \tag{3.11}$$

There are two contributions to the population in the upper state $|3\rangle$, one from state mixing with each of the lower states $|1\rangle$ and $|2\rangle$. Whether these contributions would be constructive or destructive depends on the phase of the mixed populations. The difference between the two plots in figure 3.15 is due to either destructive or

constructive interference respectively for the state $|3\rangle$ population. The fits do not include the effects of spontaneous emission equation (3.10) and demonstrate the effects of spontaneous emission to the final fidelity. The upper state populations for two example simulations are given in figure 3.16, showing the cases for nearly complete constructive, and destructive interference. An alternative view on this asymmetry is to notice that, of the two ground states in the dressed state picture, one will have a higher energy and one lower. If the bulk of the population is in the ground state that has the higher energy (closest to the excited energy) it will have the maximum level of mixing while if the bulk of the population is in the lower state then there will be a minimal amount of state mixing.
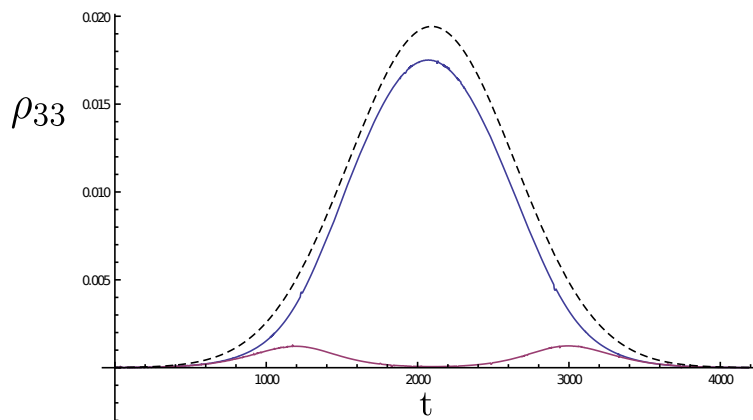
Fig. 3.16 The population of the excited state $|3\rangle$ throughout the RCAP process. The two lines show close to complete constructive/destructive interference and are for Δ_E is positive/negative respectively, or for the initial population in state $|1\rangle/|2\rangle$ respectively. Switching either of these parameters will change the behaviour of population in the upper level. The dotted fit gives the maximum population if the contributions are completely constructive and the population is split evenly between the two ground states. In both cases $\Omega = 1$, $\Delta = 5$.

In general population in the upper state $|3\rangle$, which determines the amount of spontaneous emission, will depend on both the initial state and the direction of the sweep for the Λ system. This leaves the amount of spontaneous emission complicated to predict exactly, but leaves a maximum value which can be easily determined from equation (3.11). The total population transferred throughout the process via spontaneous decay is given by the integral of the total population in the unstable state during the transfer:

$$2\Gamma \int dt \left(\frac{1}{2} - \frac{\Delta}{2\sqrt{\Delta^2 + \Omega^2}} \right) \tag{3.12}$$

3.2.5   RCAP in the Voigt geometry

To identify the effects of the fourth level on the RCAP transition we again consider the two level effective Hamiltonian for the Voigt geometry (2.17) which has two diagonal terms, one of which is identical to the Λ case and one which is rotating. We assume that the rotating term can be ignored as we did for the rotating wave approximation.

Since RCAP induces an adiabatic crossing by sweeping the frequencies (changing ω) of the lasers rather than relying on the induced Stark shift (changing Ω), it should be expected to perform similarly in both the three level Λ system and four level Voigt geometry, since the detuned $1 \rightarrow 4 \rightarrow 2$ transition will be detuned and should not significantly affect the dynamics of the transition. We compare simulation results for the three and four level transition probability in figure 3.16.
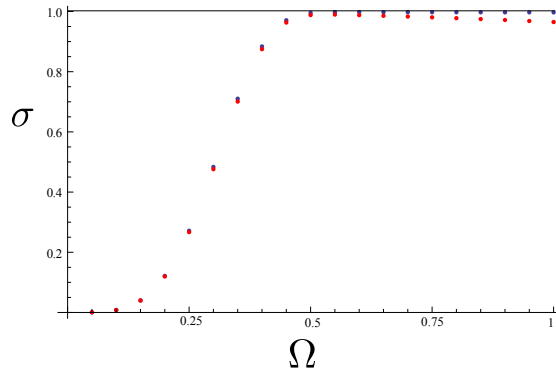
Fig. 3.17 Comparing the 3 level Λ system fidelities with the 4 level Voigt geometry fidelities. $\Delta = 1$, $\Delta_E = 0.5 \times 10^{-4}$. The four level case has a poorer fidelity due to the spontaneous emission from the fourth level.

The second effect of the fourth level is to alter the effective detuning, which is slightly beneficial as we can see from the same arguments as presented in section 3.4. The fourth level means that it is possible to use different strength Ω's without having to worry about readjusting the resonance conditions to account for the Stark shift. Here have set $\Omega_h = \Omega_v$.

We can see from figures 3.17 and 3.15 that the four level RCAP transfer probability obeys the same Landau-Zener condition (equation (3.10)) as the three-level Λ system, with an added loss of fidelity which we will see is due to spontaneous emission.

The population transfer via spontaneous emission does differ for large Ω between the 3 and 4 level systems. The total population in the upper state levels $|3\rangle$ and $|4\rangle$ through state mixing would naively be more than the population for the upper state for the Λ system, if only because there are now two levels to decay from. We find that this is generally true, however the state mixing induced population in the upper levels

Fig. 3.18 The upper state populations ρ_{33} and ρ_{44} for different initial conditions and sweeping conditions. Each plot shows the population for a po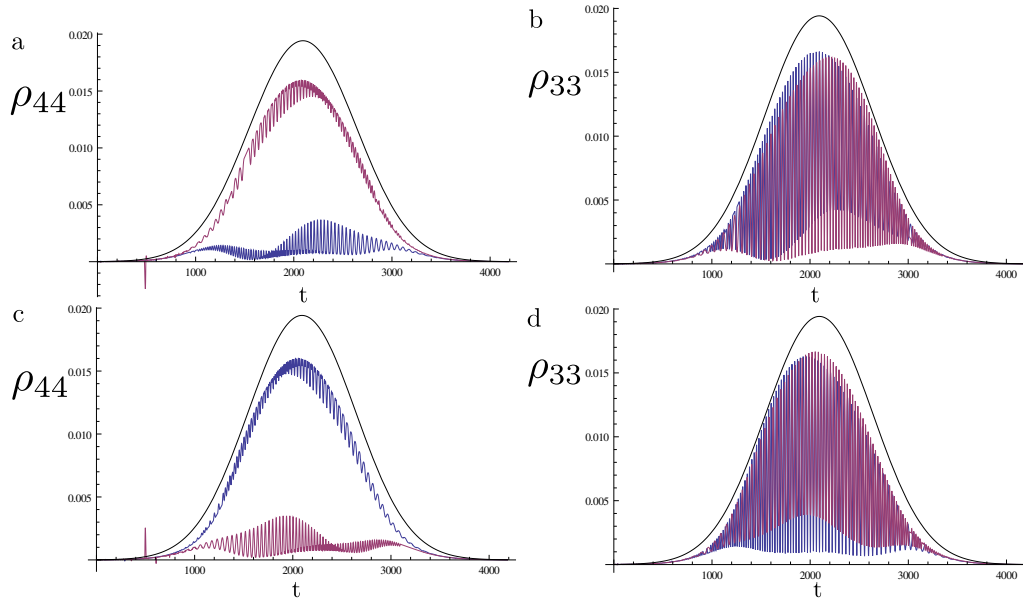sitive and negative sweep. a.) and b.) correspond to the population starting in state ρ_{11}, c.) and d.) correspond to starting in state ρ_{22}. For all cases the populations of state ρ_{33} oscillate between maximum and minimum values, which are bounded by 2 times equation (3.11), the doubling is due to constructive interference. The state ρ_{44} population varies depending on the initial condition and sweep direction, as we also saw in figure 3.16, and is also bounded by 2 times equation (3.11).

3 and 4 is similarly dependent on the initial state and sweeping direction as for the Λ case. The populations are shown in figure 3.18. One of the levels $|3\rangle$ oscillates between the maximum and minimum values shown in figure 3.16, whilst the level $|4\rangle$ population has similar dependence to the Λ case. If the level which holds the most population at the start of the simulation has the higher energy in the rotating frame, state $|4\rangle$ will contain a larger population throughout the process. This results in a contribution between 0.5 and 1.5 times the maximum Λ decay rate, given by equation (3.12), which can be controllable if the initial state is in a known ground state.

From equations (3.10) and (3.12) we can derive the total population transfer with the RCAP protocol.

$$\sigma = 1 - e^{-\frac{\left(\frac{\Omega^2}{2\Delta}\right)^2}{\Delta_E}\frac{\pi}{2}} - 2a\Gamma \int dt \left(\frac{1}{2} - \frac{\Delta}{2\sqrt{\Delta^2 + \Omega^2}} \right) \tag{3.13}$$

Where a depends on the initial conditions and sweep direction, and varies between 0.5 and 1.5 depending on the sweep direction and initial conditions.
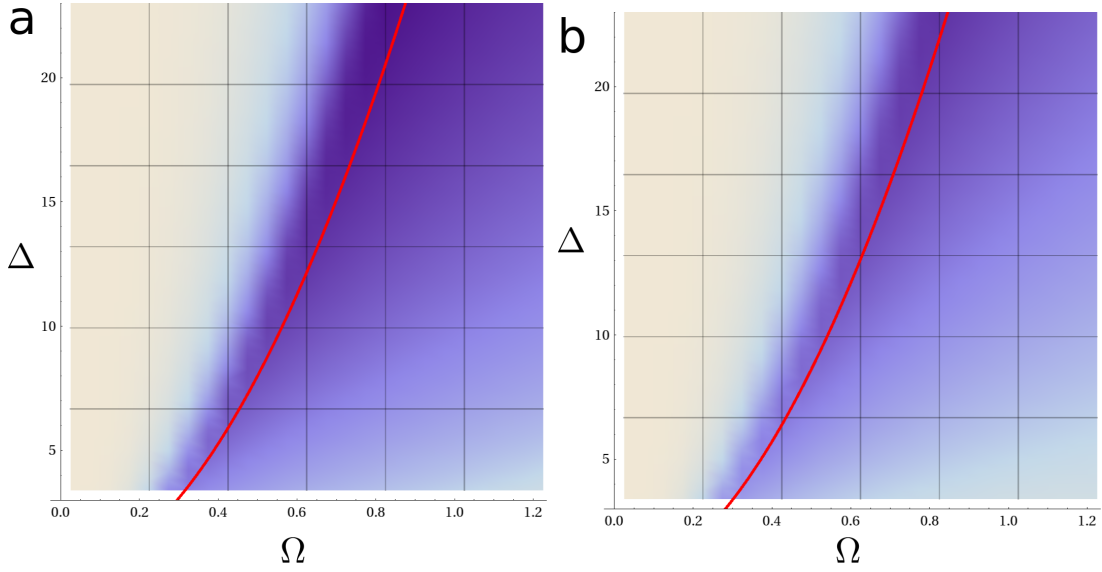
Fig. 3.19 RCAP sweep fidelities for a.) positive sweep, which shows low spontaneous emission losses b.) negative sweep which shows high spontaneous emission losses. The red curve shows the optimal Ω dependence on Δ for maximum fidelity in both cases. The colour function is fitted to a log scale from -6 to 0. Simulations used a Ω Gaussian function with a FWHM of 1800 in code units and a sweep rate of 4.8×10^{-5}.

We can see from figures 3.19 and 3.20 that the system behaviour when performing a positive or negative sweep is qualitatively similar, but the positive frequency sweep offers an overall higher fidelity of transfer. An RCAP transition performed on an ensemble of dots would have a spread of Δ's equal to the the inhomogeneous broadening, 10meV for our typical ensemble. We can see from figure 3.20 that to perform an RCAP transition with a fidelity $Ln(1-\sigma) < 5$ (a 1% loss) simultaneously on every dot in the ensemble would require a pulse detuned by at least 15meV from the closest dot for a positive sweep with $\Omega \approx 0.8$ or 25meV from the closest dot for a negative sweep with $\Omega \approx 1.0$. The value of Ω used is also less critical for larger detunings.

The spontaneous emission is dependent on the pulse width of the lasers, while the fidelity of the RCAP transition is only dependent on the strength of the coupling around the crossing, and the assumption that the system changes adiabatically. If the pulse is too short and the process is not completely adiabatic the Rabi oscillations begin to appear [51] while a longer laser pulse increases the spontaneous emission during the process, which should be minimised. The previous RCAP examples in this section (3.2.4) all use an identical Gaussian FWHM for each Ω pulse which was chosen to be 1800 in code units. Now we consider the cases for different transition
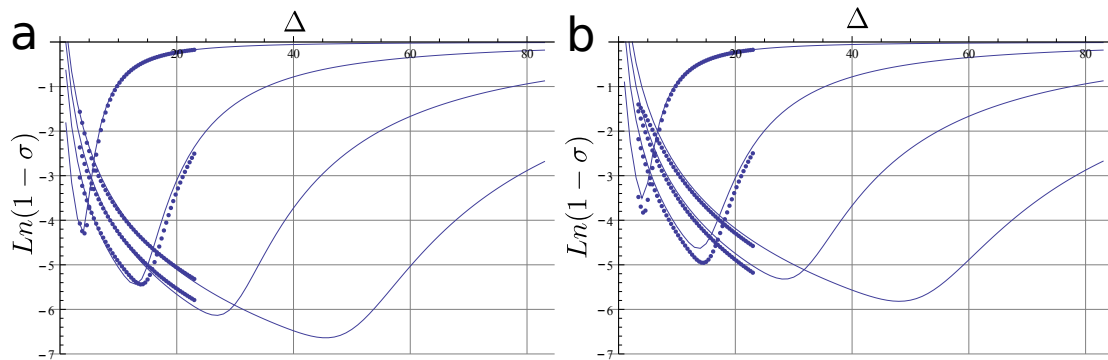
Fig. 3.20 The fidelity of the RCAP protocol for an identical Ω pulse on dots with varying Δ (in meV), for example inhomogeneously broadened dots. The Ω's used are $\{0.325, 0.625, 0.925, 1.225\}$, a.) and b.) show transfers with a positive and negative sweep respectively. Data points taken from numerical simulations in figure 3.19, fit given by equation (3.13).

times changing the FWHM of the Ω pulse to identify the range of the FWHM that will create a successful RCAP transition.

In figure 3.21 we consider the effects of modifying the pulse width in the numerical simulations, showing how the width of the laser pulses influences the fidelity of the transition. All simulations run for 3.21a are run with parameters that would be expected to have a 99% fidelity according to the Landau-Zener fidelity in equation (3.10) which does not account for spontaneous emission or the lack of adiabadicity due to the length of the Gaussian pulse, Δ_E is modified with Ω to ensure this fidelity. Figure 3.21b was run for identical Δ_E to a, but for double Ω, which should result in a fidelity beyond the numerical accuracy of the simulations. We can isolate losses due to three other effects in the simulation as a reduction from 99% in a, or ≈ 1 in b. The simulations were run with a linear frequency sweep. For larger pulse widths the frequency sweep exceeded double the ground splitting energy E_e and therefore induced a second RCAP transition from $|1\rangle \rightarrow |4\rangle \rightarrow |2\rangle$, leading to a sharp loss of fidelity for larger t shown in the figure. This is a fidelity loss mechanism that does not exist in the original Λ system and further constrains the parameters which can be used. Smaller pulse widths broke the adiabatic condition, and therefore the state underwent Rabi oscillations rather than adiabatically following the path of the eigenstates. This is particularly visible for the cases in 3.21b where the larger Ω corresponds to a larger pulse area, creating several distinct oscillations. For 3.21a the pulse area for smaller t was not large enough for multiple oscillations and can be simply seen as a complete lack of transfer. For each set of parameters there is a useful area of parameter space which is the flat shelf between the two significant losses of fidelity at each end.
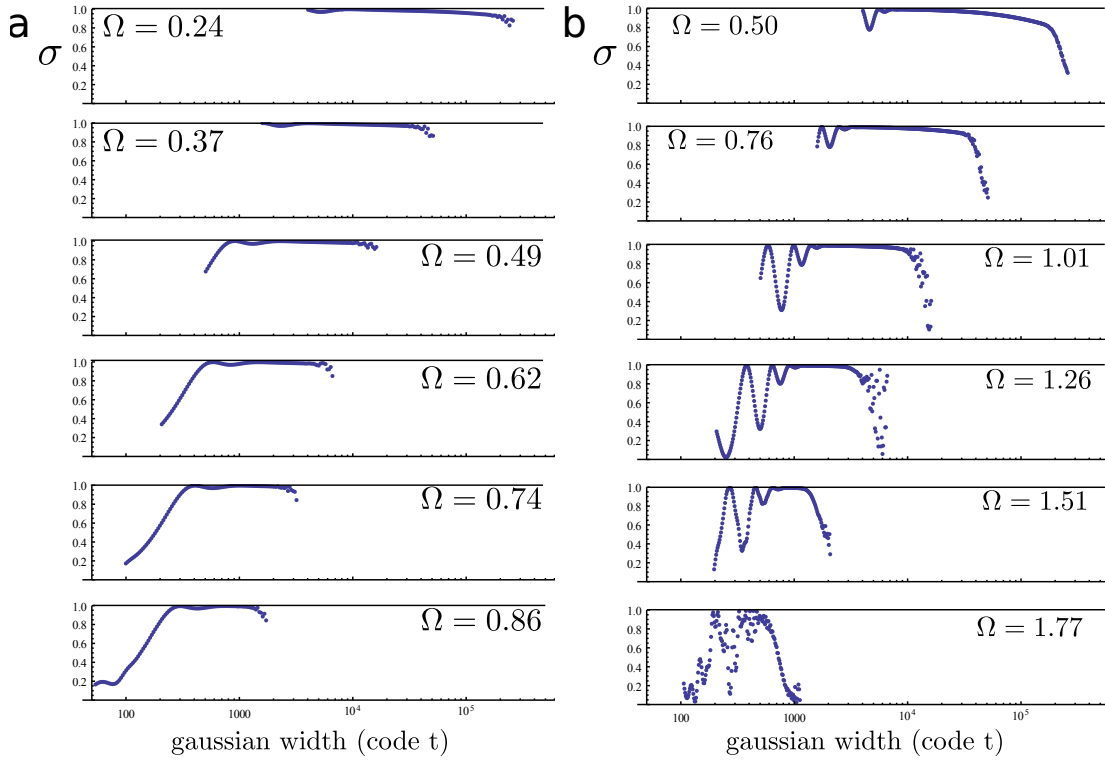
Fig. 3.21 Plots for the total fidelity of an RCAP pulse for varying pulse widths. a.) All simulation parameters set such that the Landau-Zener fidelity in equation (3.10) is fixed to $\sigma = 0.99$. $\Delta = 10$ for all cases, setting Ω sets the rate of sweep. b.) Ω is doubled to 2Ω with the rate of sweep identical to a.), such that the Landau-Zener fidelity in equation (3.10), $\sigma \approx 1$, beyond the numerical accuracy of the simulations. b.) shows clearly the Rabi oscillations that are barely visible in a. for low widths.

Spontaneous emission can be seen in 3.21a for the largest Ω's and largest Gaussian widths, however in figure 3.21b the spontaneous emission clearly creates a significant dip for larger pulse areas, for a more complete analysis of the spontaneous emission see figure 3.20. While using a larger Ω generally allows for shorter pulse, and therefore a shorter gate time, for the largest Ω sweep in 3.21b we can also see that the usable area of parameter space has vanished since the condition for the lack of adiabadicity at small t now overlaps with the condition of the total sweep frequency being less than E_e. There are therefore no advantages at any point of parameter space in trying to use an Ω which would optimise the Landau-Zener condition significantly beyond the desired fidelity of the transition.

The smallest possible $FWHM$ for the highest Ω in figure 3.21a is roughly 700 in code time, this translates to $700 \times 1000 \times \frac{\hbar}{1.6\times10^{19}} = 4.6 \times 10^{-10} = 46$ ns in real time.

3.2.6 π Rotation Conclusions

We showed that the STIRAP protocol cannot be used in the Voigt geometry but that RCAP protocol instead is a suitable protocol for performing π pulses in QDs.

We have found that the Landau-Zener formula with losses from spontaneous emission included fits the results well, given by equation (3.13). The ideal parameters are approximately ones which result in the fidelity of the ARP transition being equal to $1-$ the spontaneously emitted population. We have shown that there is an initial state and sweep direction dependence on the fidelity losses due to spontaneous emission for the RCAP protocol, because this determines whether the contributions to the population level in the unstable upper state are constructive or destructive.

We have shown that when the lasers are further detuned from resonance the transition is less sensitive to relative detuning between each dot in figure 3.20. The amount of inhomogeneous broadening therefore defines how far the laser pulses need to be detuned from resonance (Δ), but does not provide a strict limit on the fidelity of the rotation achievable for a given amount of inhomogeneous broadening.

We have shown there are two limits to the length of the pulses that can be used. The pulses must be long enough that the whole process is adiabatic whilst being short enough that the frequency sweep does not overlap with the resonant frequency of the second Λ system in the Voigt geometry. We have demonstrated that these limits do not overlap for a wide area of parameter space, as shown in figure 3.21 which allows for a large variation in the parameters used for the RCAP transition. This is necessary for the protocol to be used on ensembles containing dots with varying parameter values.

Since the fidelity σ of the RCAP transition is mostly governed by the Landau-Zener formula the maximum fidelities achievable are only limited by the time within which the transitions is performed.

We have shown in figure 3.20 simulations in which a fidelity of 0.997 is achieved across an ensemble with 10mev inhomogeneous broadening for a pulse with a FWHM of 120ns. A single dot state can be flipped with a pulse FWHM of 46ns to a fidelity of 0.99 shown in figure 3.21.

3.3 Wave Mixing Losses

There is one more contribution to a loss of fidelity of the RCAP process which we will discuss. We do not include this loss in the conclusions of this chapter because the process is unlikely to be relevant to any actual implementation of the RCAP process. It is however an interesting physical phenomenon that is valid in other models and

will be the topic of the next chapter of this thesis. The process relies on $\Omega \gtrsim \Delta$. This parameter regime would also introduce a significant amount of spontaneous emission in a real QD system, however spontaneous emission has been removed from the model for this section to isolate the behaviour of the Wave Mixing transfer.
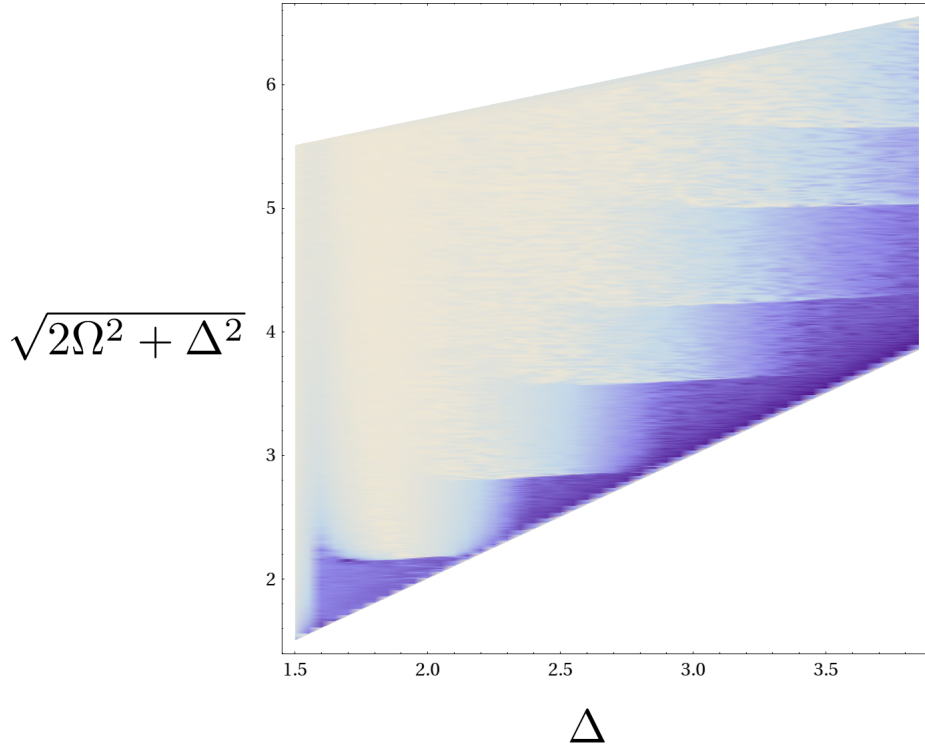
Fig. 3.22 An extension to figure 3.19, showing RCAP fidelity for lower Δ and larger Ω. Darker areas correspond to higher fidelity, lighter to poorer fidelity, the y axis was chosen empirically to emphasis the steps. The gaps between the steps are approximately the ground state splitting energy E_e. The parameter E_h was set to zero for these simulations to isolate the effect.

While numerically investigating the parameter space close to resonance with the dots a curious loss of fidelity was noticed at specific values of Ω and Δ, particularly when Δ was small and Ω was large, this was for larger Ω's than necessary for the RCAP protocol to be successful. An example result for this is shown in figure 3.22 which is the an extension of the parameter space covered in figure 3.19. The simulations covered in this figure do not include the effects of spontaneous emission and yet still yield very poor fidelities for large values of Ω which was not expected, within the parameter regime of figure 3.22 virtually all of the plot should be expected to be dark, with a fidelity beyond the numerical accuracy of the simulations and with a thin lighter line at small Ω. This loss in fidelity indicated a different mechanism that

was not yet accounted for conceptually in the model. The fidelity loss occurred with characteristic sharp steps shown in figure 3.19 and shows a highly non-linear effect with a large change in the behaviour of the system with only a small increase in Ω. The factor $(2\Omega^2 + \Delta^2)^{\frac{1}{2}}$ was determined empirically as the factor which approximately determined the critical value of Ω, and is noted to be approximately the Stark shift caused by the two applied lasers which guided us to the solution. We also noted that the steps were separated by an energy equal to the energy difference between the two lasers applied which is also the ground state energy level splitting. The effect does not occur for the same parameters in the Λ system and is therefore directly due to the inclusion of the fourth level in the Voigt geometry. We have discovered that these steps are due to high orders of wavemixing due to the interaction of the two external lasers with the dot, creating extra resonance conditions that would otherwise be absent in the system. These new resonances interact in a Stark Chirped Rapid Adiabatic Passage (SCRAP) interaction that is described in section 4.1. The full analysis of the mechanism including the generation of the different resonance conditions is given in chapter 4.

Here we briefly include a model considering the consequences of wavemixing within the RCAP protocol we were discussing above. If we assume that the only function of the fourth level is to generate wave mixing resonances, we can treat the system as a single Λ system, generating RCAP transfer plus a single extra wavemixing coupling with a frequency determined through wavemixing. This results in the Hamiltonian:

$$H_{\Lambda+WM} = \begin{pmatrix} -\delta/2 & 0 & \Omega_1/2 & 0 \\ 0 & \delta/2 & \Omega_2/2 & \Omega_{\text{WM}}/2 \\ \Omega_1/2 & \Omega_2/2 & \Delta & 0 \\ 0 & \Omega_{\text{WM}}/2 & 0 & -\Delta_{\text{WM}} \end{pmatrix} \tag{3.14}$$

Figure 3.23a gives the eigenvalues for this Hamiltonian when the parameters are set for the standard Λ RCAP transition with a large Ω. The fourth level is coupled via a wave mixing resonance to level two, this coupling undergoes two weakly avoided crossings with level two due to the Stark shift of the applied RCAP lasers. Each crossing will transfer population, destroying the fidelity of the protocol. Figure 3.23b shows the population during a numerical simulation run with the four level RCAP parameters and clearly shows two crossings between level two and level four behind the desired $2 \rightarrow 1$ transfer, as we would expect from the model in equation (3.14).
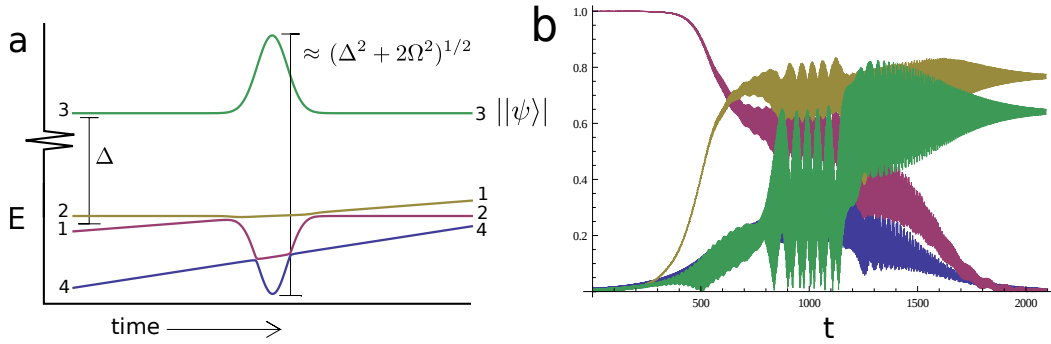
Fig. 3.23 RCAP with the inclusion of wavemixing, see figure 3.14 for RCAP transfer without wavemixing. a.) Eigenvalue diagram for an RCAP pulse coupled with a wave mixing resonance coupling to the fourth level, showing eigenvalue energy E against time. This plot gives a qualitative picture. b.) An example of a the population during 4-level RCAP transfer from a simulation with poor fidelity in figure 3.22 with $\Omega_{\max} = 1.25$, $\Delta = 2.4$ and $\frac{dE}{dt} = 4 \times 10^{-5}$.

In general there will can be many transfers throughout the process, from either of the lower levels into either of the upper levels. Figure 3.23b was chosen to show a clean example with only one pair of crossings to present the concept.

From the wave mixing theory which we introduce in the next chapter we should expect an infinite ladder of resonances spaced at energies of $2E_e$. We can see the ladder from the steps in figure 3.22. However, the actual spacing for the resonances in figure 3.22 is E_e, for these simulations E_h was set to 0 for simplicity. It is possible to deduce that setting E_h to 0 ensures the resonances with the third and fourth levels are evenly spaced. We can then see that the steps alternate between transfer to the third and fourth levels, so while the resonance with each individual level is separated by $2E_e$ this leads to the spacing of E_e shown in figure 3.22 because we need to account for transfer into both upper levels.

The reason for the steps to be so sharp, with a small change in Ω causing a large change in the behaviour in the system is because as Ω is increased the Stark shift increases, if this Stark shift is just large enough to pass through a resonance created through wave mixing there will be a population transfer causing the change in behaviour.

For parameter sets with $\Delta \gg \Omega$ the wave mixing resonances would not be strong enough to cause and noticeable transfer and the Stark shift will will be smaller, and therefore less likely to induce a crossing at all. The quantitative details regarding how wave mixing generates extra resonances within the system is left until the next

chapter 4, including an analysis of when wavemixing should be expected to interfere with systems similar to this.

3.4 Read/Write

In this section we discuss the read and write processes, which includes both the ability of the memory to absorb and emit the signal photons well as the ability to distinguish the retrieved signal photon from other photons also produced during the readout process, this ultimately leads to an analysis of the feasibility of the overall quantum memory. We will refer to any non-signal photons produced during the readout as noise photons.

3.4.1 Noise Sources

Each process performed on the ensemble in the memory protocol will be imperfect, and have a fidelity (or probability of success) σ. These imperfections will either reduce the probability of retrieving the photon, increase the number of noise photons on retrieval or both.

The noise can be filtered from the signal in several ways. The first is through polarisation. The control pulse contains around 10^{10} photons, but will be polarised orthogonally to the signal photon, which in theory allows these photons to be filtered out completely. Off the shelf polarisation filters with an extinction ratio of $10^4 : 1$ have a transmission ratio of $95\% - 98\%$ [67]. A back of the envelope calculation gives a requirement for two or three filters in series giving a transmission rate of between 86% and 96%.

The second filter mechanism is through frequency. The signal photon will be emitted from the $2 \rightarrow 3 \rightarrow 1$ transition with an energy $E_{31} - \Delta$. There will also be photons emitted though the $1 \rightarrow 4 \rightarrow 2$ transition which have a frequency of $E_{31} - \Delta + 2E_e$ and the same polarisation as the signal photon, which can be filtered spectrally. Any remaining control field that is not successfully filtered through polarisation can also be filtered spectrally as it will have an energy of $E_{31} - \Delta + E_e$. The experimental implementation of spectral filtering is beyond the scope of this thesis, but for simplicity we assume the idealised condition where the filters can eliminate these sources of extra photons. These filtering assumptions leave only the transfer of population from $2 \rightarrow 3 \rightarrow 1$ to be considered towards the noise contribution as this will have both the

same polarisation and frequency as the signal photon. Temporal filtering is not possible as the noise occurs during the signal photon emission.

The final filtering mechanism we discuss is spatial filtering. Noise that is both of the same polarisation and frequency as the signal photon will not be distinguishable from the signal if it reaches the detector. The detector size is determined by the distribution of the signal photon field which will depend on many factors including the input photon distribution and diffraction. If we considered the ensemble to be embedded in a waveguide, the probability of a spontaneously emitted photon being into the mode that reaches the detector is given by $\frac{\beta}{2}$ where β is the probability of the emission into the waveguide mode. While we are considering the free space case in this thesis, we will borrow this terminology. The equivalent β is then determined by the overlap of the emission probability of a dipole emitter with the detector area. A wider ensemble of dots would decrease diffraction, allowing for a smaller detector but would also increases the amount of noise by increasing the number of dots. The optimisation of the size and shape of the ensemble is an important factor when designing a quantum memory but is beyond the scope of this thesis. We shall leave β as an unknown parameter in this analysis.

We can therefore see that embedding the ensemble in a waveguide is actually counter productive to the quantum memory operation. The signal photon will be returned in the same mode that was received and so will be directed towards the detector regardless of the existence of a waveguide but we also need to minimise the spontaneously emitted photons that reach the detector. Therefore embedding the memory into a wave guide with large β is actually counter productive, since a high β waveguide will preferentially emit noise into the direction of the detector, greatly increasing the final noise detection. Assuming that the levels of noise are not trivial, free space or a waveguide with a particularly low β is therefore necessary for the quantum memory to function.

3.4.2 Photon Storage

It is important to understand that the spin wave which stores the information of the photon is stored in the coherences between the electron spins in each dot, rather than in the raw population in state $|2\rangle$. These coherences define not only the existence of the photon state but (when combined with the control pulse) the direction in which it will be emitted, which happens to be in the direction of the control pulse. While an amount of population in state $|2\rangle$ is a part of the spin wave, we shall see that the majority of the population will have no correlations across the ensemble. This

population will partially pumped out as noise during read meaning that the angular distribution of the noise photons will be the same as a single dipole emitter.

In a collection of papers by A.V. Gorshkov et al [32–34] have given a detailed analysis of the properties of Λ ensemble memories. This was achieved by considering how to reliably map an incoming photon onto a spin wave across the ensemble of Λ systems. Their findings have shown that the parameter that fundamentally limits the retrieval fidelity is the optical depth of the ensemble. This is because the ratio between collectively enhanced emission into the desired signal modes and spontaneous decay into undesired modes depends only on the optical depth [33]. Inhomogeneous broadening does reduce the fidelity of the transition for a given arrangement of dots, but this can be overcome by increasing the number of dots, and therefore the optical depth of the memory further.

Papers [32, 33] show that the fidelity of the read and write process in an ensemble of Λ systems is completely determined by the resonant optical depth, defined by $d = \ln\left(\frac{\text{Incident radiation}}{\text{Transmitted radiation}}\right)$ for monochromatic resonant light:

$$d = \frac{g^2 N L}{\Gamma c}, \tag{3.15}$$

where $g^2 = \mu_{ij}^2 \nu / (2\hbar\epsilon_0 A L)$ and N is the total number of dots. Note that the resonant optical depth refers to the maximum spectral absorption, not the spectrally integrated absorption. Stronger optical coupling also increases the spectral width of the peak such that resonant optical depth is actually independent of the absorption coefficients of the dots themselves. This can be seen clearly by using Fermis golden rule to substitute $\Gamma = \mu_{ij}\nu^3 / (3\pi\epsilon_0\hbar c^3)$, which gives in the following:

$$d \approx n L \lambda^2, \tag{3.16}$$

where n is the atom/dot density, L is the physical length of the sample and λ is the wavelength of the photon. This is extended in [34] for ensembles with inhomogeneous broadening to the resonant optical depth $d' = d\frac{\Gamma}{\Delta^I}$, where Δ^I is the inhomogeneous broadening width and Γ is the decay constant between the pair of levels coupled to the photon mode.

The read/write protocol we will consider here is Stimulated Raman transfer introduced in section 2.5.2 which has been demonstrated for use a a quantum memory protocol with experiments using caesium vapour[63]. For both the caesium experiments and the analysis by A.V. Gorshkov et al only Λ systems are used. For the case of quantum dots in the Voigt geometry we must deal with a fourth level creating a double

Λ system. Next we will discuss the effect of the fourth level in the systems and how, if at all it will interfere with the protocol.

Starting from the Hamiltonian in equation (2.17) that describes the two level effective dynamics in the Voigt geometry, we will first look at the two photon detuning. Here Ω_2 is a single photon and Ω_1 is the control pulse, so $\Omega_2 \ll \Omega_1$ and so we can ignore the Stark shift from the Ω_2 field. The effective detuning for the three level Λ system is $\Delta_{\text{eff}}^{\Lambda} = \delta - \frac{\Omega_1^2}{\Delta}$ and for the Voigt geometry is $\Delta_{\text{eff}} = \delta - \Omega_1^2 \left(\frac{1}{\Delta} - \frac{1}{\Delta_4} \right) \approx \delta$ since $\Delta \approx \Delta_4$. We can see that the detuning in the Voigt geometry is actually much more stable than the detuning in the original Λ case almost completely removing the resonance dependence on the control laser power Ω_1, simplifying the experimental procedure. While we believe this decrease in detuning should offer a slight improvement to the transition over the basic Λ system if large intensity controls are required, it should however not fundamentally alter the dynamics, and therefore the analysis by A.V. Gorshkov et al should still be relevant to the Voigt geometry.

The second effect of the fourth level in the Voigt geometry is to introduce a second coherent transition mode during write $1 \to 4 \to 2$ with the same strength as the desired $1 \to 3 \to 2$ transition but detuned by $2E_e$. The strength of the coupling is given by $\Omega_{\text{eff}} = \frac{\Omega_1 \Omega_2}{2\Delta}$. Since we are in the Raman regime $\Omega_1, \Omega_2 \ll \Delta$ and because Ω_2 is also a single photon field, $\Omega_2 \ll E_e$ which implies that $\Omega_{\text{eff}} \ll E_e$, therefore the transition probability via level four will be many times smaller than the transition via level three and its interference with storage of the photon can be ignored, as we did for the rotating wave approximation.

The $1 \to 4 \to 2$ transition can however incoherently pump population into state $|2\rangle$. This is not possible within the Λ system since the control pulse is not directly coupled to state $|1\rangle$ in the Λ case. The amount of population pumped via level four can be calculated by integrating equation (2.29) over the read pulse of length T and is given by:

$$\frac{T\Gamma\Omega^2}{4\Delta^2 + \Omega^2}, \tag{3.17}$$

which will add noise to the system. We therefore directly use the results from Λ system memories and add an extra noise contribution to the system due to the pumping during write and read.

3.4.3   Loss and Noise Contributions

We only consider the photons emitted from pumping $2 \to 3 \to 1$ as noise as we assume all other contributions will be filtered out to a level in which they are insignificant. The rate of emission during readout can be determined from the rate of pumping given in section 2.5.4 which is proportional to the population in state $|2\rangle$. If there were global coherences across the ensemble that corresponded to emission in a particular mode then there would be directionally controlled emission, here we shall argue that there are no coherences across the ensemble except for the desired signal. We therefore assume that the noise photons will be emitted in random directions with a probability density determined by the emission probability of a dipole. Since the emission is directly proportional to the population in state $|2\rangle$ we will now go on to discuss the various contributions to the level $|2\rangle$ population during readout and the loss of the signal photon incurred from each the four sections of the memory: Initialisation, Write, Storage and Read.

Initialisation: The fidelity of initialisation σ_{init} contributes directly to the population in state $|2\rangle$. Here we also make the naive assumption that the imperfect initialisation only reduces the optical depth by reducing the number of resonators in state $|1\rangle$ absorbing the photon while not further impeding the read/write process. The assumption that the population in state $|2\rangle$ during write doesn't interfere with the process should be investigated within the model of ref [34] or similar with an inclusion of imperfect initialisation and is beyond the scope of this thesis.

Write: Imperfect write, as described in ref [34] contributes directly to loss of the photon with probability of success σ_{write}. However in the Voigt geometry there is also the separate process of pumping described in section 3.4.2 that pumps population through level four, contributing to the state $|2\rangle$ population. The total pumped population $1 - \sigma_{\mathrm{P\ write}}$ can be calculated from section 2.5.4.

Storage: Decoherence during storage contributes linearly to the loss [32] of the photon on retrieval with the fidelity due to decoherence given by σ_{dec}. The fidelity of the two π pulses σ_π for the spin echo contribute to both loss of the photon and extra population in state $|2\rangle$.

Read: ref [33] shows that the read and write processes have the same fidelity $\sigma_{\mathrm{write}} = \sigma_{\mathrm{read}}$, we can also infer that the amount of pumped population will be the same, however since the population is not transferred before the noise is created, but rather during during noise emission we can infer that the relevant contribution for the noise is half of that during write $\sigma_{\mathrm{P\ read}} = \frac{1}{2}\sigma_{\mathrm{P\ write}}$.

The final fidelity of the photon retrieval is given by:

$$\sigma_{\text{out, total}} = \prod_i \sigma_{i \text{ loss}} = \sigma_{\text{write}}\sigma_{\text{dec}}\sigma_\pi^2 \sigma_{\text{read}}\sigma_{\text{filter}} \tag{3.18}$$

and the final population in level 2 contributing to noise is given by:

$$\rho_{22} = 1 - \prod_i \sigma_{i \text{ noise}} = 1 - \sigma_{\text{init}}\sigma_{\text{P write}}\sigma_\pi^2 \sigma_{\text{P read}} \tag{3.19}$$

where $\sigma_{i\text{loss}}$ and $\sigma_{i\text{noise}}$ correspond to the fidelities of every process relevant to either state loss or to noise generation respectively.

3.4.4 Noise Example

We now calculate the signal retrieval and noise output for our typical ensemble.

Fidelities with optimal parameters for initialisation (figure 3.11) and π pulses (figure 3.20) for the typical ensemble have been calculated to be $\sigma_{\text{init}} = 0.97$ and $\sigma_\pi > 0.997$ respectively. σ_{dec} is completely dependent on the properties of the dots and the length of time that the state is stored for. Here we will choose an example of a 0.1μs storage time for an ensemble with a decoherence time of $T_2 = 3\mu$s which gives $\sigma_{\text{dec}} = 0.97$.

The fidelities associated with write and read are strongly dependent on the optical depth of the dot ensemble and the intensity of the control field used. For our typical ensemble $d' \approx \frac{d\Delta_I}{\Gamma} = \frac{d}{2500}$. We assume that we can choose the length of the ensemble and therefore choose d to be a value such that it is not the dominant loss term and as such we will set $d' = 40$ resulting in a write/read fidelity $\sigma_{wr} = 0.99$ [34] which gives $N = 100000 \times \left(\frac{\text{width}}{\lambda}\right)^2$. At a fairly dense dot distribution of $4 \times 10^{14}m^{-2}$[46] the number of dots per layer that are in an area λ^2 would be approximately 100. 1000 layers would be required for the full memory with these parameters, which is an order of magnitude beyond current achievements [39, 76].

While the method for optimisation of the control field Ω for inhomogeneously broadened ensembles is discussed at length in ref [34], its value is not explicitly stated for our case. For the sake of providing an example we will use the value

$$\Omega_{\text{opt}} \approx \frac{\Delta}{\sqrt{\Gamma T d'}}, \tag{3.20}$$

which can be inferred from the similar case with a Lorentzian inhomogeneous broadening profile case, rather than the Gaussian profile in typical dot ensembles. The optimal control field also only accounts for optimal retrieval and does not consider minimising

the noise output. Therefore a control field that is also optimised to minimise noise may differ significantly from this in reality. We therefore use this only as rough example to infer the plausibility for the overall quantum memory process.

The population pumped from state $1 \to 4 \to 2$ during write and read can be calculated from equation (3.17) after substituting in Ω from equation (3.20). The total transferred population during write becomes $\frac{1}{d'} = 0.025 = 1 - \sigma_{\text{P write}}$.

The above parameters provide the expected retrieval efficiency of the photon:

$$\sigma_{\text{out, total}} = 0.99 \times 0.97 \times 0.997^2 \times 0.99 \times 0.94 = 0.89 \tag{3.21}$$

We can see that the largest loss factors are the losses due to the polarisation filters, which is fixed and the T_2 decoherence which is directly dependent on the storage time, the other parameters are limited by properties of the dot ensemble or protocols which can be optimised further if necessary, and therefore not directly limiting the feasibility of the memory.

The total uncorrelated population contributions from initialisation, write, read and two RCAP transitions in equation (3.19) is:

$$\rho_{22} = 1 - 0.97 \times 0.975 \times 0.997^2 \times 0.987 = 0.072. \tag{3.22}$$

We can see that the largest contribution to noise is the initialisation procedure. This value was found to be limited by the properties of the dots themselves and cannot easily be reduced. See section 3.1 for full details. This is therefore a minimum level of noise that must be sustained by memory protocol and could potentially break the feasibility of the quantum memory protocol, if this level of noise is too high.

The total pumped population from $2 \to 3 \to 1$ during readout gives the number of noise photons emitted. This population transfer can be derived from equation (2.29), from Ω given by equation (3.20), the definition of optical depth in (3.16) and while assuming $\Gamma \ll \Delta$ and $4Td'\Gamma \gg 1$. This results in the following number of noise photons:

$$NT \frac{\Gamma(\frac{\Delta^2}{\Gamma T d'})\rho_{22}}{4(\Gamma^2 + \Delta^2) + (\frac{\Delta^2}{\Gamma T d'})} \approx \frac{\rho_{22}\Delta^I}{4\Gamma} \left(\frac{\text{width}}{\lambda}\right)^2, \tag{3.23}$$

where "width" is the width of the dot ensemble, specifically the section of the ensemble that can be considered active in the memory protocol. Equations (3.23) and (3.22) result in an emission of $45\left(\frac{\text{width}}{\lambda}\right)^2$ noise photons by the ensemble.

The probability of an emitted noise photon being received at the detector $\frac{\beta}{2}$ determines the total number of noise photons that are detected, which is

$$\text{Detected Noise} = 45\beta \left(\frac{\text{width}}{\lambda}\right)^2, \tag{3.24}$$

in the limit that this expected number of photons is much less than 1.

β, which is based upon the size of the detector, is dependent on the spread of the emitted signal as the detector must be wide enough to capture the photon. The spread is dependent on many factors including diffraction due the size and shape of the ensemble. Finding the ensemble shape which minimises equation (3.24) is an important part of designing the quantum memory but is beyond the scope of this thesis.

To be within a correctable level of error with the 10% loss rate calculated above the probability of a computational error must be less than 0.0035[4] for current error correction protocols. There are two photon storage modules per quantum memory and therefore double the photons calculated above will reach the quantum computer. If we assume that there is no mechanism to detect multi-photon errors in the computation then the noise expectation per each photon memory operation must be half this, 0.0017. If the detected noise in equation (3.24) can be minimised below 0.0017 photons per readout then the memory can function within current fault tolerance models. If the computation can differentiate multi photon events then computational errors will only occur when the signal photon is simultaneously lost while a noise photon is created. This will result in a factor of 10 fewer computational errors in our example, a considerably less strict condition.

3.4.5   In-plane Read/Write

Ultimately storage and retrieval with the in-plane geometry is unlikely to be a viable memory method, but we have included a brief discussion here for completeness. The in-plane geometry storage would require the strong control and weak signal pulses to be distinguished spectrally rather than through polarisation as is the case for the out-of-plane Voigt geometry, which in itself would be a significant challenge. The Raman transition still exists $1 \xrightarrow{\Omega} 3 \xrightarrow{\gamma} 2$ and there is now a second Raman transition $1 \xrightarrow{\Omega} 4 \xrightarrow{\gamma} 2$, shown in figure 3.24a where γ refers to the photon field and Ω the control field. For both cases the phases align and so these two transitions combine constructively.

There is also significant transfer through $1 \xrightarrow{\Omega} 3 \xrightarrow{\Omega} 2$ and $1 \xrightarrow{\Omega} 4 \xrightarrow{\Omega} 2$, because the control pulses now couple to both sides of each Λ system and can generate coherent transfer between the levels. This control-control transfer is detuned and strong so
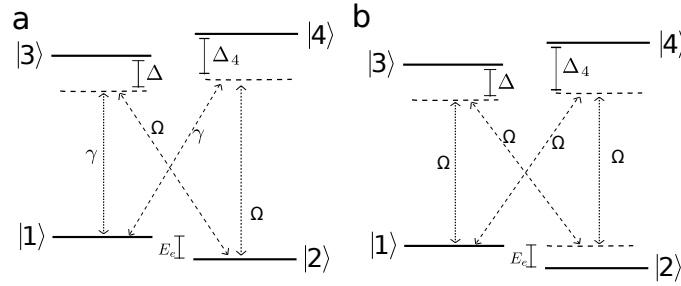
Fig. 3.24 two independent coupling mechanisms present during an in-plane geometry read/write

will create fast oscillating population transfer. The population transferred by the control-control coupling will be larger than the population transferred by the photon-control coupling despite the detuning, since γ is a single photon and Ω is a strong laser pulse, composed of approximately 10^{10} photons for a nJ control pulse used in current experiments [63]. If the amplitude of these oscillations is considerably less than 1 then the fast oscillations will not significantly effect the dynamics of the spin wave coherences, and so the final state of population transferred through the photon-control process would not be significantly changed while the population transferred through the control-control interaction would be on average half the height of the oscillations, contributing to the final noise population only. The pulses are not applied adiabatically with respect to the lower levels, and so the control-control coupling will induce Rabi oscillations rather that temporary state mixing. The height of the rabi oscillations will be given by:

$$\text{rabi}_{\text{height}} = \frac{1}{2} \frac{\Omega_{\text{eff}}^2}{\Omega_{\text{eff}}^2 + E_e^2}. \tag{3.25}$$

An approximate value for the Ω and therefore Ω_{eff} is given in section 3.4.4, applying that to equation (3.25) with the values for our typical ensemble results in a maximum oscillation height of around 0.4. This transfer is not much less than 1 and so will interfere with the dynamics of the spin wave and also the average transfer of 0.2 per dot for each transition will generate significantly more noise than the out-of-plane case, which is also likely to be limited by its noise emission.

3.5 Quantum Memory Conclusions

We have investigated the potential for QDs to be used as a quantum memory, particularly focussing on protocols for the initialisation and π pulses required for a fully

functioning memory. We combined this with the research by A Gorshkov [34] for the fidelity of the write and read process itself to discuss the feasibility of using QDs as a quantum memory.

We have shown that there are limits to the fidelity of retrieval which can be achieved in our typical ensemble, which are primarily based on the quality of the optical filters to differentiate the signal photon and the decoherence while the state is stored. The ability to build the necessary hardware (> 1000 layers of QDs) is also a significant barrier for realisation. Assuming that the hardware requirements can be achieved we have shown that retrieval rates can be placed within the limits of fault tolerant quantum computing.

We have calculated the expected noise photon count for a typical memory to be around 45 photons, compared to 1 signal photon. The number of noise photons is primarily influenced by the initialisation fidelity, the number of dots in the ensemble and the intensity of the read control pulse. The initialisation fidelity is limited almost entirely by the Zeeman splittings (E_e and E_h) and the decay rates Γ_{ij} of the QDs. The optimisation of the read control pulse is beyond the scope of this thesis, further work in this area may lead to an improved control pulse intensity profile which both maximises the returned signal while minimising the noise emission, decreasing the expected number of noise photons. The total number of noise photons emitted during readout provides a strict limit to the probability β of an emitted noise photon entering the detector or quantum computer.

We have shown that for both the initialisation and π pulse protocols that the inhomogeneous broadening of the quantum dots does not pose a significant reduction in fidelity. The write and read protocols do however suffer from a reduced efficiency for large inhomogenous broadening, requiring significantly more dots for broadened ensembles, which in turn leads to significantly more noise being emitted.

Chapter 4

Wave Mixing

In this section we depart from considering the properties of quantum dots specifically and move onto the properties of some more general theoretical models of wave mixing. This research was motivated by the anomalies noted at the end of the previous chapter, specifically we argued that the steps in figure 3.22 were due to population transfer involving N-wave mixing.

Wave mixing in its broadest terms is the effect of multiple photons interacting within a physical medium to create new photons with frequencies that are given by a sum of the incoming photon frequencies. The energy level diagram for a 4-wave mixing example is shown in figure 4.1. Here there are two lasers applied to the system, Ω_1 and Ω_2 of different frequencies ω_1 and ω_2, such that $\omega_2 - \omega_1 = \delta_\omega$. From the internal atom dynamics we can consider the photons interaction though virtual levels which do not get significantly populated, in the same way we described the Raman transition previously. Two photons from laser 2 and a photon from laser 1 can interact to create an output photon ω_3 in red.

Wave mixing creates extra couplings between the energy levels in the system at frequencies that would not otherwise occur. This leads to a spectrum of evenly spaced delta functions, or when viewed from the point of view of the internal dynamics, creates an array of resonance conditions that in general need to be avoided. This research was motivated by a loss of fidelity within the simulations of a population transfer protocol done in the previous chapter that was caused by large orders of wave mixing. As four and six wave mixing are commonly abbreviate 4 wave mixing and 6 wave mixing, we will collectively refer to higher orders as N-wave mixing where N refers to (an often arbitrary) wavemixing order number.

In general we could consider any number of different incoming frequencies, here we will only consider the case of two frequencies from two incoming lasers, or equivelantly
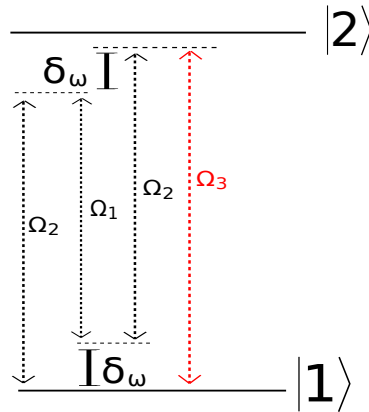
Fig. 4.1 The energy level diagram for 4-wave mixing for a two level system. Three incoming waves shown in black generate the fourth outgoing wave, shown in red, which is not of the same frequency. The two dotted lines can be considered as virtual levels and act like Raman transitions.

from a single laser before taking the rotating wave approximation, therefore including its own counter rotating term in the Hamiltoninan. Wave mixing can occur whenever the graph of couplings (examples in figure 4.2) contains a closed loop which is not self resonant (defined below). This is to say that there are two paths through which population can be transferred between two energy levels in the system, and that these two paths are not resonant under the same conditions. These two paths provide a loop through which population can be transferred around the system, through which the frequency accumulated by traversing the loop once is given by the frequency difference between the two coupling paths. The self resonant case is the trivial case when there is no frequency accumulated. The frequency accumulated can be calculated by summing the frequencies of each coupling term in the Hamiltonian that is involved in the loop, taking special care to include the sign of the frequencies. This is valid regardless of whether the lab frame or a rotating frame is chosen. For example, the graph for the four level system from equation (3.7) is shown in figure 4.2 with the closed loop in red. From appropriately adding and subtracting the frequencies of the coupling terms in equation (3.7) we find that the accumulated frequency from one rotation is $2\omega_1 - 2\omega_2 = 2\delta_\omega$. Self-resonance therefore only occurs at the trivial case for $\omega_1 = \omega_2$.

Wave mixing is generally considered from the perspective of the optical interactions with a medium, which mediates interactions between incoming photons. Wave mixing calculations are generally used to determine the frequencies and modes of output photons, which are calculated through perturbation theory. The response of the medium can then be written in terms of the incoming electric field and the n'th rank
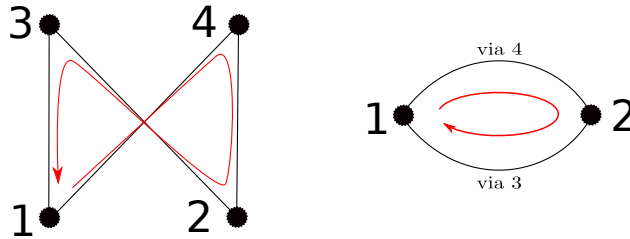
Fig. 4.2 a.) The coupling graphs between the states of a quantum dot in the Voigt geometry from the previous chapter. The closed loop is shown in red. b.) shows the ground state two level equivalent system coupling graph after adiabatic elimination, which is the equivelent of two lasers coupled to a single two level system.

non-linear susceptibility tensor [52, 75]. This approach is also only appropriate when the electric fields are sufficiently weak that perturbation theory is valid. In this chapter we instead wish to consider wave mixing from the perspective of the dynamics of an isolated atom with a linear dipole interaction. We have developed an alternative approach that allows the effects of large orders of wave mixing on the atom dynamics to be calculated.

We will now go on to build a model through which these mixing effects can be fully understood. Using this we can identify how strong these extra couplings are, and with which parameters they will occur. This can then be used to calculate when transfer events occur and how much transfer will occur. We will then go on to propose a protocol where this normally disruptive process can be used in a controlled way to achieve coherent population transfer.

4.1 SCRAP

We have found that the transfer of population with wave mixing investigated in this chapter is very similar to the Stark Chirped Rapid Adiabatic Passage (SCRAP) protocol which we will introduce now.

The simplest case of Stark Chirped Rapid Adiabatic Passage (SCRAP) consists of a two level system with two couplings. One strong coupling is far detuned from resonance and used only to Stark shift the energy splitting of the two level system and one weak coupling is applied with a resonance just above the bare state energy of the system. The pulses are applied sequentially with an overlap, the same as for STIRAP 3.2.2. Also similar to STIRAP, the Stark shift causes two avoided crossings to occur between the energy level splitting and the weak pulse, but since the weak pulse is only applied with a partial overlap, only one crossing transfers population.
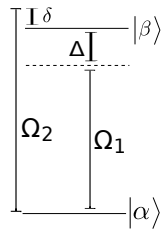
Fig. 4.3 Energy level diagram for a SCRAP protocol. For SCRAP Ω_1 is a strong pulse with a large detuning Δ which is used to induce a Stark shift, while Ω_2 is a weak pulse detuned slightly above the energy level splitting with δ small and positive that causes an avoided crossing to occur as the Stark shift changes the energy splitting of the states.

The two-level SCRAP case has the energy level structure given in figure 4.3 with the dynamics shown in figure 4.4, this can be a successful protocol to transfer population with a very high fidelity. However, for our four level case there is a complete overlap between the weak resonance, caused by wavemixing and the Stark shift caused by both RCAP lasers, meaning that both resonances will occur, and for general parameters neither are likely to be of a high fidelity. We can see one example for this in figure 3.23.

4.2   Theoretical Formulation

The two level system in figure 4.3 with Hamiltonian given in equation (4.1) has two frequencies coupled to it and is the simplest possible example with a non self resonant closed loop of couplings required for wave mixing, assuming $\delta \neq 0$.

We also note that this is an identical Hamiltonian to equation (2.9), which is a two level system coupled to a single wave before the rotating wave approximation is applied. In general, for this Hamiltonian, the faster rotating term is eliminated because for most situations its effects are irrelevant. However as we are interested in these effects this term cannot be eliminated. While wave mixing effects are often investigated through perturbation theory this is also insufficient for our purposes as we want to consider high order effects involving large incoming electric fields.

This Hamiltonian is inherently time dependent. The time dependence also cannot be considered to be adiabatic, which presents difficulties in calculating the eigenvalues of the system as these need to be considered in a time independent frame. Instead we have developed the following technique to produce a time independent Hamiltonian which we can then solve:
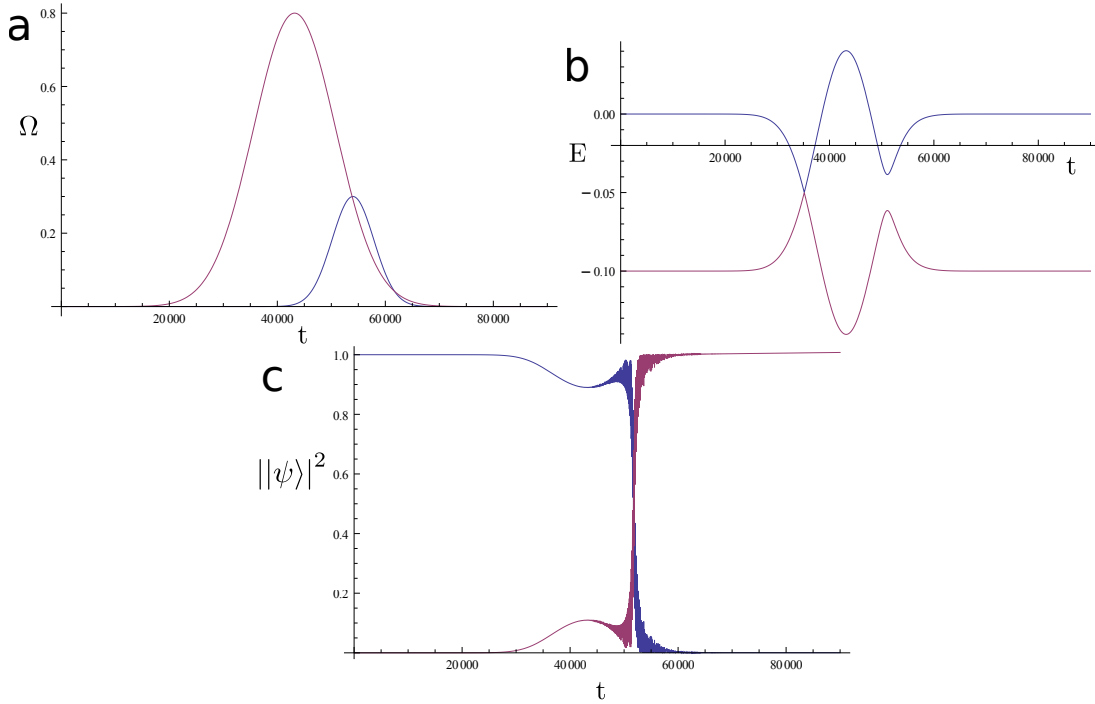
Fig. 4.4 a.) The coupling strengths for the SCRAP protocol, the large pulse is detuned away from resonance by $\Delta = 1$ and Stark shift the energy splitting of the levels whist the weaker pulse is detuned slightly above resonance by $\delta = 0.1$, such that the Stark shift sweeps through resonance with the state b.) The dressed state representation of the process, showing the avoided crossing. Since it is not possible to write the Hamiltonian in a time independent frame this plot shows how the dressed states look if the effects of the Stark coupling and resonant coupling are dealt with separately. c.) The bare state populations throughout the process, an amount of population in state $|\psi_2\rangle$ through state mixing before the avoided crossing causes nearly complete transfer from $|\psi_1\rangle$ into $|\psi_2\rangle$.

We first redefine the variables for this chapter, such that $E_0 \to \Delta$, $\Omega_{\text{eff}} \to \Omega$ and $\omega_2 - \omega_1 \to \delta$ giving us the Hamiltonian:

$$H = \tfrac{1}{2} \begin{pmatrix} -\Delta & \Omega(1+e^{i\delta t}) \\ \Omega(1+e^{-i\delta t}) & \Delta \end{pmatrix} \tag{4.1}$$

We then use the time independent Schrödinger equation:

$$H\psi = i\frac{d\psi}{dt} \tag{4.2}$$

Where

$$\psi(t) = \begin{pmatrix} \alpha(t) \\ \beta(t) \end{pmatrix} \tag{4.3}$$

This results in the following pair of coupled equations:

$$
\begin{aligned}
\frac{d\alpha(t)}{dt} &= -i\tfrac{1}{2}\alpha(t)\Delta + i\tfrac{1}{2}\Omega(1+e^{(i\delta t)})\beta(t) \\
\frac{d\beta(t)}{dt} &= i\tfrac{1}{2}\beta(t)\Delta + i\tfrac{1}{2}\Omega(1+e^{(-i\delta t)})\alpha(t)
\end{aligned}
\tag{4.4}
$$

We now define an infinite set of states

$$|\psi_\infty(t)\rangle = (...,\alpha_{k-2}(t),\beta_{k-1}(t),\alpha_k(t),\beta_{k+1}(t),\alpha_{k+2}(t),\beta_{k+3}(t),\alpha_{k+4}(t),\beta_{k+5}(t),...) \tag{4.5}$$

Where the α_k's and β_k's are are identical to the original α and β, but are now treated as independent variables. We shall see later that each copy of α and β represents a new virtual level introduced in figure 4.1. Using this new set of states we can rewrite equation (4.4) as:

$$
\begin{aligned}
\frac{d\alpha_k(t)}{dt} &= -i\tfrac{1}{2}\alpha_k(t)\Delta + i\tfrac{1}{2}\Omega(\beta_{k-1}(t) + \beta_{k+1}(t)e^{(i\delta t)}) \\
d\frac{\beta_{k+1}(t)}{dt} &= i\tfrac{1}{2}\beta_k(t)\Delta + i\tfrac{1}{2}\Omega(\alpha_{k+2}(t) + \alpha_k(t)e^{(-i\delta t)}),
\end{aligned}
\tag{4.6}
$$

which results in an infinite set of chain-linked states. This set of equations can be written out in the form of the Schrödinger equation using the infinite set of states from equation (4.5) and a corresponding infinite Hamiltonian:

$$
\frac{d}{dt}
\begin{pmatrix}
\vdots \\
\beta_{-1}(t) \\
\alpha_0(t) \\
\beta_1(t) \\
\alpha_2(t) \\
\beta_3(t) \\
\alpha_4(t) \\
\vdots
\end{pmatrix}
=
\frac{i}{2}
\begin{pmatrix}
\ddots & \ddots & 0 & 0 & 0 & 0 & 0 & 0 \\
\ddots & -\Delta & \Omega & 0 & 0 & 0 & 0 & 0 \\
0 & \Omega & \Delta & \Omega e^{(-i\delta t)} & 0 & 0 & 0 & 0 \\
0 & 0 & \Omega e^{(i\delta t)} & -\Delta & \Omega & 0 & 0 & 0 \\
0 & 0 & 0 & \Omega & \Delta & \Omega e^{(-i\delta t)} & 0 & 0 \\
0 & 0 & 0 & 0 & \Omega e^{(i\delta t)} & -\Delta & \Omega & 0 \\
0 & 0 & 0 & 0 & 0 & \Omega & \Delta & \ddots \\
0 & 0 & 0 & 0 & 0 & 0 & \ddots & \ddots
\end{pmatrix}
\begin{pmatrix}
\vdots \\
\beta_{-1}(t) \\
\alpha_0(t) \\
\beta_1(t) \\
\alpha_2(t) \\
\beta_3(t) \\
\alpha_4(t) \\
\vdots
\end{pmatrix}
\tag{4.7}
$$

Equations (4.7) have identical dynamics to equations (4.4), but can now be transformed into a time independent rotating frame. This gives:

$$
\frac{d}{dt}
\begin{pmatrix}
\vdots \\
\beta'_{-1}(t) \\
\alpha'_0(t) \\
\beta'_1(t) \\
\alpha'_2(t) \\
\beta'_3(t) \\
\alpha'_4(t) \\
\vdots
\end{pmatrix}
=
\frac{i}{2}
\begin{pmatrix}
\ddots & \ddots & 0 & 0 & 0 & 0 & 0 & 0 \\
\ddots & -\Delta+2\delta & \Omega & 0 & 0 & 0 & 0 & 0 \\
0 & \Omega & \Delta+2\delta & \Omega & 0 & 0 & 0 & 0 \\
0 & 0 & \Omega & -\Delta & \Omega & 0 & 0 & 0 \\
0 & 0 & 0 & \Omega & \Delta & \Omega & 0 & 0 \\
0 & 0 & 0 & 0 & \Omega & -\Delta-2\delta & \Omega & 0 \\
0 & 0 & 0 & 0 & 0 & \Omega & \Delta-2\delta & \ddots \\
0 & 0 & 0 & 0 & 0 & 0 & \ddots & \ddots
\end{pmatrix}
\begin{pmatrix}
\vdots \\
\beta'_{-1}(t) \\
\alpha'_0(t) \\
\beta'_1(t) \\
\alpha'_2(t) \\
\beta'_3(t) \\
\alpha'_4(t) \\
\vdots
\end{pmatrix}
\tag{4.8}
$$

Where the rotating states are no longer identical, but related by $\alpha'_k(t) = \alpha_k(t)e^{i\delta\frac{k}{2}t}$ and $\beta'_k(t) = \beta_k(t)e^{i\delta\frac{k+1}{2}t}$. The starting population of each state is given by:

$$
|\psi_\infty(0)\rangle = (...,\alpha(0),\beta(0),\alpha(0),\beta(0),\alpha(0),\beta(0),\alpha(0),\beta(0),...),
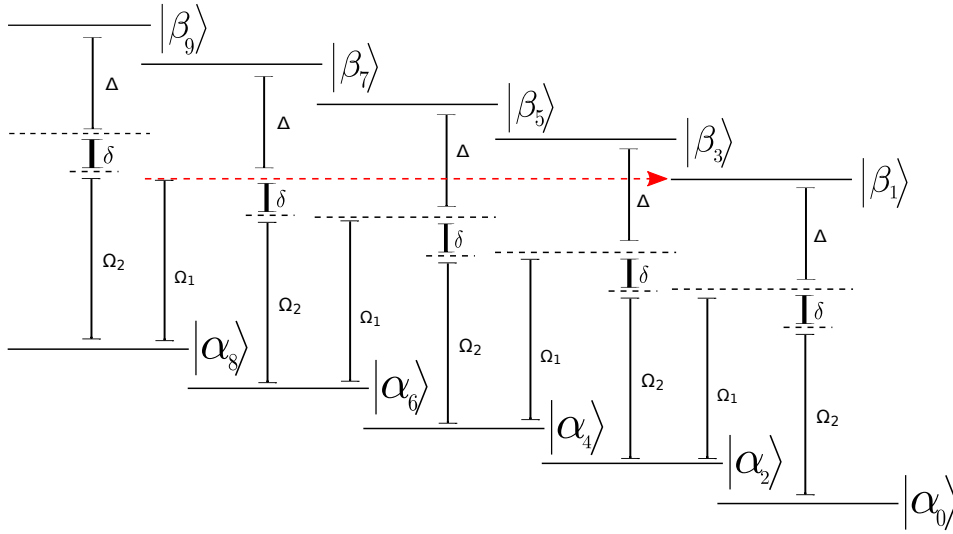\tag{4.9}
$$

Fig. 4.5 Energy levels of the expanded Hamiltonian in the rotating, time independent frame (equation (4.8)), for the case of 8 wave mixing, when $\Delta = 3\delta$. $|\alpha_8\rangle$ is on resonance with $|\beta_1\rangle$ and there are 6 intermediate levels: $|\alpha_8\rangle \rightarrow |\beta_7\rangle \rightarrow |\alpha_6\rangle \rightarrow |\beta_5\rangle \rightarrow |\alpha_4\rangle \rightarrow |\beta_3\rangle \rightarrow |\alpha_2\rangle \rightarrow |\beta_1\rangle$

which importantly is not normalised in the normal sense of a wavefunction, by summing up each term, since this isn't a real system, instead this state is normalised such that $|\alpha_k(t)|^2 + |\beta_m(t)|^2 = 1$ for all k and m. In an infinite system the dynamics are identical for each $\alpha_k'(t)$ and each $\beta_k'(t)$ and they will therefore evolve identically. We can therefore write, without loss of generality, that the state of the extended system will be given by:

$$|\psi_\infty'(t)\rangle = (..., \alpha(t)e^{\frac{i}{2}\delta(k-2)t}, \beta(t)e^{\frac{i}{2}\delta(k-2)t}, \alpha(t)e^{\frac{i}{2}\delta k t}, \beta(t)e^{\frac{i}{2}\delta k t}, \alpha(t)e^{\frac{i}{2}\delta(k+2)t},$$
$$\beta(t)e^{\frac{i}{2}\delta(k+2)t}, \alpha(t)e^{\frac{i}{2}\delta(k+4)t}, \beta(t)e^{\frac{i}{2}\delta(k+4)t}, ...) \tag{4.10}$$

Where $\alpha(t)$ and $\beta(t)$ are exactly the population in the upper and lower state of our original two level system. From now on I will refer to the infinite matrix in equation (4.8) as the expanded Hamiltonian. Using this time independent Hamiltonian it is now possible to explore the eigenvalues of the system.

4.3 Calculating N-wave mixing strength

Given the expanded Hamiltonian we can now identify the strength and location of high order N-wave mixing resonances. This can be done exactly by calculating the eigenvalues of the expanded Hamiltonian, equation (4.7). Resonances occur at avoided

crossings shown in figure 4.6 with the strength of an effective coupling Ω_{eff} given by the minimum separation of the eigenvalues when on resonance with the N-wave mixing transition, which is is also when the effective detuning $\Delta_{\text{eff}} = 0$. In general $\Delta_{\text{eff}} = \Delta - \Delta_{\text{resonance}}$. For small Ω these occur when $N\delta \approx \Delta$ by considering the coupling between each $\alpha_k(t)$ with all of the relevant $\beta_k(t)$ levels rather than just the two levels directly coupled. For higher Ω the Stark splitting needs to be taken into account.
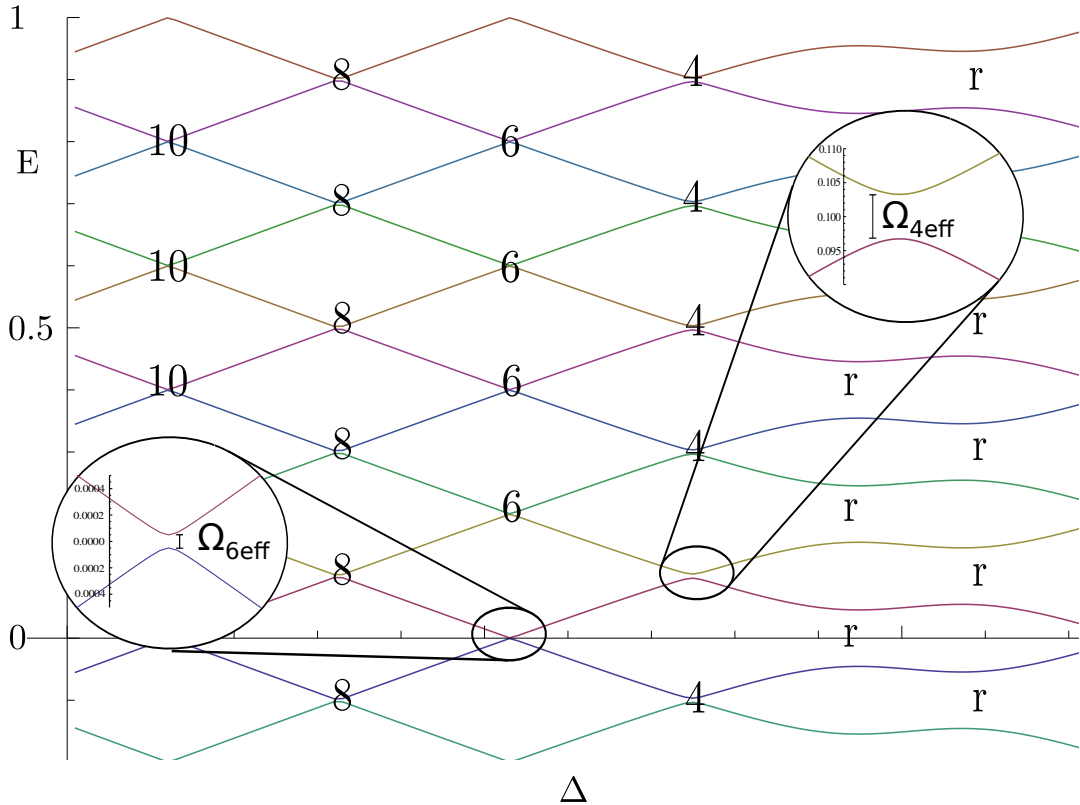
Fig. 4.6 Eigenvalues of the extended Hamiltonian for $\delta = 0.1$, $\Omega = 0.1$ and can be rescaled without altering the topography by keeping δ/Ω constant. Eigenvalues are calculated numerically for a truncated matrix sufficiently large to include the correct dynamics, in this case a 30×30 matrix.

Given the infinite, repeating nature of the expanded matrix shown in Figure 4.6, we only need to consider the two central eigenvalues to understand all of the dynamics of the system. All other eigenvalues are translations of these two and exhibit identical crossings. In Figure 4.6 the two central large avoided crossings correspond to the system on resonance, while the avoided crossings both to the left and right of these correspond to 4,6,8, ... etc wave mixing cases. Two crossings are expanded, corresponding to 4 wave mixing and 6 wave mixing respectively. The plot is for $\delta/\Omega = 1$ and scales linearly with δ and Ω.

Calculating the effective coupling strength for each order of wave mixing is the equivalent to calculating the coupling between two levels connected together by $N-2$ intermediate levels. We can solve this equations as follows, using a truncated version of the extended Hamiltonian. Where $l + (N-1) = k$ gives the order of wave mixing being calculated and n is the number of states included beyond the states being calculated.

We use the time independent Schrödinger equation (4.11) on the extended Hamiltonian to get reach equation (4.12).

$$E\psi = H\psi \tag{4.11}$$

$$
\begin{aligned}
E\psi_{l-n} &= \Delta_{l-n}\psi_{l-n} + \Omega\psi_{l-n+1} \\
&\vdots \\
E\psi_{l-1} &= \Delta_{l-1}\psi_{l-1} + \Omega\psi_l + \Omega\psi_{l-2} \\
\rightarrow E\psi_l &= \Delta_l\psi_l + \Omega\psi_{l+1} + \Omega\psi_{l-1} \\
E\psi_{l+1} &= \Delta_{l+1}\psi_{l+1} + \Omega\psi_{l+2} + \Omega\psi_l \\
&\vdots \\
E\psi_{k-1} &= \Delta_{k-1}\psi_{k-1} + \Omega\psi_k + \Omega\psi_{k-2} \\
\rightarrow E\psi_k &= \Delta_k\psi_k + \Omega\psi_{k+1} + \Omega\psi_{k-1} \\
E\psi_{k+1} &= \Delta_{k+1}\psi_{k+1} + \Omega\psi_{k+2} + \Omega\psi_k \\
&\vdots \\
E\psi_{k+n} &= \Delta_{k+n}\psi_{k+n} + \Omega\psi_{k+n-1}
\end{aligned}
\tag{4.12}
$$

We solve for $\psi_{k+1}, \psi_{k-1}, \psi_{l+1}, \psi_{l-1}$ and substitute these into the ψ_l and ψ_k (arrowed) equations to give the coupling between the two states of interest:

$$
\begin{aligned}
E\psi_l &= +\Delta_{l_{\text{eff}}}\psi_l + \Omega_{\text{eff}}\psi_k \\
E\psi_k &= -\Delta_{k_{\text{eff}}}\psi_k + \Omega_{\text{eff}}\psi_l
\end{aligned}
\tag{4.13}
$$

Which give us the effective Hamiltonian for the specific N-wave mixing crossing:

$$H_N = \frac{1}{2}\begin{pmatrix} -\Delta_{\text{eff}} & \Omega_{\text{eff}} \\ \Omega_{\text{eff}} & \Delta_{\text{eff}} \end{pmatrix} \tag{4.14}$$

See Appendix C for an example of this process for 6 wave mixing.

An N-wave mixing coupling will be resonant when the detuning for that level, $\Delta_{\text{eff}} = 0$, with a strength given by Ω_{eff}. The terms for Δ's and Ω_{eff} are calculated using computing software and are in general neither simple nor informative in their full form so have been omitted. The terms include factor of E which should be recursively replaced with Ω_{eff}, in reality a single replacement is sufficient, with all further cases of E set to zero, see figure C.1 in appendix C. Table 4.1 gives the first order approximation in Ω^2 and Δ for different orders of wave mixing. These are plotted in Figure 4.7.

Lowest Order Approximations, (for $\Omega_1 = \Omega_2 = \Omega$)

	Δ_{eff}	Ω_{eff} (at $\Delta_{\text{eff}} = 0$)
4WM	$\delta - \Delta + \frac{2(-176\delta + 71\Delta)\Omega^2}{225\delta^2}$	$\frac{\Omega^3}{4\delta^2}$
6WM	$2\delta - \Delta + \frac{(-86\delta + 13\Delta)\Omega^2}{144\delta^2}$	$\frac{\Omega^5}{64\delta^4}$
8WM	$3\delta - \Delta + \frac{(-243\delta + 25\Delta)\Omega^2}{576\delta^2}$	$\frac{\Omega^7}{2304\delta^6}$
10WM	$4\delta - \Delta + \frac{(-524\delta + 41\Delta)\Omega^2}{1600\delta^2}$	$\frac{\Omega^9}{147456\delta^8}$
12WM	$5\delta - \Delta + \frac{(-965\delta + 61\Delta)\Omega^2}{3600\delta^2}$	$\frac{\Omega^{11}}{14745600\delta^{10}}$
14WM	$6\delta - \Delta + \frac{(-1602\delta + 85\Delta)\Omega^2}{7056\delta^2}$	$\frac{\Omega^{13}}{2123366400\delta^{12}}$
16WM	$7\delta - \Delta + \frac{(-2471\delta + 113\Delta)\Omega^2}{12544\delta^2}$	$\frac{\Omega^{15}}{416179814400\delta^{14}}$
18WM	$8\delta - \Delta + \frac{(-3608\delta + 145\Delta)\Omega^2}{20736\delta^2}$	$\frac{\Omega^{17}}{1065420324864 00\delta^{16}}$
20WM	$9\delta - \Delta + \frac{(-5049\delta + 181\Delta)\Omega^2}{32400\delta^2}$	$\frac{\Omega^{19}}{345196185255593600\delta^{18}}$
22WM	$10\delta - \Delta + \frac{(-6830\delta + 221\Delta)\Omega^2}{48400\delta^2}$	
24WM	$11\delta - \Delta + \frac{(-8987\delta + 265\Delta)\Omega^2}{69696\delta^2}$	
26WM	$12\delta - \Delta + \frac{(-11556\delta + 313\Delta)\Omega^2}{97344\delta^2}$	
28WM	$13\delta - \Delta + \frac{(-14573\delta + 365\Delta)\Omega^2}{132496\delta^2}$	
30WM	$14\delta - \Delta + \frac{(-18074\delta + 421\Delta)\Omega^2}{176400\delta^2}$	

Table 4.1 Approximate solutions plotted in figure 4.7. Ω_{eff} solutions became too complicated to compute beyond 20 wave mixing.

The solutions to Ω_{eff} could not be calculated directly beyond $N = 20$ using the above method, but the following relation can be seen to be true for $N = 4 \rightarrow 20$:

$$\Omega_{\text{eff}(N+2)} = \Omega_{\text{eff}(N)} \frac{\Omega^2}{N^2 \delta^2} \tag{4.15}$$

We can check the functions calculated for $\Delta_{\text{eff}} = 0$ against the numerical eigenvalues calculated directly from the extended matrix for validity. The value of Δ required to make $\Delta_{\text{eff}} = 0$ will be called $\Delta_{\text{resonance}}$ since it is the initial detuning Δ required to place the the level on NMW resonance. Figure 4.8 shows the eigenvalues of the
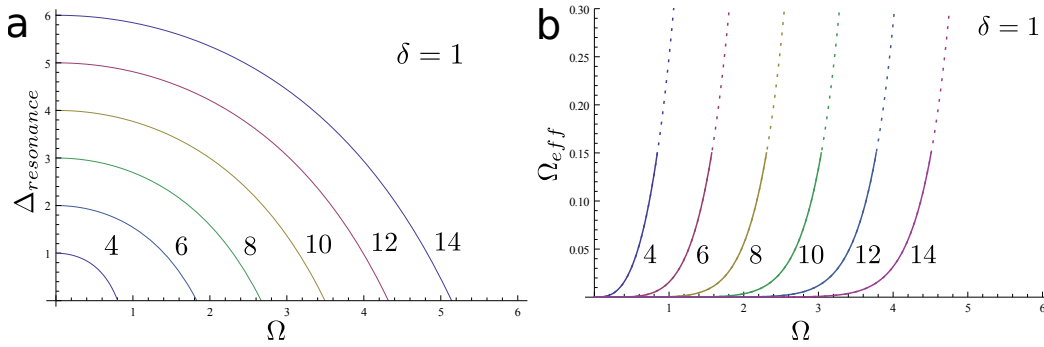
Fig. 4.7 a) Plot of $\Delta_{\text{eff}} = 0$ (resonance) for $N = 4$ through 14 for varying coupling power, aka Stark shift. This plot scales linearly with δ. b) Ω_{eff} on resonance.

extended matrix for different values of Ω. The calculated crossing values from table 4.1 are shown as vertical lines, we can see that the results approximately fit the numerical eigenvalue calculations except for the case of $\Delta < 1$. This effect can be seen again in figure 4.9 and is due to the limitation of using a second order function for the fit. Appendix C includes a discussion on the problems of creating a higher order function with our method.

As a general discussion point, we can consider the value of $\frac{(N-2)}{2}\delta - \Delta_{\text{resonance}}$ to be the AC Stark shift induced by the two lasers. This value is the amount through which the detuning needs to be altered from the naive bare state solutions for resonance of the N-wave mixing states to occur, which is the equivalent of saying the energy difference in the gap of the bare states and dressed states of the two level system. This calculation is not trivial for two applied lasers and will have different forms depending on whether the two lasers are the same intensity or very different intensities. Here we have assumed that they are equal for simplicity. Ultimately a numerical calculation of $\Delta_{\text{resonance}}$ is superior to any analytical results presented here.

Figure 4.9 compares the expected avoided crossing locations against the numerically measured minima that can be seen in figure 4.8 for a wider parameter space. Again we can see that the numerical eigenvalue results are close to our analytic function with the exception of when $\Delta_{\text{resonance}}$ is close to zero. Here there is a small deviation away from the fit for the low order wave mixing cases.

The above calculations were performed for the case $\Omega_1 = \Omega_2$. Calculating the terms for $\Omega_1 \neq \Omega_2$ results in an expression for Δ_{eff} which is neither simple nor insightful. A more useful approach is to understand that Δ_{eff} can be calculated from the Stark shift, of which there are many approximations depending on the assumptions that can be made, for example the approximation used in figure 3.22: $\Delta' \approx \sqrt{\Delta^2 + \Omega_1^2 + \Omega_2^2}$, valid for $\Delta >> \delta$.
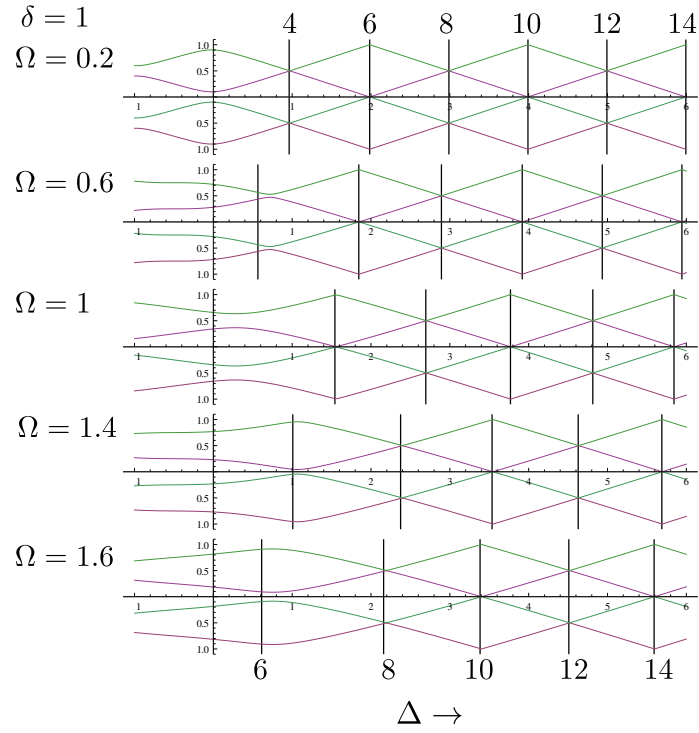
Fig. 4.8 N-wave mixing resonance crossings for 4 through 14 wave mixing and varying Ω's. Central four eigenvalues plotted for each case. Vertical black lines are the approximate solutions presented in table 4.1.
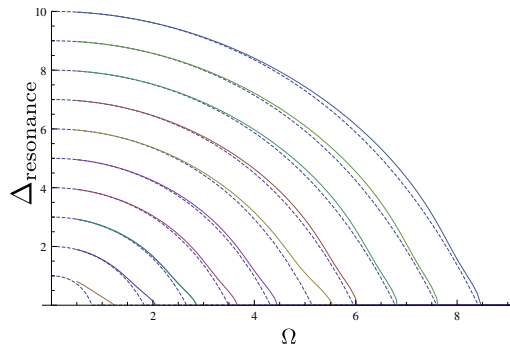
Fig. 4.9 Comparison between the resonance conditions given in table 4.1 (dotted) and the numerically calculated eigenvalue minimums of the extended Hamiltonian for wave mixing order 4 through 22. An extension from figure 4.8.

The result for the lowest orders of Ω_{eff} when $\Omega_1 \neq \Omega_2$ is however a simple result and compatible the relation given in equation (4.15). We have found that we can express the general coupling strength of an N-level wave mixing transition as:

$$\Omega_{\text{eff}(N)} = \frac{\Omega_1^{\frac{N}{2}} \Omega_2^{\frac{N}{2}-1}}{(2\delta)^{N-2} \left(\left(\frac{N-2}{2}\right)!\right)^2} \tag{4.16}$$

Where Ω_1 is closer to resonance with the bare state than Ω_2. This is of course only valid if we assume that the relation continues beyond the orders which are calculable with this approach.

This formula can be considered to be a specific case of the result for adiabatic elimination in higher level systems with any value Ω's and Δ's. We have two "end levels" and multiple in between levels which are all detuned from resonance such that we can remove then using adiabatic elimination. The coupling strength in the limit of small Ω's is simply $\frac{\prod^i \Omega_i}{\prod^i (2\Delta_i)}$. While the analytical results for large Ω's are opaque. A combination of intuition and numerical analysis has suggested that the coupling constant should actually be given by $\frac{\prod^i \Omega_i}{\prod^i (2\Delta_i')}$ where the Δ_i' are the detunings of each level from resonance after the Stark shift due to the applied strong coupling is accounted for. Normally this would be a complicated function to calculate, dependent on every other Δ and Ω. However, in the case for N-wave mixing this is simple, because each level, by definition, has to be at set intervals of δ from resonance with the N-wave mixing field at the point of resonance, which is the point at which we observe its effects. At this time the Δ primes can just be written down independently of the detuning of the original two level system, entirely in terms of δ and N. This leads exactly to the form of equation (4.16). Currently this relation is purely conjecture and has not been proven. We attribute this to the potentially surprising result that even with extremely strong Ω's, equation (4.16) does not appear to require any additional higher order terms to accurately predict coupling strengths, as is demonstrated later in figure 4.13.

4.4   Modelling N-wave mixing transfer

We test the accuracy of our model by comparing our results with numerical simulations of the original two level system. In a numerical model we are free to vary the system parameters as necessary to isolate the single N-wave mixing transfer in which we are interested.

To isolate single N-wave mixing transfers we consider a system coupled to two monochromatic sources of constant intensity, close to resonance with an N-wave mixing mode such that $\Delta = \Delta_{\text{res}} - \frac{\delta}{2}$. The energy splitting between the atom levels is then increased linearly over time until it reaches $\Delta = \Delta_{\text{res}} + \frac{\delta}{2}$. This approach ensures the system will cross the N-wave mixing mode in a controlled way, keeping all of the terms in the Landau-Zener formula constant throughout the transition minimising the effects from inaccuracies in the analytical approximations for Δ, Ω and δ. It should be noted that, while changing the splitting does actually change the effective laser coupling, it does so in a way that is easily accounted for, since we are only interested in the coupling strength at the point of the crossing itself, which by definition is when $\Delta_{\text{eff}} = 0$, fixing the detuning in Ω_{eff} and therefore fixing Ω_{eff}.
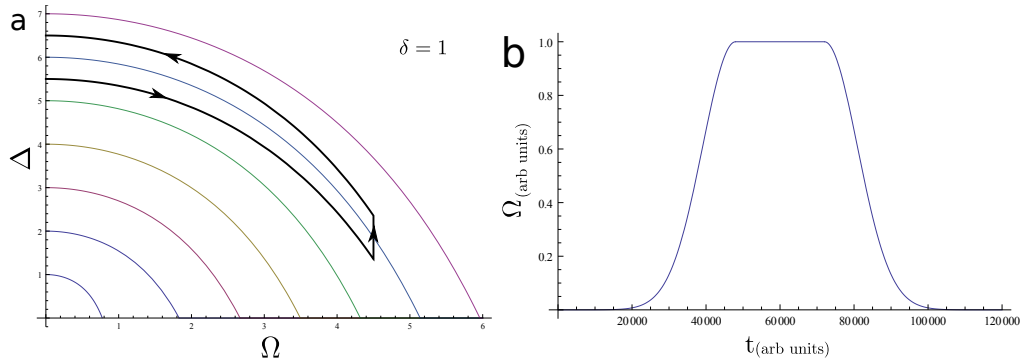

Fig. 4.10 a.) Path traversed during the simulation. b.) Ω intensity during a typical simulation, simulations below use this intensity curve shape rescaled with different maximum intensities Ω_{max} and total times T.

The whole process must be performed adiabatically, the numerical setup, shown in Fig 4.10 has an adiabatic rise in Ω to initialise the system, followed by a flat monochromatic period of Ω where the crossing occurs which is described above. This is then followed by an adiabatic removal of the lasers to reach a steady value for the transferred population. The detuning is swept during the first and last stages to ensure that there are no N-wave mixing modes crossed during the rise and fall of Ω, as shown in fig 4.10. During the central stage where the crossing occurs, Δ is swept linearly. This is then be compared to the theoretical values calculated previously.

The population of one of the bare states during a typical transition is shown in figure 4.11. State mixing increases as Ω is adiabatically increased. During the crossing the population rotates by an angle of up to π while also oscillating because of the two interfering frequencies applied, as Ω is adiabatically decreased the populations in the bare states stabilise and the fidelity of the transfer can be determined.
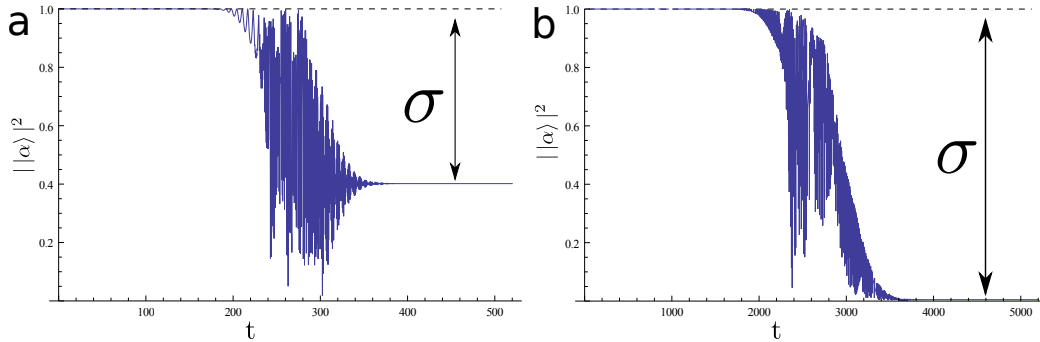

Fig. 4.11 Bare state population during typical simulations, showing a low fidelity (σ) and high fidelity transfer. Examples are for 20wave mixing, $\Omega = 6.5, \delta = 1$ and 18wave mixing, $\Omega = 6, \delta = 1$ respectively

Despite the large oscillations the population still closely obeys the Landau-Zener formula given in (2.25), confirming that the adiabatic condition for the crossing is unaffected. For 4.11a $\Omega_{\text{eff}} = \frac{6.5^{19}}{2^{18}(9!)^2}$, $dE/dt = 0.01$ and for 4.11b: $\Omega_{\text{eff}} = \frac{6^{17}}{2^{16}(8!)^2}$, $dE/dt = 0.001$ leading to expected population transfer of $e^{\frac{-\pi\Omega_{\text{eff}}^2}{2dE/dt}}$ of 0.34 and 10^-19 (which is within numerical accuracy of zero) respectively. Figure 4.12 shows the fidelity of transfer for three different sweep rates dE/dt and varying Ω compared with the expected fidelities from combining our results with the Landau-Zener formula, confirming the formulas presented in table 4.1.

From the results in figure 4.12 we can then calculate Ω_{eff} for each mixing order. These are shown in 4.13. There is a clear maximum value of Ω_{eff} which is the same for every mixing order. This makes sense geometrically since there δ limits how wide any avoided crossing can be, however this limit is lower than would be naively expected. Modifying the path to account for the bump in Δ_{eff} seen in figure 4.9 and generally being more careful may increase the

We have examined the N-wave mixing effects in a very controlled way to isolate the properties of the crossings to compare the analytic solutions with numerical data, and in doing so confirmed the validity of the results in table 4.1.
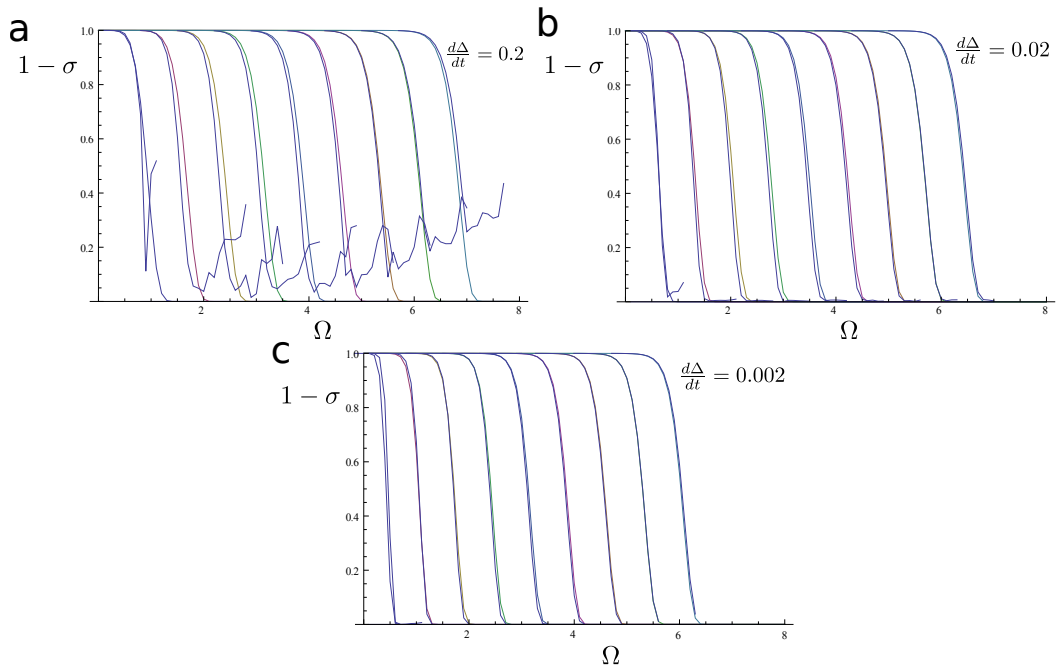
Fig. 4.12 Fidelity of an N-wave mixing-ARP transition and its dependence on Ω for N from 4 through to 20. The fit assumes that the Landau-Zener formula holds exactly for the effective coupling strength given in table 4.1.
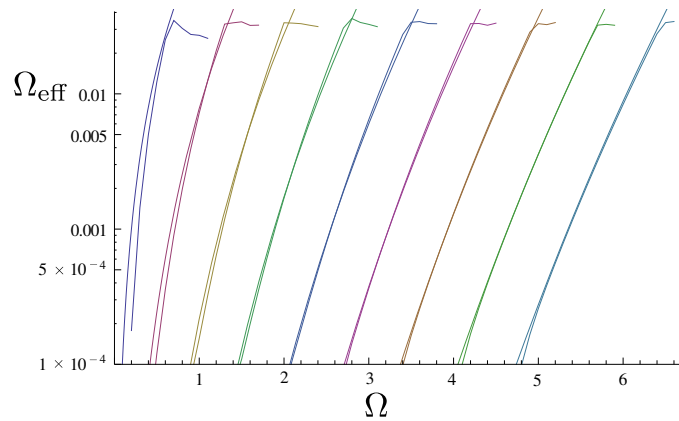
Fig. 4.13 Effective N-wave mixing coupling strength dependence on Ω for 4 through to 20 wave mixing, for varying Ω

4.5 Modelling disruptive N-wave mixing effects

In general the N-wave mixing effects we are considering are neither intentional nor desired, involving multiple crossings with each transferring small amounts of population in an uncontrolled manner.

We now consider the case with the path shown in figure 4.14, in which a pair of strong Gaussian-enveloped monochromatic pulses are coupled to a two level system. The Gaussian pulse generates a time dependent Stark shift, which, if the pulses are sufficiently strong, will cause crossings to occur with one or more N-wave mixing virtual levels. Every crossing will transfer an amount of population between the levels which we can calculate using Table 4.1.
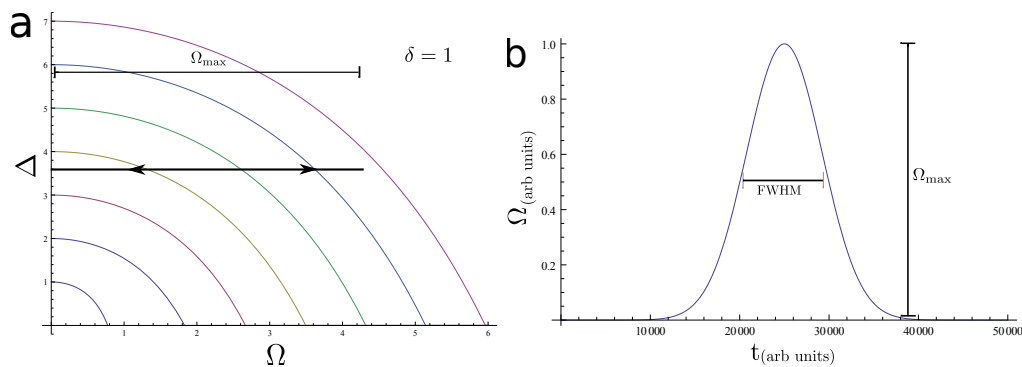
Fig. 4.14 a.) Example path traversed during the simulation b.) Ω intensity during the simulation, given by an adiabatic rise to height Ω_{max}, a period of constant Ω, followed by an adiabatic removal of Ω. The Purpose of this path is to drive the system adiabatically with zero crossings during periods of changing Ω and then driving the system with constant Ω and varying Δ across exactly one avoided crossing. Following simulations run with different total times T and strengths Ω_{max}, which scale with the shape of b.

We first set up a simple two level system without wave mixing to investigate the population transfer that occurs when two Landau-Zener crossings occur with a Gaussian shaped coupling term and Gaussian shaped eigenvalues. We then compare these results to the actual population transfer that occurs during N-wave mixing simulations.

4.5.1   Geometric Phase

To calculate the population transfer for the path taken in figure 4.14 we must first consider the effects of multiple ARP crossings. To do this we now introduce a two

level model with similar dynamics as a pair of N-wave mixing crossings. Within this example we set the detuning Δ and off-diagonal coupling Ω as follows:

$$\Delta = 1.5 - e^{-\frac{20\left(t-\frac{T}{2}\right)^2}{T^2}}\left(1 + \frac{\Delta_k}{1000}\right)$$

$$\Omega = e^{-\frac{20\left(t-\frac{T}{2}\right)^2}{T^2}}\left(1 + \frac{\Delta_k}{1000}\right)\frac{1}{2}\Omega_{\text{max}}$$

(4.17)

Where T is the time elapsed in the simulation, Δ_k determines how far the states cross over and Ω_{max} is a constant. We can consider this system in the frame where one bare state set constant, representing the fixed N-wave mixing virtual state and the second state's energy following a Gaussian profile, representing the real state being driven by a strong Stark shift which punches through the steady N-wave mixing state. The coupling between the states is given by the same Gaussian, and importantly will have the same value at the crossing points independent of Δ_k, as would be expected during an N-wave mixing transition.
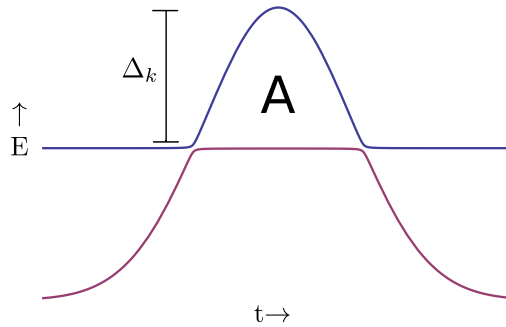
Fig. 4.15 Eigenvalues the two level system with equations (4.17), set to simulate a single N-wave mixing crossing pair with a path as described in figure 4.14. A is the area between the two eigenvalues, Δ_k determines how far the states cross over

Simulations run with equations (4.17) undergo two transitions, as the base state energies cross twice. Although we know the angle rotated on the Bloch sphere we do not currently know the direction. Therefore the two transfers can either be constructive, destructive or somewhere in between. Two typical results are shown in figure 4.16, one constructive and one destructive.

We treat the transfer as a rotation by θ determined by the Landau-Zener formula at an angle ϕ determined by the phases of the system. The maximum transfer is therefore given by the angle 2θ and the minimum rotation angle is zero, if both transition are the

Fig. 4.16 The population during two typical simulations for $T = 1000$, $\Omega_{\max} = 1/300$ and $\Delta_k = 953$ and 1000 respectively. Each has two transfer points. Δ_k is chosen in the first simulation such that the transfers are constructive and in the second simulation destructive, resulting in no overall change in the state.
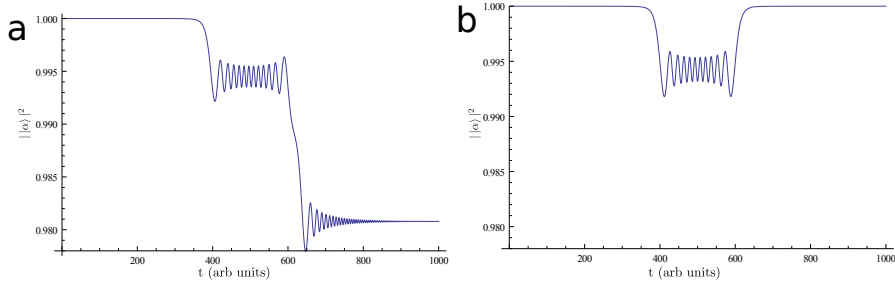
same fidelity. Only the relative values of ϕ between the two crossings are important as this completely determines the constructive/destructive nature of the transitions. The relative angle between the two transitions is determined by the area A shown in figure 4.15 and is known as the geometric phase [9]. For small angles the final population transfer is given by.

$$||\psi_{1\text{final}}\rangle|^2 = \tfrac{1}{2}\left(1 - \cos\left(2\arccos\left(1 - 2\sigma\right)\right)\right)\tfrac{1}{2}(\sin(A) + 1), \tag{4.18}$$

which takes the maximum possible transfer from two consecutive ARP transfers multiplied by a function of the geometric phase factor A which accounts for whether the transfers were constructive or destructive. This is a simplistic method that does not account for the dynamics of the first peak, giving an infinite answer as the levels first touch due to the unrealistic infinitely flat crossing angle. A complete approach is given in [69], the addition is not necessary for the analysis performed later and has not been included.

Figure 4.17 shows an initial rise in the population transfer followed by an oscillatory and decreasing population transfer as Δ_k is increased. The initial increase is due to the two levels starting to cross over and having infinite gradient, our treatment fails because it is not relevant to consider the transfer as the product of two independent avoided crossings at this point, a complete derivation of a similar setup is done in section 2 in [69] which also fits correctly for $A \approx 0$. For the purposes in this thesis the result in equation (4.18) will be sufficient as the majority of the graph is well represented by the fit. The oscillations are due to the geometric phase accumulated between the two crossing points and the slow decrease in transfer is due to Δ_t increasing in line with the shape of the stretched Gaussian, Ω at the point of crossing remains constant throughout.
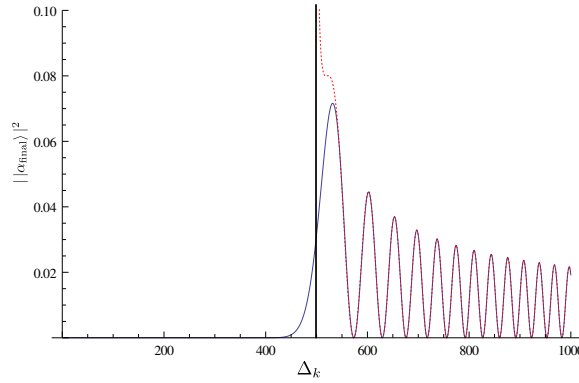
Fig. 4.17 The final populations for simulations run with equations (4.17) (blue, solid) fit given by equation (4.18) (red, dotted). Black line corresponds to the value of Δ_k when the bare states touch just once.

4.5.2 N-wave mixing disruptive transfer

We now use the results from the section 4.5.1 to calculate the population transfer that occurs in systems with strong Gaussian pulses inducing multiple Landau-Zener crossings with N-wave mixing virtual levels. The parameter path for this is shown in 4.14, which when considered through the extended Hamiltonian results in the eigenvalue diagram in figure 4.18.
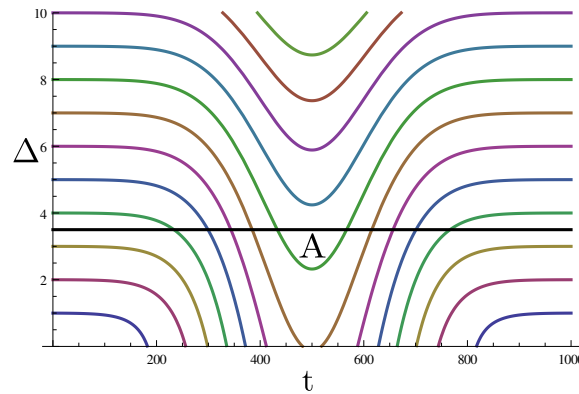
Fig. 4.18 Coloured lines: resonance conditions given from table 4.1 for $\delta = 1$, $\Omega_{max} = 6$. Black line included for $\Delta = 3.5$ reference, giving the Landau-Zener crossing points between the N-wave mixing virtual levels.

We use the resonance conditions from table 4.1 to calculate when the system with bare state detuning $\Delta = 3.5$ will be on resonance with the N-wave mixing virtual levels and undergo a Landau-Zener crossing. The Stark shift modified resonance conditions are shown in figure 4.18 with the black line for $\Delta = 3.5$ showing both when resonances are expected to occur and the rate of the energy sweep at each crossing. This can be

used to determine the location and fidelity of each Landau-Zener crossing. The area A gives the relative phase between the highest two crossings.
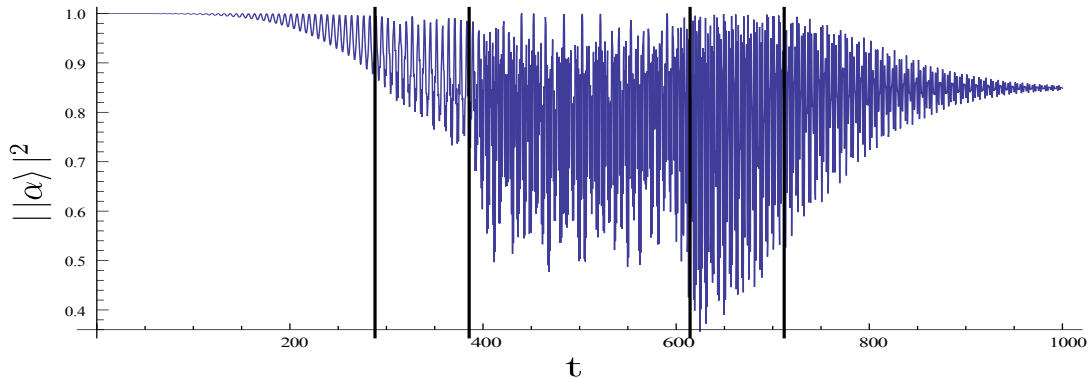
Fig. 4.19 Bare state population during a typical simulation. $\Delta = 2.5$, $\delta = 1$, $\Omega_{\mathrm{max}} = 3.1$ Black lines are the crossing points for 8wave mixing (outer pair) and 10 wave mixing (inner pair). We can see after the first 8 wave mixing crossing the Rabi oscillations no longer reach back to 1, indicating a small population transfer, the population transfer after each 10 wave mixing crossing is indicated by a more pronounced step. The total population transferred during this simulation is roughly 0.15.

The maximum possible transfer from a set of ARP population transfers can be calculated by summing up the total angle rotated by each transition, assuming that they act constructively:

$$\sigma_{\mathrm{max}} = \frac{1}{2}\left(1 - \cos\left(\sum_{j=1}^{n}\arccos\left(1 - 2\sigma_j\right)\right)\right), \qquad (4.19)$$

unless the sum reaches more than a full π rotation of the Bloch sphere, in which case the maximum is simply 1. This equation is generated with the same method as the first part of equation (4.18) and sums up the angle each ARP transfer rotates on the Bloch sphere and returns this value in terms of the total population transfer This equation is used to fit the to the simulation data shown in 4.20 and should provide an upper bound to the results. We can see from 4.20 that the actual upper bound is a small deviation from this result, and we believe is due to the deviations between the numerical and analytical results for $\Delta_{\mathrm{resonance}}$ shown in figure 4.9.

The geometric phase accumulated between each transition determines whether the pairs of transfers will be constructive or destructive, and is calculated in the same method as section 4.5.1. A full treatment should take into account the interferences between each pair of transitions. Here we are primarily interested in validating our model, so we have only included the highest order as this dominates the transfer.
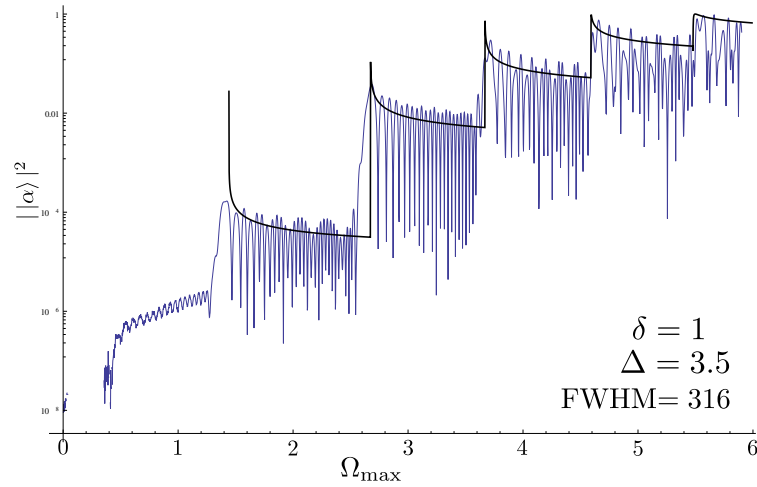
Fig. 4.20 Blue: data, Black: fit. Population transfer for simulations with a pair of Gaussian pulses as described in 4.14 for various $\Omega_{\max}$, clearly showing steps due to each order of wavemixing crossed and oscillations to the geometric phase accumulated between transitions. The five steps correspond to $10 \to 18$wave mixing.

Accounting for the phases between pairs of transfers from different orders of wave mixing is not trivial.

$$\sigma = \sigma_{\max}\tfrac{1}{2}(\sin(A) + 1), \tag{4.20}$$

where A, shown in figure 4.18, is the area enclosed between the highest order crossing with the detuning energy Δ, which for the example in the figure is the 16 wave mixing crossing with $\Delta = 3.5$.
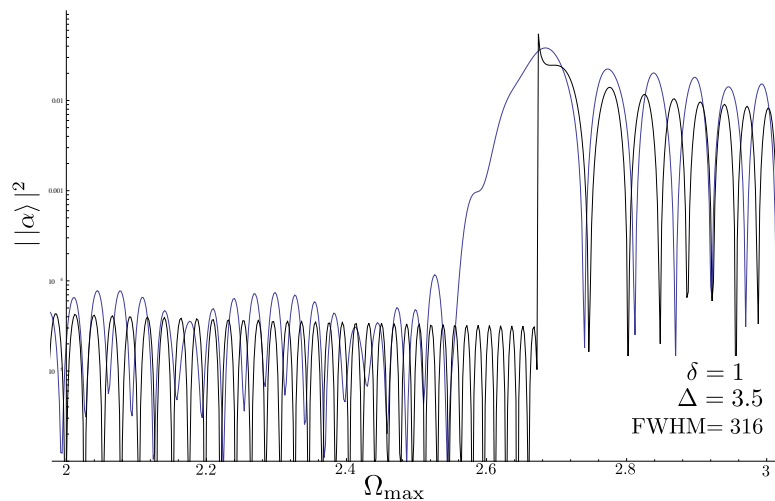
Fig. 4.21 Blue: data, Black: fit. A subsection of data from figure 4.20 with a fitting curve defined by equation (4.20)

Figure 4.21 shows the data and fit for an N-wave mixing transition. While the fit in the figure qualitatively matches the numerical simulations well the oscillation width quickly deviates from the numerical values, this is due to the imperfect match between the calculated and actual values for $\Delta_{\text{resonance}}$ which were shown in figure 4.9.

4.6   Smooth curve

The transfer probability for the situations with a large number of steps or low Ω resolution is better represented by a smooth function which is continuous in N ignoring the discreteness of the steps above. To calculate this we require the functions $\Omega_{\text{eff}}(N)$ and $\Delta_{\text{resonance}}(N)$ for $N \in \mathbb{R}$. These functions were given in table 4.1 for integer N only. We can directly extrapolate $\Omega_{\text{eff}}(N)$ from equation (4.16) to give:

$$\Omega_{\text{eff}(n)} = \frac{\Omega^{2n+1}}{(2\delta)^{2n}\Gamma\left(n+1\right)^2} \tag{4.21}$$

Where Γ is the gamma function, the continuous variable extension to the factorial. There is however no exact relation for $\Delta_{\text{resonance}}(N)$ (the value of Δ required to make $\Delta_{\text{eff}} = 0$). Instead we have approximated $\Delta_{\text{resonance}}(N)$ by noting that the dependence on N scales approximately linearly with δ. We (arbitrarily) pick the 28 wave mixing $\Delta_{\text{resonance}}$ equation from 4.1 to derive:

$$\Delta(\text{n}) = \frac{-1121\text{n}\Omega^2\delta + 784\text{n}^3\delta^3}{-365\Omega^2 + 784\text{n}^2\delta^2} \tag{4.22}$$

Where n is the number of the equation in table 4.1 and $N = 2n+2$. Given a known Δ, δ and Ω a (generally non-integer) value for n can be found from equation (4.22). We can then calculate a smooth approximate solution for the total population transfer, ignoring the discontinuous steps by generalising equation (4.18):

$$\sigma_{\text{total}} = 1/2\left(1-\cos\left(\int\arccos\left(\sigma(n)\right)\left|\frac{dn}{dt}\right|dt\right)\right) \tag{4.23}$$

Where $\sigma(n)$ is the population transfer probability at the the point n, given by:

$$\sigma(n) = e^{\frac{\Omega_{\text{eff}n}}{\left|\frac{d\Delta}{dt}\right|}\frac{\pi}{2}} = e^{\frac{\left(\frac{\Omega^{2n+1}}{(2\delta)^{2n}\Gamma(n+1)^2}\right)}{\left|\frac{d\Delta}{d\Omega}\frac{d\Omega}{dt}\right|}\frac{\pi}{2}} \tag{4.24}$$
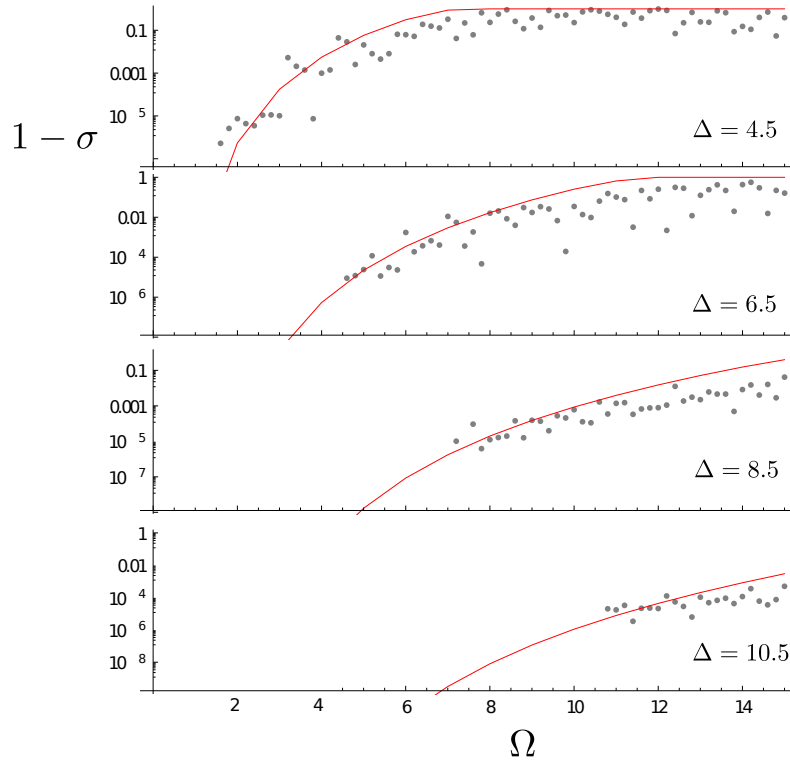
Fig. 4.22 Simulation data (points) and smooth fit from equation (4.23) (line) for the path given in figure 4.14. Steps in the data are partially visible, simulation precision is 10^{-6}, limiting the comparison between fit and data to transfer probabilities $\gtrsim 10^{-6}$.

and

$$\frac{d\Delta}{d\Omega} = \frac{1185408\mathrm{n}^3\Omega\delta^3}{\left(365\Omega^2 - 784\mathrm{n}^2\delta^2\right)^2} \tag{4.25}$$

can be derived from equation (4.22).

Figure 4.22 shows some example comparisons between the simulation data and the fit given in equation (4.23). The fit assumes that all transfers are constructive and therefore can be considered to be a maximum transfer function. We can see that while the fit should be an upper bound to the results, some lie above the fit. As was the case in figure 4.21 this is due to inaccuracies in the analytically calculated $\Delta_{\text{resonance}}$ which leads to an underestimate in the transfer probability.

We calculate the smooth transfer function for a wider parameter space with $\delta = 1$ and Gaussian FWHM= 1000. We then generalised the curves' parameters based on

their scaling with δ and the FWHM. The contour plot for this data is given in figure 4.23. The contour lines f_i correspond to lines of a (maximum) transfer probability:

$$\sigma_{\text{total}} = 10^{-19+i} \times \text{FWHM} \times \delta. \tag{4.26}$$

This plot therefore allows a calculation of the expected transfer for a completely general set of parameters δ, Δ, Ω and FWHM. Assuming that the two laser couplings applied are of the same strength, $\Omega_1 = \Omega_2$. This plot can therefore be used to determine whether an experiment with intense Gaussian pulses will suffer from losses due to wave mixing which are large enough disrupt the result.

For example if we run an experiment with $\Delta = 5\text{meV}$, $\delta = 0.6\text{meV}$, $\Omega = 6\text{meV}$ and a $FWHM = 10,000$ in code units, $= 650\text{ns}$, we get the factors $\frac{\Delta}{\delta} = 8.3$ and $\frac{\Omega}{\delta} = 10$, which corresponds to the line f_{13} in figure 4.23. From equation (4.26) we can calculate the transfer due to wavemixing to be $\sigma_{\text{total}} = 10^{-19+13} \times 10,000 \times 0.6 = 0.006$, which means that there should be up to 0.6% population transfer during the process due. If
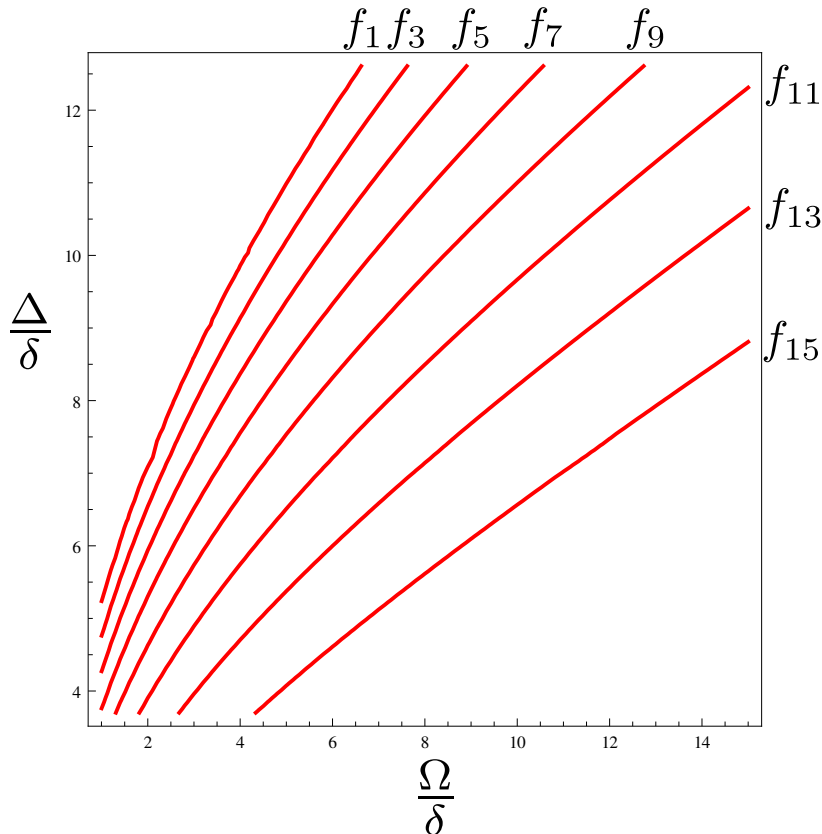

Fig. 4.23 Contour plot for fit f_i corresponds to a total transfer $\sigma_{\text{total}} = 10^{-19+i} \times$ FWHM $\times \delta$ for $\sigma_{\text{total}} > 1$. This plot can be used to infer the approximate transfer probability for any Δ, δ, $FWHM$ and Ω (for $\Omega_1 = \Omega_2$).

however Ω is increased to 8meV, corresponding to line f_{15} in figure 4.23 the population transfer will be 100 times higher, resulting in up to 60% transfer during the process while if an Ω of 4meV (f_{10}) was used the transfer due to wavemixing would only be around 6×10^{-7}. Demonstrating the sensitivity of wavemixing transfer where relatively small variations in the parameters can result in orders of magnitude difference in the total population transfer.

4.7   N-wave mixing SCRAP
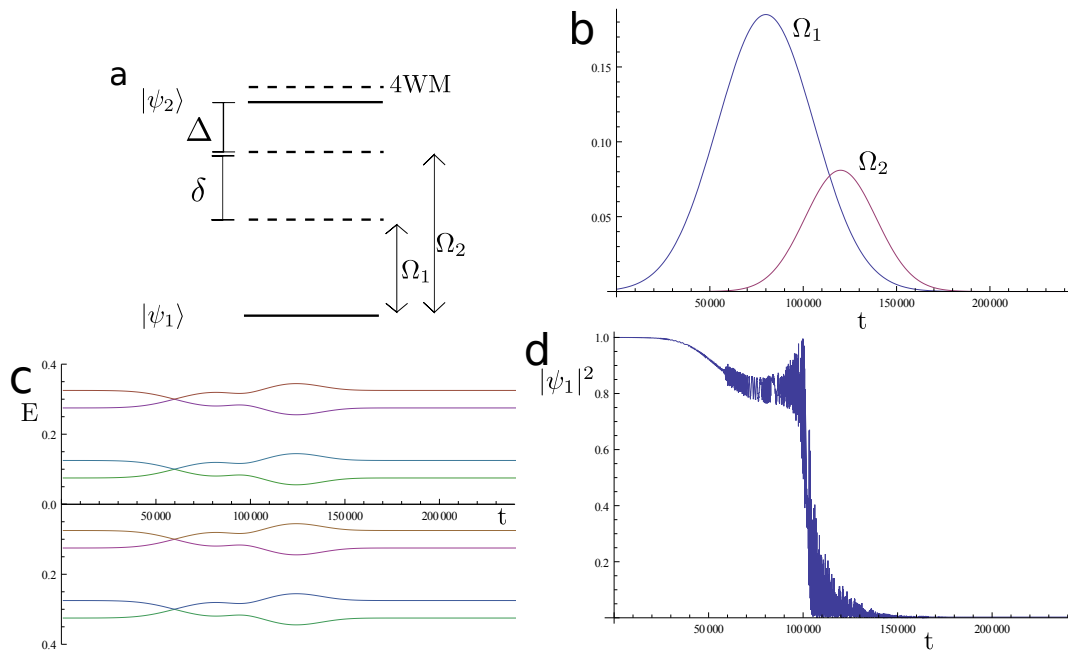
Fig. 4.24 Four wave mixing SCRAP protocol. a.) Energy level diagram, energy levels given by solid line, resonances given by dotted lines including the 4 wave mixing virtual detuned slightly above resonance. $\Delta = 0.15$, $\delta = 0.2$. b.) Temporal profile of Ω_1 and Ω_2. c.) The eigenvalues of the extended Hamiltonian, each pair of levels corresponds to $|\psi_1\rangle$ and $|\psi_2\rangle$ and repeated infinitely. Both pulses generate a significant amount of Stark shift, the non-avoided crossing is clear at t=60,000 while the avoided crossing at around t=110,000 is strongly separated by the combination of the pulses. d.) the population during the process showing a large proportion of state mixing before and a strong transfer at the second level crossing. Also not small jump at t=60,000 due to the first crossing. A thinner or more delayed Ω_2 would prevent this.

So far we have only considered the disruptive effects of wavemixing. However, given the results from the previous section we know that the N-wave mixing-SCRAP transition is a coherent process and can potentially be used for controlled population
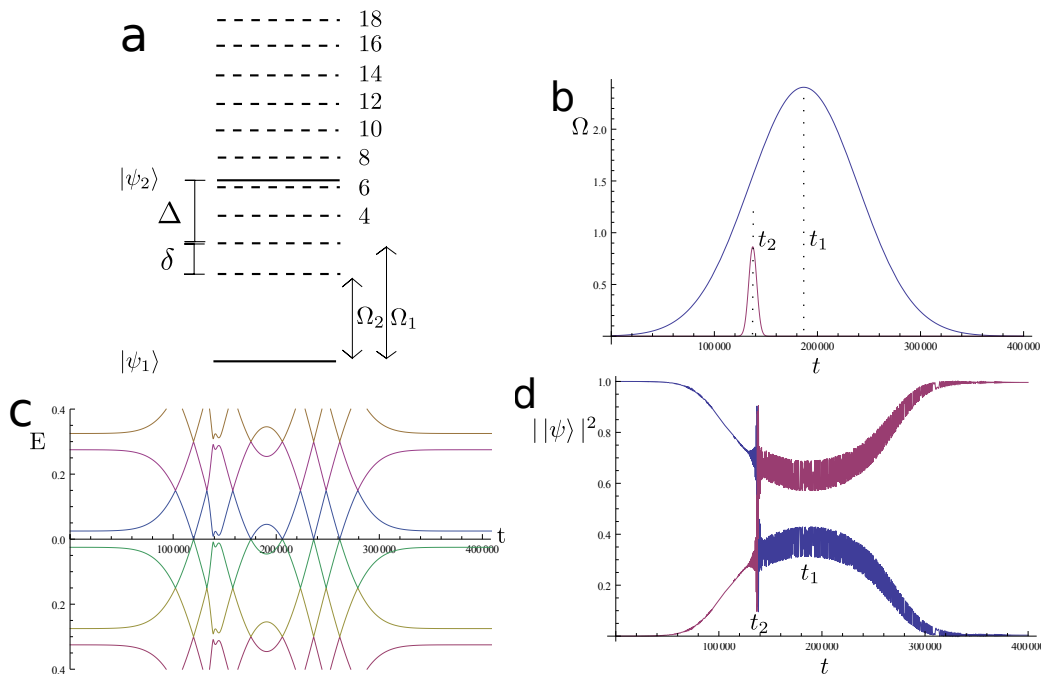
Fig. 4.25 14 wave mixing-SCRAP example a.) wave mixing levels up to 18 shown $\Delta = 0.65$, $\delta = 0.3$. b.) Two pulses applied to the system Ω_1: long pulse centred at t_1 and Ω_2 short pulse centred at t_2. c.) Eigenvalues of the extended matrix showing a large Stark shift crossing many levels caused by Ω_1. The weaker pulse Ω_2 is chosen to intersect at the 14 wave mixing crossing causing an avoided crossing. All other crossings are benign. d.) The populations of each level during the transition. The large state mixing population is due to Ω_1 while the sharp crossing t_2 is the SCRAP crossing.

transfer in quantum information protocols. SCRAP is an ARP transition and can therefore only be used robustly for π rotations. One example for a controlled N-wave mixing-SCRAP transition was provided in figure 4.10 which isolated a single transition in a numerical simulation using a complicated and carefully tuned path. Performing a similar path in an actual experiment would be impractical.

The simplest, most practical scheme that we have come up with for controlled population transfer is directly analogous to the Stark Chirped Rapid Adiabatic Passage (SCRAP) transfer 4.1. SCRAP involves two lasers, one strong laser far detuned from resonance that induces a Stark shift in the energy splitting of the system, and one weak laser that is detuned slightly above resonance with the bare state splitting of the system such that as the Stark shift is increased the system passes through resonance with the weak laser, inducing population transfer.

Fig. 4.26 The fidelity of the N-wave mixing-SCRAP transition for the parameters given in figure 4.25 with a varying time delay for the second pulse t_2. The position of the second pulse determines which N-wave mixing transition becomes avoided, creating SCRAP transfer. Each drop is due to wave mixing and is labelled by it's order.

For small orders of wave mixing our N-wave mixing-SCRAP protocol uses two strong, far detuned lasers to induce the Stark shift in the system and simultaneously generate a weak N-wave mixing field on re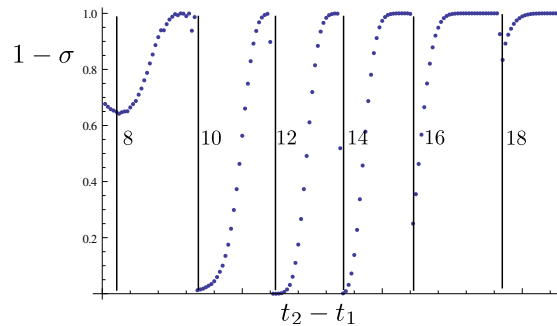sonance to cause the population transfer. An example N-wave mixing-SCRAP crossing is shown in figure 4.24 for a 4 wave mixing case. In general the first eigenvalue crossing should transfer an insignificant amount of population and the second should have near complete transfer. This example was chosen to show a small transfer at the first crossing, which can be seen from the oscillations that begin at that point. A temporally thinner second pulse would eliminate the first, unwanted population transfer

For high wave mixing orders methods including two pulses of roughly equal length will not work as the pulses will generally induce several crossings in a similarly messy situation that generated the steps in the previous section. For higher orders of wave mixing we found that we require one very strong and long pulse to provide the majority of the Stark shift and one weaker, but still strong short pulse to generate the wave mixing transition to ensure only a single avoided crossing occurred and to give the ability to control which crossing was used. The short pulse must be shorter than the time between subsequent crossings. Short enough to only create a single avoided crossing, while wide enough to be adiabatic. An example for 14 wave mixing is shown in figure 4.25 but in theory any level wave mixing is possible with suitably high intensity fields and appropriate detunings.

For transfer with high wave mixing order the timing of the short pulse is important to determine the order of wave mixing that is used for transfer. Figure 4.26 shows the final transfer for the parameters used in figure 4.25 but for different values of t_2. Figure 4.25d shows the population during an optimal 14 wave mixing example, but

we can see that varying the delay between the pulses allows for anything from 8 wave mixing to 18 wave mixing transfer to be generated for the same Stark pulse. For wave mixing orders that are too small the strength of the Stark laser at the point of crossing is not sufficient to generate complete population transfer since the crossing occurs at the tail of the Gaussian. For wave mixing orders that are too high the pulses are not of sufficient strength to generate complete population transfer for this example. For this example we created high fidelity crossings for wave mixing 10 through 14.

This section was provided to indicate the possibilities of the N-wave mixing-SCRAP transfer protocol. We have not begun to analyse the transfer probabilities here, however we would expect equation (4.16) to fit the data regarding the strength of transfer.

4.8 Wave Mixing Conclusions

We have identified the source of loss in figure 3.22 and found a general solution to the strength of large order wave mixing couplings. This was done by generating an infinite Hamiltonian that was still an exact solution to the two level wave mixing problem and then approximating the Raman strength of distant levels within the extended Hamiltonian, creating a table of coupling strengths and resonance conditions calculated up to 20 wave mixing, and a relation between the coupling strengths that is expected but not proven to continue to any wave mixing order.

The solutions were tested against an idealised numerical model of wave mixing transfer and then a two level equivalent to the unwanted transfer problem originally found in the previous chapter. The solution broadly fits the numerical simulations for both the strength and location of the resonances. We have also shown that geometric phases can be generated from the relative energies of the virtual levels. We have found that the calculations for the resonance conditions are not good enough to provide a close quantitative fit for the geometric phase accumulated between crossings, calculation of the resonance conditions numerically from the eigenvalues of the extended matrix is expected to improve this fit significantly. We have not found a general solution to the resonance conditions for $\Omega_1 \neq \Omega_2$, this is best approximated on a case by case basis.

We have provided a general smooth approximation to the problem of unwanted transfer for arbitrary δ, Δ, Ω and FWHM for the case of $\Omega_1 = \Omega_2$, this case is useful for setups with two lasers of the same intensity, or more commonly accounting for the effects of the counter rotating term for a single laser pulse. We provided a process which could be extended for cases $\Omega_1 \neq \Omega_2$ if an appropriate function for the Stark

shift is used in place of equation (4.22). This can be used to identify parameter areas where experiments with strong couplings should avoid to minimise wave mixing effects.

We go on to provide some examples of controlled wave mixing transfer which are based upon the SCRAP protocol, N-wave mixing-SCRAP. These methods could in principle be used to transfer population coherently in real systems using high orders of wave mixing, however due to the extreme sensitivity to all parameters involved (Ω's, Δ and δ) we feel it is unlikely to be a practical protocol. The only exception to this is if there is a problem in obtaining the required frequencies in the lab required for transfer. Because of the sensitivity to the parameters these transfer mechanisms could potentially be used to make precise measurements of the system and its optical couplings.

Chapter 5

Conclusions

5.1 Quantum Memory

We introduced a complete quantum memory algorithm capable of single photon storage and retrieval using an ensemble of self-assembled quantum dots, analysing in detail the initialisation protocol and π pulse transfer required for spin echo.

We introduced a novel initialisation protocol which is capable of initialising an ensemble of quantum dots with a large inhomogeneous broadening to a reasonable fidelity of around 97%, which we have found is limited by the decay rate Γ and the electron and hole zeeman splitting of the dots in the ensemble. We have shown that the maximum initialisation fidelity is independent of the inhomogeneous broadening of the ensemble. Increased inhomogeneous broadening linearly increases the time required to intialise the ensemble.

We found that the RCAP π pulse is the most appropriate protocol for performing a spin echo during photon storage. We calculated the amount of spontaneous decay during each RCAP transition and found that the fidelity losses due to spontaneous emission during the π pulse is within the limits provided by fault tolerant quantum computing. The fidelity of the π pulses is primarily limited to the time available to run the pulse and can be performed satisfactorily in under 100ns. We also found that the losses due to spontaneous emission are dependent on the direction of the frequency sweep that is taken.

We considered both the case of an in-plane geometry which only uses a single polarisation to couple to all four of the Voigt geometry transitions and could be realised with current fabrication techniques and an out-of-plane version which requires roughly 1000 layers of quantum dots to be stacked, which is beyond current fabrication abilities. We found that the initialisation process can be achieved for the in-plane case, if at a

reduced fidelity and π pulse transfer should also be achievable to a reasonable fidelity. The write and read processes however are not possible for the in-plane geometry, this rules out the creation of quantum memory using this geometry but could still lead to experimental studies which confirm initialisation and/or π rotation feasibility.

We gave a rough analysis of the signal fidelity and noise probability that would be expected from a typical memory. We found that the photon losses are within the thresholds for fault tolerant quantum computing. We have calculated the noise for an example ensemble, which can be used to calculate the noise output from the memory into the quantum computer after further study to determine the spread of the outgoing photon.

5.2   Quantum Memory Future Work

An analysis of the optimal size and shape of the control and signal field (and therefore the ensemble) will allow a fully calculation of the measured noise into the quantum computer, and will therefore answer the question of the viability of the memory. Several of the calculations surrounding the noise output that were used were speculative and intended only to provide a rough conclusion as to the memory viability. These assumptions should be revisited, particularly the optimised control pulse strengths for the write and read protocols that we used in calculations, since these had been considered in terms of photon retrieval efficiency only. A study with an optimisation that accounts for both the signal and noise generation during readout will be necessary for a complete analysis of the memory.

A study into the the in-plane selection rules for different quantum dots is necessary to determine whether one or two linear polarisations are accessible in all cases. If it is possible to manufacture ensembles in which transitions with both polarisations are accessible the results presented in this thesis from the full Voigt geometry will be applicable to an in-plane propagating photon, considerably increasing the feasibility of realising the QM.

We have found that the primary source of noise is the initialisation process, it may therefore be feasible to consider multimode storage where an individual dot can contribute to storing multiple spin waves, using angular multiplexing, for example [74].

5.3 Wave mixing

We identified the source of loss presented at the end of chapter 3 as N-wave mixing and found a novel solution to the problem through the use of an infinite Hamiltonian matrix, which allows a calculation of wave mixing to large orders. We then found approximate solutions to this matrix through adiabatic elimination at the parameter conditions relevant to population transfer and confirmed the results of the N-wave mixing strengths through numerical simulations for wave mixing orders between 4 and 20. We found a good agreement between theory and simulation for the strength of the transition and found a reasonable agreement between the theory and simulation for the detuning required for resonance, which is the equivalent to the Stark shift. This demonstrates the success of our extended Hamiltonian approach.

We used these solutions to calculate the (generally disruptive) population transfer via N-wave mixing for a pair of Gaussian pulses applied to the two level system and compared to numerical simulations, this included the geometric phases that are due to the multiple crossings which create oscillations in T and Ω in the total transfer probability. This research recreated a similar scenario to the one that generated the stepped plot 3.22 which is a general problem for experiments where intense couplings are applied.

The case for two Gaussian pulses causing N-wave mixing population transfer was concluded by calculating a smooth transfer function which ignores features such as the steps and geometric phases and focusses instead on the approximate population transfer. This result gives the transfer probability when two equal Gaussian pulses are applied for a wide range of parameters relevant to experiments with multiple intense adiabatic couplings.

We identified the possibility of a controlled and coherent transfer using N-wave mixing and the SCRAP protocol, N-wave mixing-SCRAP. We introduced two approaches to achieving N-wave mixing-SCRAP, one for low order N-wave mixing and one for higher order N-wave mixing and presented some preliminary results for each case which are sucessful for almost complete transfer. These protocols are very sensitive to both the detunings and strengths of the lasers, whilst there are no practical applications immediately obvious for these transfer protocols they may be of use for determining the properties of some systems because of this sensitivity.

5.3.1   Wave Mixing Future Work

The methods presented provide only an approximate solution to the eigenvalues of the extended Hamiltonian, an exact solution for the infinite tri-diagonal matrix may still be possible [40]. The results in equations (4.16) and (4.15) are compatible with the intuitive expectations of Raman coupling and adiabatic elimination extended to multiple level systems and fit simulations well despite being the lowest order approximation. We therefore suspect, but have been unable to prove, that this is the exact solution. An exact solution to the extended Hamiltonian should be able to confirm this result after further research.

The results for destructive transfer probability were limited to the case where two equal Gaussian pulses are applied to the system. The theory presented is easily extended to non Gaussian shaped pulses, however it is not trivial to extend it to two different strength pulses, as different parameter regimes call for different approximations to the Stark shift.

We presented two example methods of controlled N-wave mixing-SCRAP transfer used for coherent population transfer. A complete analysis of these transfer techniques could identify whether these protocols have any benefits over current population transfer protocols or whether it could be used to analyse the interaction between light pulses and atomic systems, given the sensitive dependence on several parameters.

The analysis was completed without once considering the emission spectrum of the system. The emission due to wave mixing will be a series of δ functions. The properties of the emission would be expected to be given by the emission between the relevant orders within the extended Hamiltonian.

References

[1] S. Ashhab, J. Johansson, A. Zagoskin, and Franco Nori. Two-level systems driven by large-amplitude fields. *Physical Review A*, 75(6):063414, June 2007. ISSN 1050-2947. doi: 10.1103/PhysRevA.75.063414. URL http://link.aps.org/doi/10.1103/PhysRevA.75.063414.

[2] Adriano Barenco, Charles Bennett, Richard Cleve, David DiVincenzo, Norman Margolus, Peter Shor, Tycho Sleator, John Smolin, and Harald Weinfurter. Elementary gates for quantum computation. *Physical Review A*, 52(5):3457–3467, November 1995. ISSN 1050-2947. doi: 10.1103/PhysRevA.52.3457. URL http://link.aps.org/doi/10.1103/PhysRevA.52.3457.

[3] Sean D. Barrett and Thomas M. Stace. Fault Tolerant Quantum Computation with Very High Threshold for Loss Errors. *Physical Review Letters*, 105(20): 200502, November 2010. ISSN 0031-9007. doi: 10.1103/PhysRevLett.105.200502. URL http://link.aps.org/doi/10.1103/PhysRevLett.105.200502.

[4] Sean D. Barrett and Thomas M. Stace. Fault Tolerant Quantum Computation with Very High Threshold for Loss Errors. *Physical Review Letters*, 105(20): 200502, November 2010. ISSN 0031-9007. doi: 10.1103/PhysRevLett.105.200502. URL http://link.aps.org/doi/10.1103/PhysRevLett.105.200502.

[5] Gerald Bastard. *wave mechanics applied to semiconductor hetrostructures*. Les Éditions de Physique, 1988. ISBN 0470217081.

[6] Charles Bennett and Gilles Brassard. Quantum Cryptography: Public key distribution and coin tossing, 1984. URL https://www.cs.ucsb.edu/~chong/290N-W06/BB84.pdf.

[7] C. Bentham, I. E. Itskevich, R. J. Coles, B. Royall, E. Clarke, J. O'Hara, N. Prtljaga, A. M. Fox, M. S. Skolnick, and L. R. Wilson. On-chip electrically controlled routing of photons from a single quantum dot. *Applied Physics Letters*, 106(22):221101, June 2015. ISSN 0003-6951. doi: 10.1063/1.4922041. URL http://scitation.aip.org/content/aip/journal/apl/106/22/10.1063/1.4922041.

[8] K. Bergmann, H. Theuer, and B. Shore. Coherent population transfer among quantum states of atoms and molecules. *Reviews of Modern Physics*, 70(3):1003–1025, July 1998. ISSN 0034-6861. doi: 10.1103/RevModPhys.70.1003. URL http://link.aps.org/doi/10.1103/RevModPhys.70.1003.

[9] M. V. Berry. Quantal Phase Factors Accompanying Adiabatic Changes. *Proceedings of the Royal Society A: Mathematical, Physical and Engineering Sciences*, 392 (1802):45–57, March 1984. ISSN 1364-5021. doi: 10.1098/rspa.1984.0023. URL http://rspa.royalsocietypublishing.org/cgi/doi/10.1098/rspa.1984.0023.

[10] V.I. Boev, S.A. Filonovich, M.I. Vasilevskiy, C.J. Silva, M.J.M. Gomes, D.V. Talapin, and A.L. Rogach. Dipole–dipole interaction effect on the optical response of quantum dot ensembles. *Physica B: Condensed Matter*, 338(1-4):347–352, October 2003. ISSN 09214526. doi: 10.1016/j.physb.2003.08.018. URL http://www.sciencedirect.com/science/article/pii/S0921452603005234.

[11] P. Borri, W. Langbein, S. Schneider, U. Woggon, R. Sellin, D. Ouyang, and D. Bimberg. Rabi oscillations in the excitonic ground-state transition of InGaAs quantum dots. *Physical Review B*, 66(8):081306, August 2002. ISSN 0163-1829. doi: 10.1103/PhysRevB.66.081306. URL http://link.aps.org/doi/10.1103/PhysRevB.66.081306.

[12] V. Bouchiat, D. Vion, P. Joyez, D. Esteve, and M. H. Devoret. Quantum Coherence with a Single Cooper Pair. *Physica Scripta*, T76(1):165, 1998. ISSN 0031-8949. doi: 10.1238/Physica.Topical.076a00165. URL http://stacks.iop.org/1402-4896/1998/i=T76/a=024.

[13] E Brion, L H Pedersen, and K Mølmer. Adiabatic elimination in a lambda system. *Journal of Physics A: Mathematical and Theoretical*, 40(5):1033–1043, February 2007. ISSN 1751-8113. doi: 10.1088/1751-8113/40/5/011. URL http://iopscience.iop.org/1751-8121/40/5/011.

[14] B. Broers, H. van Linden van den Heuvell, and L. Noordam. Efficient population transfer in a three-level ladder system by frequency-swept ultrashort laser pulses. *Physical Review Letters*, 69(14):2062–2065, October 1992. ISSN 0031-9007. doi: 10.1103/PhysRevLett.69.2062. URL http://link.aps.org/doi/10.1103/PhysRevLett.69.2062.

[15] C. Simon et al. Quantum memories - A review based on the European integrated project "Qubit Applications (QAP)" | Eur. Phys. J. D. *Eur. Phys. J. D*, 58:1–22, 2010. URL http://epjd.edpsciences.org/index.php?option=com_article&access=standard&Itemid=129&url=/articles/epjd/abs/2010/07/d100125/d100125.html.

[16] H.J. Carmichael. *Statistical Methods in Quantum Optics 1*. 1999.

[17] S. Chelkowski and A. D. Bandrauk. Raman Chirped Adiabatic Passage: a New Method for Selective Excitation of High Vibrational States. *Journal of Raman Spectroscopy*, 28(6):459–466, June 1997. ISSN 0377-0486. doi: 10.1002/(SICI) 1097-4555(199706)28:6<459::AID-JRS124>3.0.CO;2-Y. URL http://doi.wiley.com/10.1002/(SICI)1097-4555(199706)28:6<459::AID-JRS124>3.0.CO;2-Y.

[18] Szczepan Chelkowski and George Gibson. Adiabatic climbing of vibrational ladders using Raman transitions with a chirped pump laser. *Physical Review A*, 52(5): R3417–R3420, November 1995. ISSN 1050-2947. doi: 10.1103/PhysRevA.52.R3417. URL http://link.aps.org/doi/10.1103/PhysRevA.52.R3417.

[19] Pochung Chen, C. Piermarocchi, L. Sham, D. Gammon, and D. Steel. Theory of quantum optical control of a single spin in a quantum dot. *Physical Review B*, 69 (7):075320, February 2004. ISSN 1098-0121. doi: 10.1103/PhysRevB.69.075320. URL http://link.aps.org/doi/10.1103/PhysRevB.69.075320.

[20] T. Cubel, B. Teo, V. Malinovsky, J. Guest, A. Reinhard, B. Knuffman, P. Berman, and G. Raithel. Coherent population transfer of ground-state atoms into Rydberg states. *Physical Review A*, 72(2):023405, August 2005. ISSN 1050-2947. doi: 10.1103/PhysRevA.72.023405. URL http://link.aps.org/doi/10.1103/PhysRevA. 72.023405.

[21] J. Deiglmayr, M. Reetz-Lamour, T. Amthor, S. Westermann, A.L. de Oliveira, and M. Weidemüller. Coherent excitation of Rydberg atoms in an ultracold gas. *Optics Communications*, 264(2):293–298, August 2006. ISSN 00304018. doi: 10.1016/j.optcom.2006.02.058. URL http://www.sciencedirect.com/science/ article/pii/S0030401806004901.

[22] D. Deutsch. Quantum Theory, the Church-Turing Principle and the Universal Quantum Computer. *Proceedings of the Royal Society A: Mathematical, Physical and Engineering Sciences*, 400(1818):97–117, July 1985. ISSN 1364-5021. doi: 10.1098/rspa.1985.0070. URL http://rspa.royalsocietypublishing.org/content/400/ 1818/97.short.

[23] R. H. Dicke. Coherence in Spontaneous Radiation Processes. *Physical Review*, 93 (1):99–110, January 1954. ISSN 0031-899X. doi: 10.1103/PhysRev.93.99. URL http://link.aps.org/doi/10.1103/PhysRev.93.99.

[24] David P. DiVincenzo. The Physical Implementation of Quantum Computation. *Fortschritte der Physik*, 48(9-11):771–783, September 2000. ISSN 00158208. doi: 10.1002/1521-3978(200009)48:9/11<771::AID-PROP771>3.0.CO;2-E. URL http: //arxiv.org/abs/quant-ph/0002077.

[25] D.P. DiVincenzo and D. Loss. Quantum information is physical. *Superlattices and Microstructures*, 23(3-4):419–432, March 1998. ISSN 07496036. doi: 10. 1006/spmi.1997.0520. URL http://www.sciencedirect.com/science/article/pii/ S0749603697905206.

[26] L M Duan, M D Lukin, J I Cirac, and P Zoller. Long-distance quantum communication with atomic ensembles and linear optics. *Nature*, 414(6862): 413–8, November 2001. ISSN 0028-0836. doi: 10.1038/35106500. URL http://dx.doi.org/10.1038/35106500.

[27] M. Dutt, Jun Cheng, Bo Li, Xiaodong Xu, Xiaoqin Li, P. Berman, D. Steel, A. Bracker, D. Gammon, Sophia Economou, Ren-Bao Liu, and L. Sham. Stimulated and Spontaneous Optical Generation of Electron Spin Coherence in Charged GaAs Quantum Dots. *Physical Review Letters*, 94(22), June 2005. ISSN 0031-9007. doi: 10.1103/PhysRevLett.94.227403. URL http://prl.aps.org/abstract/PRL/v94/i22/ e227403.

[28] T. Einwohner, J. Wong, and J. Garrison. Analytical solutions for laser excitation of multilevel systems in the rotating-wave approximation. *Physical Review A*, 14

(4):1452–1456, October 1976. ISSN 0556-2791. doi: 10.1103/PhysRevA.14.1452. URL http://link.aps.org/doi/10.1103/PhysRevA.14.1452.

[29] C. Emary, Xiaodong Xu, D. Steel, S. Saikin, and L. Sham. Fast Initialization of the Spin State of an Electron in a Quantum Dot in the Voigt Configuration. *Physical Review Letters*, 98(4):047401, January 2007. ISSN 0031-9007. doi: 10. 1103/PhysRevLett.98.047401. URL http://link.aps.org/doi/10.1103/PhysRevLett. 98.047401.

[30] Michael Fleischhauer, Atac Imamoglu, and Jonathan Marangos. Electromagnetically induced transparency: Optics in coherent media. *Reviews of Modern Physics*, 77(2):633–673, July 2005. ISSN 0034-6861. doi: 10.1103/RevModPhys.77.633. URL http://link.aps.org/doi/10.1103/RevModPhys.77.633.

[31] Alexey Gorshkov, Axel André, Michael Fleischhauer, Anders Sørensen, and Mikhail Lukin. Universal Approach to Optimal Photon Storage in Atomic Media. *Physical Review Letters*, 98(12):123601–, March 2007. ISSN 0031-9007. doi: 10.1103/ PhysRevLett.98.123601. URL http://link.aps.org/doi/10.1103/PhysRevLett.98. 123601.

[32] Alexey Gorshkov, Axel André, Mikhail Lukin, and Anders Sørensen. Photon storage in Λ-type optically dense atomic media. II. Free-space model. *Physical Review A*, 76(3):033805–, September 2007. ISSN 1050-2947. doi: 10.1103/PhysRevA.76. 033805. URL http://link.aps.org/doi/10.1103/PhysRevA.76.033805.

[33] Alexey Gorshkov, Axel André, Mikhail Lukin, and Anders Sørensen. Photon storage in Λ-type optically dense atomic media. I. Cavity model. *Physical Review A*, 76(3):033804–, September 2007. ISSN 1050-2947. doi: 10.1103/PhysRevA.76. 033804. URL http://link.aps.org/doi/10.1103/PhysRevA.76.033804.

[34] Alexey Gorshkov, Axel André, Mikhail Lukin, and Anders Sørensen. Photon storage in Λ-type optically dense atomic media. III. Effects of inhomogeneous broadening. *Physical Review A*, 76(3):033806–, September 2007. ISSN 1050-2947. doi: 10.1103/PhysRevA.76.033806. URL http://link.aps.org/doi/10.1103/ PhysRevA.76.033806.

[35] a Greilich, D R Yakovlev, a Shabaev, Al L Efros, I a Yugova, R Oulton, V Stavarache, D Reuter, a Wieck, and M Bayer. Mode locking of electron spin coherences in singly charged quantum dots. *Science (New York, N.Y.)*, 313 (5785):341–5, July 2006. ISSN 1095-9203. doi: 10.1126/science.1128215. URL http://www.ncbi.nlm.nih.gov/pubmed/16857937.

[36] A. Greilich, S. Spatzek, I. Yugova, I. Akimov, D. Yakovlev, Al. Efros, D. Reuter, A. Wieck, and M. Bayer. Collective single-mode precession of electron spins in an ensemble of singly charged (In,Ga)As/GaAs quantum dots. *Physical Review B*, 79 (20):201305, May 2009. ISSN 1098-0121. doi: 10.1103/PhysRevB.79.201305. URL http://link.aps.org/doi/10.1103/PhysRevB.79.201305.

[37] Lov K. Grover. A fast quantum mechanical algorithm for database search. page 8, May 1996. URL http://arxiv.org/abs/quant-ph/9605043.

[38] Rui Han, Hui Khoon Ng, and Berthold-Georg Englert. Raman transitions without adiabatic elimination: a simple and accurate treatment. *Journal of Modern Optics*, 60(4):255–265, February 2013. ISSN 0950-0340. doi: 10.1080/09500340. 2013.770573. URL http://www.tandfonline.com/doi/abs/10.1080/09500340.2013. 770573.

[39] Jesús Hernández-Saz, Miriam Herrera, Diego Alonso-Álvarez, and Sergio I Molina. Analysis of the 3D distribution of stacked self-assembled quantum dots by electron tomography. *Nanoscale research letters*, 7(1):681, January 2012. ISSN 1556-276X. doi: 10.1186/1556-276X-7-681. URL http://www.pubmedcentral.nih.gov/articlerender.fcgi?artid=3534247&tool=pmcentrez&rendertype=abstract.

[40] Yasuhiko Ikebe, Nobuyoshi Asai, Yoshinori Miyazaki, and DongSheng Cai. The eigenvalue problem for infinite complex symmetric tridiagonal matrices with application. *Linear Algebra and its Applications*, 241-243:599–618, July 1996. ISSN 00243795. doi: 10.1016/0024-3795(95)00699-0. URL http://www.sciencedirect.com/science/article/pii/0024379595006990.

[41] Tosio Kato. On the Adiabatic Theorem of Quantum Mechanics. *Journal of the Physical Society of Japan*, 5(6):435–439, November 1950. ISSN 0031-9015. doi: 10.1143/JPSJ.5.435. URL http://journals.jps.jp/doi/abs/10.1143/JPSJ.5.435.

[42] E Knill, R Laflamme, and G J Milburn. A scheme for efficient quantum computation with linear optics. *Nature*, 409(6816):46–52, January 2001. ISSN 0028-0836. doi: 10.1038/35051009. URL http://dx.doi.org/10.1038/35051009.

[43] Pieter Kok, Kae Nemoto, T. C. Ralph, Jonathan P. Dowling, and G. J. Milburn. Linear optical quantum computing with photonic qubits. *Reviews of Modern Physics*, 79(1):135–174, January 2007. ISSN 0034-6861. doi: 10.1103/RevModPhys. 79.135. URL http://link.aps.org/doi/10.1103/RevModPhys.79.135.

[44] Miro Kroutvar, Yann Ducommun, Dominik Heiss, Max Bichler, Dieter Schuh, Gerhard Abstreiter, and Jonathan J Finley. Optically programmable electron spin memory using semiconductor quantum dots. *Nature*, 432(7013):81–4, November 2004. ISSN 1476-4687. doi: 10.1038/nature03008. URL http://dx.doi.org/10.1038/nature03008.

[45] L. Landau. No Title. *Phys. Z. Sowjetunion*, (2):46, 1932.

[46] H. Y. Liu, I. R. Sellers, T. J. Badcock, D. J. Mowbray, M. S. Skolnick, K. M. Groom, M. Gutie'rrez, M. Hopkinson, J. S. Ng, J. P. R. David, and R. Beanland. Improved performance of 1.3 μm multilayer InAs quantum-dot lasers using a high-growth-temperature GaAs spacer layer. *Applied Physics Letters*, 85(5):704, July 2004. ISSN 00036951. doi: 10.1063/1.1776631. URL http://scitation.aip.org/content/aip/journal/apl/85/5/10.1063/1.1776631.

[47] M. Lukin. Colloquium: Trapping and manipulating photon states in atomic ensembles. *Reviews of Modern Physics*, 75(2):457–472, April 2003. ISSN 0034-6861. doi: 10.1103/RevModPhys.75.457. URL http://link.aps.org/doi/10.1103/RevModPhys.75.457.

[48] Alexander I. Lvovsky, Barry C. Sanders, and Wolfgang Tittel. Optical quantum memory. *Nature Photonics*, 3(12):706–714, December 2009. ISSN 1749-4885. doi: 10.1038/nphoton.2009.231. URL http://www.nature.com/doifinder/10.1038/nphoton.2009.231.

[49] Maxim N. Makhonin, James E. Dixon, Rikki J. Coles, Ben Royall, Isaac J. Luxmoore, Edmund Clarke, Maxime Hugues, Maurice S. Skolnick, and A. Mark Fox. Waveguide Coupled Resonance Fluorescence from On-Chip Quantum Emitter. *Nano Letters*, 14(12):6997–7002, December 2014. ISSN 1530-6984. doi: 10.1021/nl5032937. URL http://dx.doi.org/10.1021/nl5032937.

[50] S. Malik, E. Le Ru, D. Childs, and R. Murray. Time-resolved studies of annealed InAs/GaAs self-assembled quantum dots. *Physical Review B*, 63(15):155313, March 2001. ISSN 0163-1829. doi: 10.1103/PhysRevB.63.155313. URL http://link.aps.org/doi/10.1103/PhysRevB.63.155313.

[51] V.S. Malinovsky and J.L. Krause. General theory of population transfer by adiabatic rapid passage with intense, chirped laser pulses. *The European Physical Journal D*, 14(2):147–155, May 2001. ISSN 14346060. doi: 10.1007/s100530170212. URL http://www.springerlink.com/index/10.1007/s100530170212.

[52] Pierre Meystre and Murray Sargent. *Elements of Quantum Optics*. 4th edition, 2007.

[53] O. Mishina, N. Larionov, A. Sheremet, I. Sokolov, and D. Kupriyanov. Stimulated Raman process in a scattering medium applied to the quantum memory scheme. *Physical Review A*, 78(4), October 2008. ISSN 1050-2947. doi: 10.1103/PhysRevA.78.042313. URL http://pra.aps.org/abstract/PRA/v78/i4/e042313.

[54] O. Mishina, M. Scherman, P. Lombardi, J. Ortalo, D. Felinto, A. Sheremet, A. Bramati, D. Kupriyanov, J. Laurat, and E. Giacobino. Electromagnetically induced transparency in an inhomogeneously broadened Λ transition with multiple excited levels. *Physical Review A*, 83(5):053809, May 2011. ISSN 1050-2947. doi: 10.1103/PhysRevA.83.053809. URL http://link.aps.org/doi/10.1103/PhysRevA.83.053809.

[55] A. Muller, E. B. Flagg, P. Bianucci, X. Y. Wang, D. G. Deppe, W. Ma, J. Zhang, G. J. Salamo, M. Xiao, and C. K. Shih. Resonance Fluorescence from a Coherently Driven Semiconductor Quantum Dot in a Cavity. *Physical Review Letters*, 99(18):187402, November 2007. ISSN 0031-9007. doi: 10.1103/PhysRevLett.99.187402. URL http://link.aps.org/doi/10.1103/PhysRevLett.99.187402.

[56] T. Nakaoka, T. Saito, J. Tatebayashi, and Y. Arakawa. Size, shape, and strain dependence of the g factor in self-assembled In(Ga)As quantum dots. *Physical Review B*, 70(23):235337, December 2004. ISSN 1098-0121. doi: 10.1103/PhysRevB.70.235337. URL http://link.aps.org/doi/10.1103/PhysRevB.70.235337.

[57] K. Bergmann N.V. Vitanov, B.W. Shore. Adiabatic population transfer in multistate chains via dressed intermediate states | Eur. Phys. J. D, 1998. URL http://epjd.epj.org/articles/epjd/abs/1998/10/d8101/d8101.html.

[58] Nathalie Perret, Denis Morris, Loic Franchomme-Fossé, René Côté, Simon Fafard, Vincent Aimez, and Jacques Beauvais. Origin of the inhomogenous broadening and alloy intermixing in InAs/GaAs self-assembled quantum dots. *Physical Review B*, 62(8):5092–5099, August 2000. ISSN 0163-1829. doi: 10.1103/PhysRevB.62.5092. URL http://link.aps.org/doi/10.1103/PhysRevB.62.5092.

[59] Jarryd J Pla, Kuan Y Tan, Juan P Dehollain, Wee H Lim, John J L Morton, David N Jamieson, Andrew S Dzurak, and Andrea Morello. A single-atom electron spin qubit in silicon. *Nature*, 489(7417):541–5, September 2012. ISSN 1476-4687. doi: 10.1038/nature11449. URL http://dx.doi.org/10.1038/nature11449.

[60] David Press, Thaddeus D Ladd, Bingyang Zhang, and Yoshihisa Yamamoto. Complete quantum control of a single quantum dot spin using ultrafast optical pulses. *Nature*, 456(7219):218–21, November 2008. ISSN 1476-4687. doi: 10.1038/nature07530. URL http://www.ncbi.nlm.nih.gov/pubmed/19005550.

[61] David Press, Kristiaan De Greve, Peter L. McMahon, Thaddeus D. Ladd, Benedikt Friess, Christian Schneider, Martin Kamp, Sven Höfling, Alfred Forchel, and Yoshihisa Yamamoto. Ultrafast optical spin echo in a single quantum dot. *Nature Photonics*, 4(6):367–370, April 2010. ISSN 1749-4885. doi: 10.1038/nphoton.2010. 83. URL http://www.nature.com/nphoton/journal/v4/n6/full/nphoton.2010.83. html#close.

[62] a J Ramsay. A review of the coherent optical control of the exciton and spin states of semiconductor quantum dots. *Semiconductor Science and Technology*, 25(10):103001, October 2010. ISSN 0268-1242. doi: 10.1088/0268-1242/25/10/ 103001. URL http://stacks.iop.org/0268-1242/25/i=10/a=103001?key=crossref. 26468a1ab565451e9940ede1f705fcd6.

[63] K. F. Reim, J. Nunn, V. O. Lorenz, B. J. Sussman, K. C. Lee, N. K. Langford, D. Jaksch, and I. a. Walmsley. Towards high-speed optical quantum memories. *Nature Photonics*, 4(4):218–221, March 2010. ISSN 1749-4885. doi: 10.1038/ nphoton.2010.30. URL http://www.nature.com/doifinder/10.1038/nphoton.2010. 30.

[64] B. J. Riel. An introduction to self-assembled quantum dots. *American Journal of Physics*, 76(8):750, August 2008. ISSN 00029505. doi: 10.1119/1.2907856. URL http://link.aip.org/link/?AJPIAS/76/750/1.

[65] Nicolas Sangouard, Christoph Simon, Jiri Minar, Mikael Afzelius, Thierry Chanelière, Nicolas Gisin, Jean-Louis Le Gouet, Hugues de Riedmatten, and Wolfgang Tittel. Impossibility of faithfully storing single photons with the three-pulse photon echo. *Physical Review A*, 81(6):062333, June 2010. ISSN 1050-2947. doi: 10.1103/PhysRevA.81.062333. URL http://link.aps.org/doi/10.1103/PhysRevA. 81.062333.

[66] Taketomo Sato, Chinami Kaneshiro, Hiroshi Okada, and Hideki Hasegawa. Formation of Size- and Position-Controlled Nanometer Size Pt Dots on GaAs and InP Substrates by Pulsed Electrochemical Deposition. *Japanese Journal of Applied Physics*, 38(Part 1, No. 4B):2448–2452, April 1999. ISSN 0021-4922. doi: 10.1143/JJAP.38.2448. URL http://stacks.iop.org/1347-4065/38/i=4S/a=2448.

[67] Schäfter + Kirchhoff GmbH. Polarization Filters 5PF - Optics, Metrology and Photonics. URL http://www.sukhamburg.com/products/Polarization_Filters_5PF.html.

[68] M. Sénès, B. Urbaszek, X. Marie, T. Amand, J. Tribollet, F. Bernardot, C. Testelin, M. Chamarro, and J.-M. Gérard. Exciton spin manipulation in InAs/GaAs quantum dots: Exchange interaction and magnetic field effects. *Physical Review B*, 71(11):115334, March 2005. ISSN 1098-0121. doi: 10.1103/PhysRevB.71.115334. URL http://link.aps.org/doi/10.1103/PhysRevB.71.115334.

[69] Efrat Shimshoni and Yuval Gefen. Onset of dissipation in Zener dynamics: Relaxation versus dephasing. *Annals of Physics*, 210(1):16–80, August 1991. ISSN 00034916. doi: 10.1016/0003-4916(91)90275-D. URL http://www.sciencedirect.com/science/article/pii/000349169190275D.

[70] Peter Shor. Algorithms for Quantum Computation: Discrete Logarithms and Factoring. In *35th Annual Symposium on Foundations of Computer Science*, volume 51, 1994.

[71] Mika Sillanpää, Teijo Lehtinen, Antti Paila, Yuriy Makhlin, and Pertti Hakonen. Continuous-Time Monitoring of Landau-Zener Interference in a Cooper-Pair Box. *Physical Review Letters*, 96(18):187002, May 2006. ISSN 0031-9007. doi: 10.1103/PhysRevLett.96.187002. URL http://link.aps.org/doi/10.1103/PhysRevLett.96.187002.

[72] J. Smith, P. Dalgarno, R. Warburton, A. Govorov, K. Karrai, B. Gerardot, and P. Petroff. Voltage Control of the Spin Dynamics of an Exciton in a Semiconductor Quantum Dot. *Physical Review Letters*, 94(19):197402, May 2005. ISSN 0031-9007. doi: 10.1103/PhysRevLett.94.197402. URL http://link.aps.org/doi/10.1103/PhysRevLett.94.197402.

[73] A. Steane. The ion trap quantum information processor. *Applied Physics B: Lasers and Optics*, 64(6):623–643, June 1997. ISSN 0946-2171. doi: 10.1007/s003400050225. URL http://link.springer.com/10.1007/s003400050225.

[74] K. Surmacz, J. Nunn, K. Reim, K. C. Lee, V. O. Lorenz, B. Sussman, I. A. Walmsley, and D. Jaksch. Efficient spatially resolved multimode quantum memory. *Physical Review A*, 78(3):033806, September 2008. ISSN 1050-2947. doi: 10.1103/PhysRevA.78.033806. URL http://link.aps.org/doi/10.1103/PhysRevA.78.033806.

[75] D Suter. *The Physics of Laser-Atom Interactions.* 1997.

[76] Fumihiko Tanoue, Hiroharu Sugawara, Kouichi Akahane, and Naokatsu Yamamoto. Highly stacked InGaAs quantum dot laser diodes fabricated by ultrahigh-rate molecular beam epitaxial growth technique. *physica status solidi (c)*, 9(2):226–229, February 2012. ISSN 18626351. doi: 10.1002/pssc.201100287. URL http://doi.wiley.com/10.1002/pssc.201100287.

[77] J. G. Tischler, A. S. Bracker, D. Gammon, and D. Park. Fine structure of trions and excitons in single GaAs quantum dots. *Physical Review B*, 66(8):081310, August 2002. ISSN 0163-1829. doi: 10.1103/PhysRevB.66.081310. URL http://link.aps.org/doi/10.1103/PhysRevB.66.081310.

[78] Michael Varnava, Daniel Browne, and Terry Rudolph. Loss Tolerance in One-Way Quantum Computation via Counterfactual Error Correction. *Physical Review Letters*, 97(12):120501–, September 2006. ISSN 0031-9007. doi: 10.1103/PhysRevLett. 97.120501. URL http://link.aps.org/doi/10.1103/PhysRevLett.97.120501.

[79] Richard J Warburton. Single spins in self-assembled quantum dots. *Nature materials*, 12(6):483–93, June 2013. ISSN 1476-1122. doi: 10.1038/nmat3585. URL http://www.nature.com/nmat/journal/v12/n6/fig_tab/nmat3585_ft.html.

[80] Yanwen Wu, I. Piper, M. Ediger, P. Brereton, E. Schmidgall, P. Eastham, M. Hugues, M. Hopkinson, and R. Phillips. Population Inversion in a Single InGaAs Quantum Dot Using the Method of Adiabatic Rapid Passage. *Physical Review Letters*, 106(6):1–4, February 2011. ISSN 0031-9007. doi: 10.1103/PhysRevLett. 106.067401. URL http://link.aps.org/doi/10.1103/PhysRevLett.106.067401.

[81] Xiaodong Xu, Yanwen Wu, Bo Sun, Qiong Huang, Jun Cheng, D. G. Steel, A. S. Bracker, D. Gammon, C. Emary, and L. J. Sham. Fast Spin State Initialization in a Singly Charged InAs-GaAs Quantum Dot by Optical Cooling. *Physical Review Letters*, 99(9), August 2007. ISSN 0031-9007. doi: 10.1103/PhysRevLett.99.097401. URL http://prl.aps.org/abstract/PRL/v99/i9/e097401.

[82] Xiaodong Xu, Bo Sun, Paul R. Berman, Duncan G. Steel, Allan S. Bracker, Dan Gammon, and L. J. Sham. Coherent population trapping of an electron spin in a single negatively charged quantum dot. *Nature Physics*, 4(9):692–695, August 2008. ISSN 1745-2473. doi: 10.1038/nphys1054. URL http://dx.doi.org/10.1038/nphys1054.

[83] I. Yugova, A. Greilich, E. Zhukov, D. Yakovlev, M. Bayer, D. Reuter, and A. Wieck. Exciton fine structure in InGaAs/GaAs quantum dots revisited by pump-probe Faraday rotation. *Physical Review B*, 75(19):195325, May 2007. ISSN 1098-0121. doi: 10.1103/PhysRevB.75.195325. URL http://link.aps.org/doi/10.1103/PhysRevB.75.195325.

[84] C. Zener. Non-adiabatic crossing of energy levels. *Proc. R. Soc. A*, (137):696, 1932.

Appendix A

Modelling Techniques

A.1   Mathematica NDSolve

The majority of the results presented in this thesis are generated through numerical simulations run in Mathematica. Here I provide an example of the code used and some discussion around how it was used.

```
In[1]:= (*Initialising Required parameters...*)
    Do[sigma[b, a] = Normal[SparseArray[{{4, 4} -> 0, {a, b} -> 1}]], {a, 4},
    {b, 4}];
    rho = 0;

    Do[rho = rho +      p[b, a][t]*sigma[a, b] /. {p[4, 4][t] ->
        1 - p[3, 3][t] - p[2, 2][t] - p[1, 1][t]}, {a, 4}, {b, 4}];
    (*defining the density matrix rho*)

    rotation[w_] =   SparseArray[{Band[{3, 1}] -> Table[Exp[-I*w*t], {i, 2},
    {j, 2}],
        Band[{1, 3}] -> Table[Exp[I*w*t], {i, 2}, {j, 2}]}, {4, 4}, 1] //
        Normal;

    rhor[w_] = rho*rotation[w]; (*used to transform into a frame that
    rotates with the laser frequency, reducing simulation run time*)

    rho0 = {{1, 0, 0, 0}, {0, 0, 0, 0}, {0, 0, 0, 0}, {0, 0, 0, 0}};
    (*define starting state*)
```

We then set up a command "run" which, once called, generates the equations and then implements the Mathematica command NDSolve to run the simulation.

```
In[2]:=  run[w_, w2_, ohmx_, ohmy_, Ee_, Ex_, Eh_, gam_, prec_, T_] := Do[

      H = Ee*sigma[1, 1] + (Ex + Ee)*sigma[3, 3] + (Ee + Ex + Eh)*sigma[4, 4] +
         (1/2)*ohmx*(Exp[-I*w*t]*sigma[1, 3] + Exp[I*w*t]*sigma[3, 1] +
         Exp[-I*w*t]*sigma[2, 4] + Exp[I*w*t]*sigma[4, 2]) +
          (1/2)*ohmy*(Exp[-I*w2*t]*sigma[1, 4] + Exp[I*w2*t]*sigma[4, 1] +
         Exp[-I*w2*t]*sigma[2, 3] + Exp[I*w2*t]*sigma[3, 2]);

      SetAttributes[Equal, Listable]; (*Allows == to act on elements of a matrix*)

      lindblad = (D[rhor[w], t] == -I*(H.rhor[w] - rhor[w].H) +
          gam/2 (2 sigma[3, 1].rhor[w].sigma[1, 3] + 2 sigma[3, 2].rhor[w].sigma[2,
              3] - (sigma[1, 3].sigma[3, 1] +  sigma[2, 3].sigma[3, 2]).rhor[w] -
            rhor[w].(sigma[1, 3].sigma[3, 1] +  sigma[2, 3].sigma[3, 2]) +
            2 sigma[4, 1].rhor[w].sigma[1, 4] + 2 sigma[4, 2].rhor[w].sigma[2,
              4] - (sigma[1, 4].sigma[4, 1] +  sigma[2, 4].sigma[4, 2]).rhor[w] -
            rhor[w].(sigma[1, 4].sigma[4, 1] + sigma[2, 4].sigma[4, 2])));

      temp = Solve[Delete[Flatten[lindblad], 16],
        Delete[Flatten[D[rho, t]], 16]];(*the final component #16 is redundant and
   needs to be removed each time*)

      equations = Flatten[{Delete[Flatten[D[rho, t]] == Flatten[(D[rho, t] /. temp)],
          16], Delete[Flatten[rho == rho0] /. t -> 0, 16]}];

      ClearAttributes[Equal, Listable];

      output =    NDSolve[equations, Delete[Flatten[rho], 16], {t, 0, T},
        MaxSteps -> 1000000, WorkingPrecision -> prec*MachinePrecision];

      , {1}]
```

The precision of the simulation is determined by the "WorkingPrecision" attribute, normally set to "MachinePrecision" which results in an accuracy of roughly 10^{-6}, if resolution below this is required the precision can be increased. The remaining parameters for run[...] define the simulation parameters.

an example RCAP transition:

```
In[3]:=  Ee = 1;
         Eh = 1;
         T = 4000;
         d = 0.1;
         del = 15;
         omega = 1 Exp[-(t - T/2)^2*30/T^2];
```

```
In[4]:=  run[(1200 - Ee - del) - d + t*d/T, (1200 - del), omega, omega, Ee, 1200, Eh,
         0.004, 1, T];
         p[1, 1][t] /. output(*output from NDSolve is in the form of an
         InterpolatingFunction...*)
```

```
Out[4]=  {InterpolatingFunction[{{0.',4000.'}},"<>"][t]}
```

```
In[5]:=  Plot[p[1, 1][t] /. output // Re, t, 0, T](*plot the real part of the output.
         The imaginary part should be 0 by definition, but numerical inaccuracies
          introduce a small imaginary component*)
```

Out[5]=
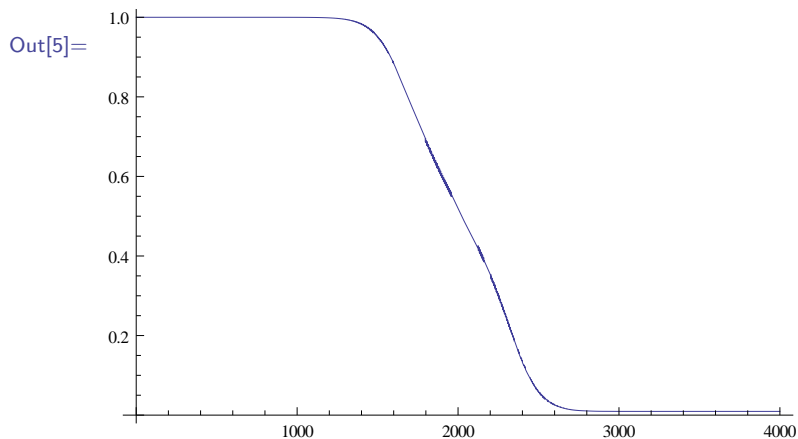
A.2 Bugs/Issues

While running NDSolve Mathematica saves all of the data points for that run. Many of the simulations in this thesis will run out of memory on a standard desktop before the simulation has finished, losing all of the data. For more demanding simulations the NDSolve should be split into N parts and stitched together afterwards.

Running a full density matrix form of the code $\rho'[t] = -i[H, \rho]$ is more demanding than running a wave function form of the code $\psi'[t] = -iH\psi$. However spontaneous emission can only be included for the full density matrix case, much of the research was performed on the vector code then the parameters copied into the density matrix code for the final analysis with the inclusion of spontaneous emission. The code run for initialisation would take days to run fully, the approximations made in section 3.1.1 reduced the equations to a single parameter, and the time to run to seconds. Again the parameters were re-run for the full equations for selected cases to confirm validity, some examples presented in figure 3.4. The results presented would not be possible without these approximations.

Appendix B

Extended Matrix

The extended matrix in section 4 can be generated by the following two commands:

```
In[6]:= n1 = 8;
     Hna = SparseArray[{{i_, i_} → Δ[i - 1], {i_, j_} /; (i - j) ==
           1 → Ω[j]/2, {i_, j_} /; -(i - j) == 1 → Ω[i]/2},
      {n1, n1}] // Normal;

     Hna /. Table[Ω[i] → Ω1, {i, 1, n1 - 1,    2}] /. Table[Ω[i] →
     Ω2, {i, 2,    n1 - 1, 2}] /.  Table[Δ[(n1 - 4)/2 + i] →
     (-1)^i*Δin/2 + i*δin - (-1)^i*δin - δin - δin*Floor[i/2],
     {i, -(n1 - 4)/2, 3 + (n1 - 4)/2}];

     % //MatrixForm
```

Out[6]//MatrixForm=

$$
\begin{pmatrix}
-3\delta\text{in}+\frac{\Delta\text{in}}{2} & \frac{\Omega1}{2} & 0 & 0 & 0 & 0 & 0 & 0 \\
\frac{\Omega1}{2} & -\frac{\Delta\text{in}}{2} & \frac{\Omega2}{2} & 0 & 0 & 0 & 0 & 0 \\
0 & \frac{\Omega2}{2} & -2\delta\text{in}+\frac{\Delta\text{in}}{2} & \frac{\Omega1}{2} & 0 & 0 & 0 & 0 \\
0 & 0 & \frac{\Omega1}{2} & \delta\text{in}-\frac{\Delta\text{in}}{2} & \frac{\Omega2}{2} & 0 & 0 & 0 \\
0 & 0 & 0 & \frac{\Omega2}{2} & -\delta\text{in}+\frac{\Delta\text{in}}{2} & \frac{\Omega1}{2} & 0 & 0 \\
0 & 0 & 0 & 0 & \frac{\Omega1}{2} & 2\delta\text{in}-\frac{\Delta\text{in}}{2} & \frac{\Omega2}{2} & 0 \\
0 & 0 & 0 & 0 & 0 & \frac{\Omega2}{2} & \frac{\Delta\text{in}}{2} & \frac{\Omega1}{2} \\
0 & 0 & 0 & 0 & 0 & 0 & \frac{\Omega1}{2} & 3\delta\text{in}-\frac{\Delta\text{in}}{2}
\end{pmatrix}
$$

Where "n1" defines the size of the matrix created, which should be much larger to avoid end effects.

Calculating the eigenvalues for this matrix should be a simple case of calling the "Eigenvalues" command. However, for larger matrices with analytic components Mathematica struggles to return the values, either providing discontinuous answers which randomly flip between eigenvalues, or worse, simply returning incorrect answers. There are however no issues with Numerical calculations and so the plots of eigenvalues shown in this thesis are calculated through plotting lists of numerical values.

Appendix C

Calculating 6WM example

Here we present an example of calculating the six wave mixing coupling strength. The expanded Hamiltonian for N=6, n=3 and the time independent Schroedinger equation leaves us with the following set of equations:

$$
\begin{aligned}
\mathrm{E}\psi_1 &= \left(4\delta + \tfrac{\Delta}{2}\right)\psi_1 + \tfrac{1}{2}\Omega\psi_2 \\
\mathrm{E}\psi_2 &= \tfrac{1}{2}\Omega\psi_1 + \left(3\delta - \tfrac{\Delta}{2}\right)\psi_2 + \tfrac{1}{2}\Omega\psi_3 \\
\mathrm{E}\psi_3 &= \tfrac{1}{2}\Omega\psi_2 + \left(3\delta + \tfrac{\Delta}{2}\right)\psi_3 + \tfrac{1}{2}\Omega\psi_4 \\
\rightarrow \mathrm{E}\psi_4 &= \tfrac{1}{2}\Omega\psi_3 + \left(2\delta - \tfrac{\Delta}{2}\right)\psi_4 + \tfrac{1}{2}\Omega\psi_5 \\
\mathrm{E}\psi_5 &= \tfrac{1}{2}\Omega\psi_4 + \left(2\delta + \tfrac{\Delta}{2}\right)\psi_5 + \tfrac{1}{2}\Omega\psi_6 \\
\mathrm{E}\psi_6 &= \tfrac{1}{2}\Omega\psi_5 + \left(\delta - \tfrac{\Delta}{2}\right)\psi_6 + \tfrac{1}{2}\Omega\psi_7 \\
\mathrm{E}\psi_7 &= \tfrac{1}{2}\Omega\psi_6 + \left(\delta + \tfrac{\Delta}{2}\right)\psi_7 + \tfrac{1}{2}\Omega\psi_8 \\
\mathrm{E}\psi_8 &= \tfrac{1}{2}\Omega\psi_7 - \tfrac{1}{2}\Delta\psi_8 + \tfrac{1}{2}\Omega\psi_9 \\
\rightarrow \mathrm{E}\psi_9 &= \tfrac{1}{2}\Omega\psi_8 + \tfrac{1}{2}\Delta\psi_9 + \tfrac{1}{2}\Omega\psi_{10} \\
\mathrm{E}\psi_{10} &= \tfrac{1}{2}\Omega\psi_9 + \left(-\delta - \tfrac{\Delta}{2}\right)\psi_{10} + \tfrac{1}{2}\Omega\psi_{11} \\
\mathrm{E}\psi_{11} &= \tfrac{1}{2}\Omega\psi_{10} + \left(-\delta + \tfrac{\Delta}{2}\right)\psi_{11} + \tfrac{1}{2}\Omega\psi_{12} \\
\mathrm{E}\psi_{12} &= \tfrac{1}{2}\Omega\psi_{11} + \left(-2\delta - \tfrac{\Delta}{2}\right)\psi_{12}
\end{aligned}
\tag{C.1}
$$

We are looking to rewrite the two arrowed equations in C.1 in terms of only ψ_4 and ψ_9. We therefore need to solve the remaining equations for ψ_3, ψ_5, ψ_8 and ψ_{10}.

Solving the first three equations for ψ_3 gives:

$$\psi_1 = \frac{\Omega\psi_2}{2\mathrm{E} + \Delta - 2(4\delta + \Delta)}$$

$$\psi_2 = \frac{(2\mathrm{E} - 8\delta - \Delta)\Omega\psi_3}{4\mathrm{E}^2 - 28\mathrm{E}\delta + 48\delta^2 - 2\delta\Delta - \Delta^2 - \Omega^2} \qquad \text{(C.2)}$$

$$\psi_3 = \frac{\Omega\psi_4}{2\left(\mathrm{E} - 3\delta - \frac{\Delta}{2} - \frac{(2\mathrm{E} - 8\delta - \Delta)\Omega^2}{2\left(4\mathrm{E}^2 - 28\mathrm{E}\delta + 48\delta^2 - 2\delta\Delta - \Delta^2 - \Omega^2\right)}\right)}$$

Solving for ψ_{10} using the last three equations:

$$\psi_{12} = \frac{\Omega\psi_{11}}{2\mathrm{E} + 4\delta + \Delta}$$

$$\psi_{11} = -\frac{(2\mathrm{E} + 4\delta + \Delta)\Omega\psi_{10}}{-4\mathrm{E}^2 - 12\mathrm{E}\delta - 8\delta^2 + 2\delta\Delta + \Delta^2 + \Omega^2} \qquad \text{(C.3)}$$

$$\psi_{10} = \frac{\Omega\psi_9}{2\left(\mathrm{E} + \delta + \frac{\Delta}{2} + \frac{(2\mathrm{E} + 4\delta + \Delta)\Omega^2}{2\left(-4\mathrm{E}^2 - 12\mathrm{E}\delta - 8\delta^2 + 2\delta\Delta + \Delta^2 + \Omega^2\right)}\right)}$$

Solving for ψ_8 is done through solving the middle four equations beginning at the top, and solving for ψ_5 is done through solving for the same four equations beginning at the bottom. Solving for ψ_5:

$$\psi_8 = \frac{\Omega\psi_7 + \Omega\psi_9}{2\mathrm{E} + \Delta}$$

$$\psi_7 = \frac{2\mathrm{E}\Omega\psi_6 + \Delta\Omega\psi_6 + \Omega^2\psi_9}{4\mathrm{E}^2 + 4\mathrm{E}\Delta + \Delta^2 - 4\mathrm{E}(\delta + \Delta) - 2\Delta(\delta + \Delta) - \Omega^2}$$

$$\psi_6 =$$

$$\frac{\frac{1}{2}\Omega\psi_5 + \frac{\Omega^3\psi_9}{2\left(4\mathrm{E}^2 + 4\mathrm{E}\Delta + \Delta^2 - 4\mathrm{E}(\delta+\Delta) - 2\Delta(\delta+\Delta) - \Omega^2\right)}}{\mathrm{E} - \delta + \frac{\Delta}{2} - \frac{\mathrm{E}\Omega^2}{4\mathrm{E}^2 + 4\mathrm{E}\Delta + \Delta^2 - 4\mathrm{E}(\delta+\Delta) - 2\Delta(\delta+\Delta) - \Omega^2} - \frac{\Delta\Omega^2}{2\left(4\mathrm{E}^2 + 4\mathrm{E}\Delta + \Delta^2 - 4\mathrm{E}(\delta+\Delta) - 2\Delta(\delta+\Delta) - \Omega^2\right)}}$$

$$\psi_5 =$$

$$\frac{-\Omega\left(-(2\mathrm{E}+\Delta)\left(4(\mathrm{E}-\delta)^2 - \Delta^2\right) + 2(2\mathrm{E}-\delta+\Delta)\Omega^2\right)\psi_4 + \Omega^4\psi_9}{(2\mathrm{E}-4\delta-\Delta)(2\mathrm{E}-2\delta-\Delta)(2\mathrm{E}+\Delta)(2\mathrm{E}-2\delta+\Delta) + \left(-12\mathrm{E}^2 + 24\mathrm{E}\delta - 8\delta^2 + 8\delta\Delta + 3\Delta^2\right)\Omega^2 + \Omega^4}$$

And in reverse to solve for ψ_8:

$$\psi_5 = \frac{\Omega\psi_4 + \Omega\psi_6}{2\mathrm{E} + \Delta - 2(2\delta + \Delta)}$$

$$\psi_6 = \frac{\Omega^2\psi_4 + 2\mathrm{E}\Omega\psi_7 - 4\delta\Omega\psi_7 - \Delta\Omega\psi_7}{4\mathrm{E}^2 - 12\mathrm{E}\delta + 8\delta^2 - 2\delta\Delta - \Delta^2 - \Omega^2}$$

$$\psi_7 =$$

$$\frac{\frac{\Omega^3\psi_4}{2\left(4\mathrm{E}^2 - 12\mathrm{E}\delta + 8\delta^2 - 2\delta\Delta - \Delta^2 - \Omega^2\right)} + \frac{1}{2}\Omega\psi_8}{\mathrm{E} - \delta - \frac{\Delta}{2} - \frac{\mathrm{E}\Omega^2}{4\mathrm{E}^2 - 12\mathrm{E}\delta + 8\delta^2 - 2\delta\Delta - \Delta^2 - \Omega^2} + \frac{2\delta\Omega^2}{4\mathrm{E}^2 - 12\mathrm{E}\delta + 8\delta^2 - 2\delta\Delta - \Delta^2 - \Omega^2} + \frac{\Delta\Omega^2}{2\left(4\mathrm{E}^2 - 12\mathrm{E}\delta + 8\delta^2 - 2\delta\Delta - \Delta^2 - \Omega^2\right)}}$$

$$\psi_8 =$$

$$\frac{\Omega^4\psi_4 + (2\mathrm{E}-4\delta-\Delta)(2\mathrm{E}-2\delta-\Delta)(2\mathrm{E}-2\delta+\Delta)\Omega\psi_9 + 2(-2\mathrm{E}+3\delta+\Delta)\Omega^3\psi_9}{(2\mathrm{E}-4\delta-\Delta)(2\mathrm{E}-2\delta-\Delta)(2\mathrm{E}+\Delta)(2\mathrm{E}-2\delta+\Delta) + \left(-12\mathrm{E}^2 + 24\mathrm{E}\delta - 8\delta^2 + 8\delta\Delta + 3\Delta^2\right)\Omega^2 + \Omega^4}$$

$$(\mathrm{C}.4)$$

Substituting these four solutions into the arrowed equations in equation C.1 is too large to show here, but allows us to calculate Ω_{eff} and Δ_{eff} by separating out the components of ψ_5 and ψ_9.

$$\Omega_{\text{eff}} =$$

$$\frac{\Omega^5}{\left((2\text{E}-4\delta-\Delta)(2\text{E}-2\delta-\Delta)(2\text{E}+\Delta)(2\text{E}-2\delta+\Delta)+\left(-12\text{E}^2+24\text{E}\delta-8\delta^2+8\delta\Delta+3\Delta^2\right)\Omega^2+\Omega^4\right)}$$

$$\Delta_{\text{eff}} =$$

$$\frac{1}{4}\Big(8\delta-4\Delta+$$

$$\frac{-2(2\text{E}-4\delta-\Delta)(2\text{E}-2\delta-\Delta)(2\text{E}-2\delta+\Delta)\Omega^2+4(2\text{E}-3\delta-\Delta)\Omega^4}{(2\text{E}-4\delta-\Delta)(2\text{E}-2\delta-\Delta)(2\text{E}+\Delta)(2\text{E}-2\delta+\Delta)+\left(-12\text{E}^2+24\text{E}\delta-8\delta^2+8\delta\Delta+3\Delta^2\right)\Omega^2+\Omega^4}+$$

$$\frac{\Omega^2}{\text{E}-3\delta-\frac{\Delta}{2}+\frac{(-2\text{E}+8\delta+\Delta)\Omega^2}{2(2\text{E}-8\delta-\Delta)(2\text{E}-6\delta+\Delta)-2\Omega^2}}-\frac{\Omega^2}{\text{E}+\delta+\frac{\Delta}{2}-\frac{(2\text{E}+4\delta+\Delta)\Omega^2}{2(2(\text{E}+\delta)-\Delta)(2\text{E}+4\delta+\Delta)-2\Omega^2}}+$$

$$\frac{\Omega^2}{\text{E}-2\delta-\frac{\Delta}{2}+\frac{\Omega^2\left(-4\text{E}^2+4\text{E}\delta+2\delta\Delta+\Delta^2+\Omega^2\right)}{2(2\text{E}+\Delta)\left(4(\text{E}-\delta)^2-\Delta^2\right)-4(2\text{E}-\delta+\Delta)\Omega^2}}\Big)$$

(C.5)

At this point we replace E with an eigenvalue $\lambda = \pm\sqrt{\Omega_{\text{eff}}^2 + \Delta_{\text{eff}}^2}$. Either eigenvalue can be used as all the components of H_{eff} are symmetric in E. The eigenvalues also contain factors of E, so this approach becomes recursive. Figure C.1 shows the calculation of the resonance condition ($\Delta_{\text{eff}} = 0$) for different numbers of replacements. We find that beyond one replacement the solutions do not vary further when considered at the lowest order approximation. Further replacements make the computations considerably more difficult and introduce extra, non-physical poles, so for all further calculations E is replaced once with the eigenvalue λ and then set to zero.
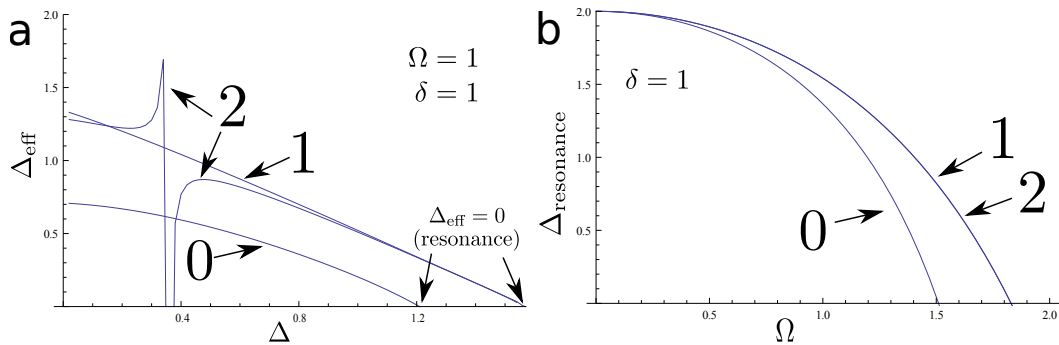

Fig. C.1 a.) Plotting how the calculated Δ_{eff} depends on the number of times E is recursively replaced by λ, an eigenvalue of H_{eff}. b.) Plotting the resonance condition calculation (after lowest order approximations have been made). 0 corresponds to setting E straight to zero, 1 corresponds to replacing E with λ then setting E within λ to zero and 2 corresponds to replacing E with λ twice before setting it to zero

Once Ω_{eff} and Δ_{eff} have been calculated we are left with two large expressions. To simplify Δ_{eff} we then perform a series expansion around $\Omega = 0$ to get

$$\Delta_{\text{eff}} = 2\delta - \Delta - \frac{(3\delta + \Delta)(2\delta + 5\Delta)\Omega^2}{24\delta\Delta(\delta + \Delta)} \tag{C.6}$$

Which for higher orders is a very large expression. This is then expanded around the point $\Delta = 2\delta$, corresponding to resonance at $\Omega = 0$ to get:

$$\Delta_{\text{eff}} = 2\delta - \Delta + \frac{(-86\delta + 13\Delta)\Omega^2}{144\delta^2} \tag{C.7}$$

To calculate Ω_{eff} we use the condition of $\Delta_{\text{eff}} = 0$ to get:

$$\Delta = \frac{2\delta\left(144\delta^2 - 43\Omega^2\right)}{144\delta^2 - 13\Omega^2} \tag{C.8}$$

Which we use to replace Δ within Ω_{eff}, since we only need to consider the strength of NWM when on resonance. This leaves Ω_{eff} as an expression in terms of Ω and δ that we then series expand around $\Omega = 0$ to the lowest order that provides a non-zero answer. For 6WM this is Ω^5, leaving:

$$\Omega_{\text{eff}} = \frac{\Omega^5}{64\delta^4} \tag{C.9}$$